H_0 from Cosmic Background Imager Observations of the Sunyaev-Zel'dovich Effect in Nearby Clusters

Thesis by

Patricia Simcoe Udomprasert

In Partial Fulfillment of the Requirements

for the Degree of

Doctor of Philosophy

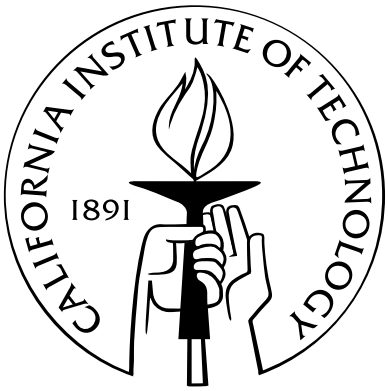

California Institute of Technology

Pasadena, California

2004

(Defended August 12, 2003)

For Rob, with love.

Acknowledgements

Since these are "acknowledgements," I thought I'd begin by acknowledging that yes, living in Chile for 8 months was one of the most difficult things I've ever done. But it was also one of the most rewarding (and no, Tony, I'm not interested in going back). Many of the returns were scientific, but the most important came from the friendships I gained through this project, as the CBI team became a real family to me.

Tony, thank you for giving me the opportunity to work on such an exciting project, and for teaching me so much. Tony made countless sacrifices for the group, spending more time in Chile away from his family than the rest of us, so we wouldn't have to. He held everything together in a way that no one else could, lobbied tirelessly for funding so our work could proceed, and sheltered us grad students from a multitude of behind-the-scenes tasks, so we could focus on our science. And he makes an incredible beef bourgignon.

Tim Pearson and Martin Shepherd, of course, are programming geniuses, but they are also two of the nicest people I've known. I can't thank Tim enough for his invaluable help, scientifically and editorially. Tim's hawk-eyes never allowed me to get away with glossing over things I didn't fully understand, but he always pointed out flaws in my work kindly. His turnaround time in reading thesis chapters was unbelievable. Without Martin, SZBETA would not have happened. He very patiently explained to me the finer details of using pointers and arrays in C, and most importantly, how to use the debugger! I only wish I had taken more of his advice to heart. Martin added countless "special request" gizmos to Difmap and other CBI software, so my thesis work could proceed more quickly, and I could always count on him for late-night company in Robinson. Plus, he put up with all of our abuse. Martin, I hope you know that we only tease you because we care.

In the CBI family, Brian Mason had the role of "cool teenage older brother"—part mentor, part friend, and awesome at both. He taught me most of what I know about the SZE and the 40-meter, and this thesis would never have happened without all his tireless help. His off-the-wall sense of humor and cheerful company also made the long months in Chile pass more quickly. The CBI would not exist without the incomparable Steve Padin, so thank you, not only for your engineering and scientific prowess, but also for teaching me that the English can, in fact, make tasty food. I'll miss the scones, flaming puddings, and plum and treacle sponges.

To my two buddies Jon Sievers and John Cartwright, thank you for sharing the Chile experience (and the office, after we all became so weird upon our return that no one else would). I could always count on you both for help with the science, but also to be the ones who could truly understand what I was going through when times were rough. John, thank you for your wackiness and your friendship, for always knowing what to do in a crisis, and for listening to all my crazy ideas about what to do with life after grad school. Jon, thanks for your patience explaining maximum likelihood and eigenmodes to me (among other things), and for always being willing to be my procrastination buddy. I'll miss slaughtering Bach and cooking with you.

Special thanks go to Steve Myers, for his pioneering work in the field of SZE at low redshift. This project couldn't have happened without his valuable insights and advice. Russ Keeney's work on the 40-meter telescope was vital to the success of the project, and John Yamasaki contributed to the CBI electronics, as well as to my mental health. (And Yama-Q's are the best barbeque ever.) A whole host of people helped take observational data for the various CBI programs, and Sida kept us fed. If only all the health conscious adults in the group hadn't struck the cheese empanadas from the weekly menu.

I'd like to thank my committee, Sterl Phinney, George Djorgovski, Andrew Blain, (and Shri Kulkarni and Wal Sargent from round I) for their suggestions and advice, and especially my committee chair Andrew Lange, for his enthusiastic support of this project. Special thanks to the Readheads and the Sargents for always being interested in how Rob and I were doing, both with the science and otherwise, and for keeping us well-nourished with many an elegant meal. I also wanted

to acknowledge Greg Taylor and all the wonderful folks at NRAO who introduced me to the world of radio interferometry. Many professors at Princeton, especially Neta Bahcall, Michael Strauss, and Jill Knapp, instilled in me a deep love of cosmology. Although I didn't study astronomy with him, an important early mentor who gave me my first job in the physics department, was the late David Wilkinson.

The wondrous team of Cheryl Southard, Patrick Shopbell, and Anu Mahabal are the best system administrators anywhere, and Judith Mack, Loly Ekmekjian, and Sandy Lester were especially helpful in keeping the CBI running smoothly. Thanks for taking such good care of us! Andrew Baker, Brad Behr, Chris Fassnacht, and Roy Gal, among others, helped welcome me to Caltech. Ben Mazin's no-nonsense point of view helped me keep things in perspective over the years. Dave Vakil has become a true friend, someone I can always count on, even though we almost killed each other when we first arrived. Alice Shapley is an irreplaceable person in my life, and I never would have made it through 6 years without her friendship. Her caring, enthusiastic support and encouragement have meant so much to me, and she is one of the most fun people I know. Ashley Borders preserved my sanity with vital ice cream, singing, and chamber music breaks, and she has an uncanny way of knowing when I need to talk. Megan and Bryan Jacoby have both provided support and friendship, and Bryan was a real trouper for putting up with me and Jon in the office. Jackie Kessler's cheerful late-night company helped keep me from really losing it those last few weeks. The St. Andrew's 5 o'clock choir helped to remind me that there was life outside of grad school, and I thank them for their prayers and support.

Although they were far away, Pa, Pam, Chris, Mom, and Nisha have been my most enhusiastic cheering squad. Thank you for always being there for me, even if you only had vague ideas about what I was working on. Rachel and Scooter Fezzie and Ali Reeves are life-long friends who have also provided vast amounts of encouragement long-distance, as have Bob and Ellie Simcoe, and Tim and Steph. Finally, Rob, you've been with me through every step of this process, and I can't thank you enough for all the tremendous love and support you've given me. I couldn't have done this without you.

Abstract

We present H_0 results from Cosmic Background Imager (CBI) observations of the Sunyaev-Zel'dovich Effect (SZE) in 7 galaxy clusters, A85, A399, A401, A478, A754, A1651, and A2597. These observations are part of a program to study a complete, volume-limited sample of low-redshift ($z < 0.1$), X-ray selected clusters. Our focus on nearby objects allows us to study a well-defined, orientation-unbiased sample, minimizing systematic errors due to cluster asphericity. We use density models derived from *ROSAT* imaging data and temperature measurements from *ASCA* and *BeppoSAX* spectral observations. We quantify in detail sources of error in our derivation of H_0, including calibration of the CBI data, density and temperature models from the X-ray data, Cosmic Microwave Background (CMB) primary anisotropy fluctuations, and residuals from radio point source subtraction. From these 7 clusters we obtain a result of $H_0 = 67^{+30}_{-18\,(\mathrm{ran})}{}^{+15}_{-6\,(\mathrm{sys})}$ km s^{-1} Mpc^{-1} for an unweighted sample average. The respective quoted errors are random and systematic uncertainties at 68% confidence. The dominant source of error is confusion from intrinsic anisotropy fluctuations. We present results from simulations of an eigenmode weighting analysis that reduce the uncertainties due to CMB in $h^{-1/2}$ by $\sim$30%.

Contents

List of Figures

List of Tables

Chapter 1

Introduction

The Sunyaev-Zel'dovich Effect (SZE) was first predicted in 1968 (Zel'dovich & Sunyaev, 1969; Sunyaev & Zel'dovich, 1970) as a distortion in the Planck spectrum of the Cosmic Microwave Background (CMB) radiation caused by the Compton scattering of CMB photons by electrons in hot ionized gas. When astronomers discovered extended X-ray radiation coinciding with the Coma, Virgo, Perseus, and other rich clusters (Gursky et al., 1972, and references therein), they postulated that the X-rays could be caused by two possible phenomena, a) bremsstrahlung emission from a non-relativistic thermal population of electrons or b) inverse Compton scattering of the CMB photons by highly relativistic nonthermal electrons. Sunyaev and Zel'dovich (1972) suggested that if it were the former, the optical depth to Compton scattering should still be large enough to boost very slightly the energy of the CMB photons. Since photon number must be conserved, this energy boost would cause a deficit of low-energy photons and an increase in high-energy photons relative to the normal black body spectrum, as seen in Figure 1.1. Under this scenario, if one were to observe the CMB radiation in the direction of a hot cluster, one would expect to see a temperature decline in the map at low frequencies. Sunyaev and Zel'dovich (1972) suggested that if such a phenomenon could be observed towards of rich clusters, it would demonstrate that the emitted X-rays were due to thermal bremsstrahlung radiation.

Pariiskii (1972)[1] reported a detection of a "cold spot" of ~ 1 mK (relative to the CMB) towards the Coma cluster, which at the time lent confidence in the predictions of Sunyaev and Zel'dovich.

[1] Variously transliterated from Russian as Parijskij, Pariysky, Parijsky, Pariishkii, and Pariskii.

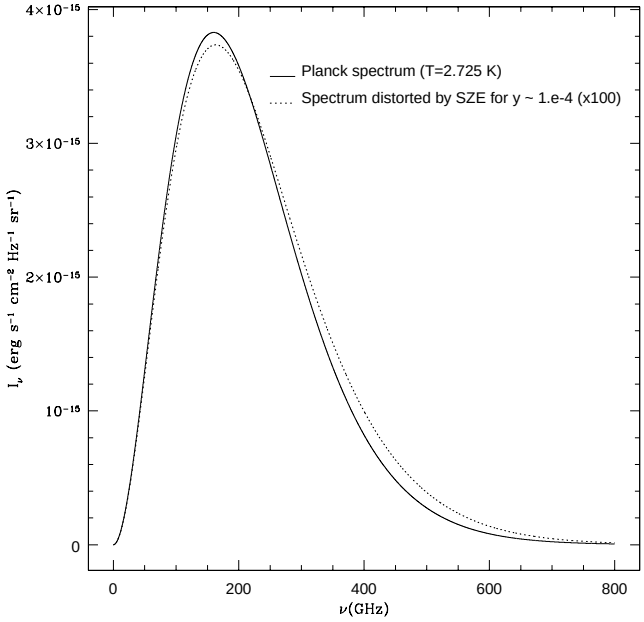

Figure 1.1 The CMB black body spectrum (solid curve) distorted by the thermal non-relativistic SZE (dashed curve) from a cluster with $y = 1 \times 10^{-4}$. The magnitude of the SZE has been increased by a factor of 100.

Although later measurements (e.g., Herbig et al., 1995) have since shown this result to have been in error (likely due to contamination from ground spillover and unsubtracted point sources in the main and reference fields since the observations were at low frequency, 7.5 GHz), it is perhaps fortunate that this was the case, as Pariiskii's early result gave later observers the confidence to attempt and refine their own measurements. Early predictions of the expected SZE magnitude were also somewhat optimistic, and the effort among observers to detect the SZE in other galaxy clusters proceeded more slowly than expected. Over a decade passed before the first reliable detections of the SZE were made in 1984 by Birkinshaw et al. (1984). Since then, however, the SZE has been routinely observed by single dish radio telescopes such as the Owens Valley Radio Observatory (OVRO) 40-meter and 5-meter telescopes (e.g., Mason et al., 2001) and the Nobeyama 45-meter telescope (e.g., Tsuboi et al., 1998), bolometer arrays such as SuZIE (Sunyaev-Zel'dovich Infrared Experiment) and MITO (Millimetre and Infrared Testagrigia Observatory) (Holzapfel et al., 1997; De Petris et al., 2002), and radio interferometers such as the Ryle Telescope and the OVRO and Berkeley Illinois

Maryland Association (BIMA) millimeter arrays (Grainge et al., 2002; Reese et al., 2002). As the technology and observing techniques have improved, the SZE has entered the mainstream as a powerful cosmological tool that enables us to improve our understanding of the universe as well as galaxy clusters themselves.

SZE observations allow one to determine the projected mass of the cluster gas along the line of sight. When combined with independent measurements of Ω_b, the ratio of the baryon mass density to the critical mass density, (for example, from comparisons of observed light element abundances with big bang nucleosynthesis calculations), this yields an upper limit on the density of matter, Ω_M, in the universe, provided the cluster environment is a fair representative of the universe as a whole (e.g., Myers et al., 1997; Grego et al., 2001). By combining SZE, X-ray, and weak lensing observations, the three-dimensional shapes of clusters can be constrained (Zaroubi et al., 1998; Doré et al., 2001). Multifrequency observations of the SZE through the null at 218 GHz yield measurements of the cluster peculiar velocities via the kinematic SZE (Holzapfel et al., 1997). A unique property of the SZE is that it is independent of distance, so its magnitude depends only on the properties of the cluster gas. This allows the possibility of searching for clusters at higher redshift than would be possible from optical and X-ray searches. Such blind cluster searches provide an extremely sensitive probe of Ω_M and Ω_Λ, the energy density associated with the cosmological constant. Most measurements of the SZE so far have focused on joint analyses with X-ray observations in order to determine the Hubble constant, and this is the primary objective of this thesis. Given the different sources of systematic error present in any measurements, it is valuable to approach the distance scale problem from many perspectives.

1.1 The Sunyaev-Zel'dovich Effect

To understand the change in the CMB spectrum due to the SZE, we first consider the scattering of a single photon. The frequency change of the photon depends on the properties of the cluster gas and is proportional to the gas pressure integrated along the line of sight through the cluster. For a rich cluster, the peak central density in the cluster is typically $n_{e0} \sim 10^{-3}$ cm^{-3}, and the

electron temperature $T_e \sim 5-10$ keV (roughly $10^7 - 10^8$ K), so $T_e \gg T_{\rm CMB}$; the following derivation assumes this inequality, and that the cluster gas is isothermal[2]. The SZE is given by the Compton-y parameter

$$y = \frac{k_b T_e}{m_e c^2} \int \sigma_T \, n_e(r) \, dl, \tag{1.1}$$

where k_b is the Boltzmann constant, m_e is the electron mass, c is the speed of light, σ_T is the Thomson electron scattering cross section, $n_e(r)$ is the electron density as a function of cluster radius, and dl indicates an integral along the line of sight. The first part of the expression, $\frac{k_b T_e}{m_e c^2}$, represents the typical fractional energy change imparted to a CMB photon in one scattering, while the second part $\tau = \int \sigma_T \, n_e(r) \, dl$ is the optical depth to scattering. A photon has a probability $\sim \tau e^{-\tau}$ of being scattered once; for a typical rich cluster $\tau \sim 0.01$, so the probability of a scattering is 1%. For $T_e = 5$ keV, $\frac{k_b T_e}{m_e c^2} \sim 10^{-2}$, so $y \sim 10^{-4}$.

Given a distribution of photons with a range of energies, one can calculate the efficiency with which a photon of a particular frequency is scattered. In the non-relativistic limit, this is derived from the Kompaneets equation which describes the interaction between free electrons and photons as a diffusion process. The non-relativistic frequency dependence of the fractional change in intensity due to the thermal SZE is given by

$$f_{\rm nr}(x) = \frac{x e^x}{e^x - 1} \left[x \coth\left(\frac{x}{2}\right) - 4 \right], \tag{1.2}$$

where the normalized frequency is defined as $x = \frac{h\nu}{k_b T_{CMB}}$, with h the Planck constant, ν the frequency of observation, and $T_{CMB} = 2.725$ K, the temperature of the CMB radiation (Fixsen & Mather, 2002).

By combining the above results, the change in radiation intensity due to the SZE in the non-relativistic case is

$$\frac{\Delta I_{\rm SZE}}{I} = y f_{\rm nr}(x) \tag{1.3}$$

[2]In general, as we discuss in Section 4.4.3, one expects T_e to be a function of r. In that case, the pressure integral is $\int T_e(r) n_e(r) \, dl$.

or

$$\frac{\Delta I_{\rm SZE}}{I} = \frac{xe^x}{e^x-1}\left[x\coth\left(\frac{x}{2}\right)-4\right]\frac{k_bT_e}{m_ec^2}\int\sigma_T\,n_e(r)\,dl, \tag{1.4}$$

where I is the CMB intensity,

$$I = \frac{2h\nu^3}{c^2}\frac{1}{e^x-1}. \tag{1.5}$$

Thus,

$$\Delta I_{\rm SZE} = I_0 y\frac{x^4e^x}{(e^x-1)^2}\left[x\coth\left(\frac{x}{2}\right)-4\right], \tag{1.6}$$

where $I_0 = \frac{2h}{c^2}\left(\frac{k_bT_{\rm CMB}}{h}\right)^3$. The change in brightness temperature is given by

$$\frac{\Delta T_{\rm SZE}}{T} = y\left[x\coth\left(\frac{x}{2}\right)-4\right]. \tag{1.7}$$

In the Rayleigh-Jeans limit, for low frequencies, $x \to 0$, and

$$\frac{\Delta T_{\rm SZE}}{T} \sim -2y. \tag{1.8}$$

As discussed above, $y \sim 10^{-4}$ in a typical rich cluster, so the temperature decrement due to the SZE is roughly an order of magnitude larger than the intrinsic anisotropy fluctuations of the CMB on angular scales of a few arcminutes.

The above derivation from the Kompaneets equation is not strictly valid in the case of cluster gas with $T_e \gtrsim 3$ keV since the electron distribution is mildly relativistic. (Typical clusters have mean electron velocities in the range $v \simeq (0.1-0.3)c$.) Also, since the scattering optical depth is so low ($\tau \sim 0.01$) the diffusion process assumed by Kompaneets is not an adequate description of the photon scattering probabilities. Including these effects, the thermal SZE can be represented by

$$\frac{\Delta I_{\rm SZE}}{I} = \tau\frac{xe^x}{e^x-1}\left\{\frac{k_bT_e}{m_ec^2}(F-4)+\left(\frac{k_bT_e}{m_ec^2}\right)^2\left[-10+\frac{47}{2}F-\frac{42}{5}F^2+\frac{7}{10}F^3+\frac{7}{5}G^2(-3+F)\right]\right\}, \tag{1.9}$$

(Sazonov & Sunyaev, 1998; Challinor & Lasenby, 1998; Itoh et al., 1998), where $F = x\coth(x/2)$ and

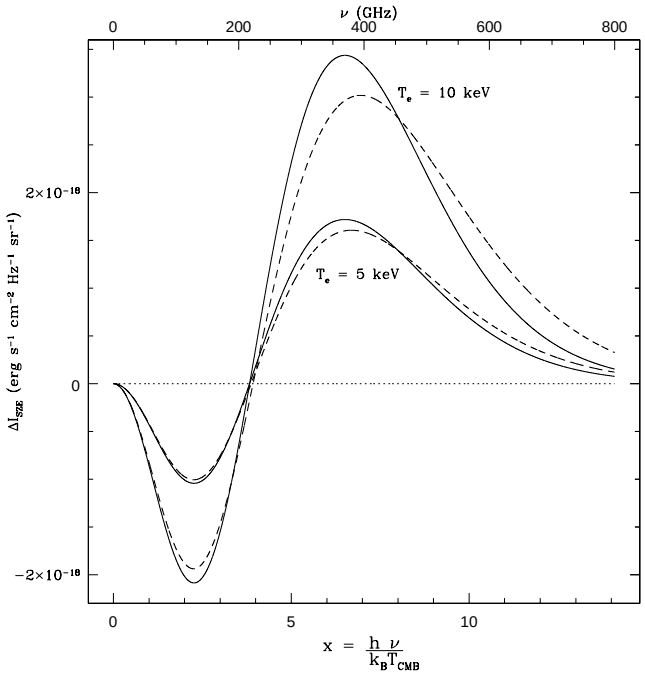

Figure 1.2 The thermal SZE as a function of radiation frequency for $T_e = 5$ keV and $T_e = 10$ keV with (dashed curve) and without (solid curve) the relativistic corrections.

$G = x/\sinh(x/2)$. In this case, the frequency dependence of the SZE is dependent upon the electron gas temperature. The first term in Equation 1.9 ($\propto \frac{k_b T_e}{m_e c^2}$) represents the original non-relativistic thermal SZE. The second term in Equation 1.9 ($\propto \left(\frac{k_b T_e}{m_e c^2}\right)^2$) is the relativistic correction (Sazonov & Sunyaev, 1998; Challinor & Lasenby, 1998). This analytical expression for the correction has been shown to be in good agreement with numerical results of Rephaeli (1995) for clusters with temperatures up to 15 keV, a limit which includes all the objects we will consider. Figure 1.2 shows the thermal SZE as a function of radiation frequency for $T_e = 5$ keV and $T_e = 10$ keV with and without the relativistic corrections. For both temperatures, the low energy photons are scattered more efficiently and boosted to higher energies when compared with the non-relativistic case. In the non-relativistic approximation the crossover frequency, also called the SZE null, is at 218 GHz. The frequency of the SZE null shifts when relativistic effects are correctly accounted for. The relativistic correction is substantial at frequencies $x > 2 - 3$, but at frequencies which we will be considering ($\nu \sim 30$ GHz, or $x \sim 0.5$), the relativistic term amounts to $\sim$3% reduction in the magnitude of the SZE.

1.2 Bremsstrahlung Emission

The extended X-ray emission discovered in rich clusters in the 1970's was indeed found to be primarily thermal bremsstrahlung from the ionized gas we have been discussing (although some clusters do show evidence of also having some X-ray emission due to inverse Compton scattering of CMB photons). The X-ray surface brightness from thermal bremsstrahlung is given by

$$b_X(E) = \frac{1}{4\pi(1+z)^3} \int n_e^2(r) \Lambda(E, T_e)\, dl \tag{1.10}$$

(e.g., Birkinshaw, 1999), where $\Lambda(E, T_e)$ is the X-ray spectral emissivity, a function of the energy of observation, E, the electron temperature, the metallicity of the gas, and the redshift, z. For a sufficiently broad X-ray bandpass, $\Lambda \propto T_e^{1/2}$, roughly.

1.3 Measuring H_0 from X-ray and SZE Observations of Galaxy Clusters

The SZE is proportional to $\int n_e T_e\, dr$, while the X-ray emission due to thermal bremsstrahlung is proportional to $\int n_e^2 \Lambda(E, T_e)\, dr$. X-ray imaging observations constrain the cluster density profiles, while X-ray spectroscopy provides temperature measurements. These allow one to predict the expected SZE towards a cluster. The comparison of the X-ray and SZE observations, coupled with the assumption that clusters are spherically symmetric, yields a direct measurement of H_0, independent of the cosmic distance ladder.

The cluster gas is typically assumed to be well fitted by a spherical isothermal β-model (Cavaliere & Fusco-Femiano, 1978), with the gas distribution following the form

$$n_e(r) = n_{e0} \left(1 + \frac{r^2}{r_0^2}\right)^{-3\beta/2}, \tag{1.11}$$

where n_{e0} is the central electron density, r_0 is the physical core radius (related to the angular core

radius, θ_0, by $r_0 = D_A\theta_0$, where D_A is the angular diameter distance to the cluster), and β is the power law index. The electron temperature T_e is taken to be a constant. By substituting Equation 1.11 into Equation 1.9, for a given frequency and temperature, the SZE becomes

$$\Delta I_{\rm pred} \propto n_{e0}\theta_0 D_A \left(1 + \frac{\theta^2}{\theta_0^2}\right)^{-\frac{3}{2}\beta+\frac{1}{2}}. \tag{1.12}$$

This is the model prediction. As we will show in Chapter 4, our measurement of $n_{e0} \propto h^{1/2}$ and $D_A \propto h^{-1}$, so $\Delta I_{\rm pred} \propto h^{-1/2}$. By comparing the predicted model with the observed SZE, one obtains H_0:

$$\frac{\Delta I_{\rm pred}}{\Delta I_{\rm obs}} = h^{-1/2}. \tag{1.13}$$

1.4 Systematic Errors

Several assumptions enter the SZE/X-ray determination of H_0, the most important being that the cluster gas is spherical, smooth, and isothermal. Any deviations from these assumptions may bias the H_0 result. Several studies (e.g., Carter & Metcalfe, 1980; McMillan et al., 1989; Mohr et al., 1995) show that many clusters are aspherical, so H_0 results from any one cluster are likely to be biased. If one can construct a complete sample of randomly oriented clusters, one would expect a bias of $< 3\%$ in H_0 for a sample of 25 clusters (Cooray, 2000), based on X-ray observations of two-dimensional cluster shapes (Mohr et al., 1995). Until recently, most SZE studies have focused on clusters at relatively high redshift ($0.15 < z < 0.9$), where issues of completeness cannot be addressed with confidence. Optical and X-ray selection of galaxy clusters at high redshift favor the detection of clusters elongated along the line of sight, since a cigar shaped cluster pointed toward the observer would show a larger galaxy overdensity in optical observations (or have a greater X-ray intensity) than a similar object oriented perpendicular to the line of sight. Thus, a determination of H_0 from high-redshift clusters (as has been done by Birkinshaw et al. (1984); Grainge et al. (2002); Reese et al. (2002)) may be biased low relative to the actual value due to the predominance of clusters elongated along the line of sight in the sample. Myers et al. (1997) and Mason et al. (2001)

have used a single dish telescope, the OVRO 5-meter telescope, to observe nearby ($z < 0.1$) clusters. At low redshift, it is straightforward to define a volume limited, complete sample, with clusters randomly oriented. Thus, in order to obtain an H_0 measurement from the SZE which is free from orientation bias, it is advantageous to construct a sample of clusters at low redshift, which is what we do in this thesis.

X-ray data also demonstrate that temperature profiles may not be isothermal (Markevitch et al., 1998; De Grandi & Molendi, 2002), nor is the gas smooth, particularly in the case of clusters that have recently merged. Again, one can best deal with these difficulties by observing nearby clusters because their larger angular sizes relative to distant clusters allow any deviations from the model assumptions to be observed with greater resolution. Also, nearby clusters have been studied in more detail at all wavelengths, and X-ray observations require less integration time to obtain comparable sensitivity to those at high redshift since the X-ray flux decreases as D_L^{-2} (where the luminosity distance $D_L = D_A(1+z)^2$).

1.5 Observations of the SZE with an Interferometer

Herbig et al. (1995) made the first reliable observations of a nearby cluster, Coma, with the OVRO 5-meter telescope. Since then, Myers et al. (1997) and Mason et al. (2001) have expanded upon their work and have used the OVRO 5-meter telescope to observe a well-defined sample. We further extend this work by observing a larger sample with an interferometer, the Cosmic Background Imager (CBI), a 13-element interferometer located in the Chilean Andes. There are several advantages of observing the SZE with an interferometer over a single dish telescope, and we describe them in this section.

1.5.1 Overview of Radio Interferometry

An interferometer produces a Fourier transform of the sky through measurements of complex visibilities. A simplified schematic of a two-element interferometer (e.g., Thompson et al., 1998) is presented in Figure 1.3. The incoming wavefront arrives at one of the antennas with a geometrical

delay of

$$\tau_g = \frac{\boldsymbol{b} \cdot \boldsymbol{s}}{c} = \frac{|\boldsymbol{b}|}{c} \sin(\Psi_0 + \theta), \tag{1.14}$$

where $\boldsymbol{b}$ is the baseline vector, $\boldsymbol{s}$ is the unit vector describing the direction of the source, and c is the speed of light. The angle Ψ_0 represents the telescope pointing center, and θ gives the source position with respect to the pointing center. The input waveforms seen by the antennas as a function of time are

$$V_1 = v_1 \cos 2\pi\nu(t - \tau_g), \tag{1.15}$$

and

$$V_2 = v_2 \cos 2\pi\nu t, \tag{1.16}$$

where v_1 and v_2 are the amplitudes of the incoming waves, and ν is the frequency of observation. A correlator voltage multiplies and time averages the signal, giving an output

$$r(\tau_g) = v_1 v_2 \cos 2\pi\nu\tau_g. \tag{1.17}$$

The cosine term represents the oscillation of the source through the interferometer fringe pattern, caused by τ_g slowly changing with time as the earth rotates, and $v_1 v_2$ is the amplitude.

The vector $\boldsymbol{b}$ is represented by (u, v), where u and v are usually given in units of wavelengths. The position of the source on the sky is (x, y). With these definitions, the complex visibility of a source is given by

$$V(u, v) = \int A(x, y) I(x, y) e^{-2\pi(ux+vy)i} dx\, dy, \tag{1.18}$$

where $A(x, y)$ is the primary beam response of the interferometer antennas, and $I(x, y)$ is the source intensity distribution. Longer baselines have shorter periods of fringe oscillations, and hence are sensitive to emission on smaller angular scales. The angular resolution of an interferometer is approximately λ/b, where λ is the wavelength of the observation and b is the baseline length.

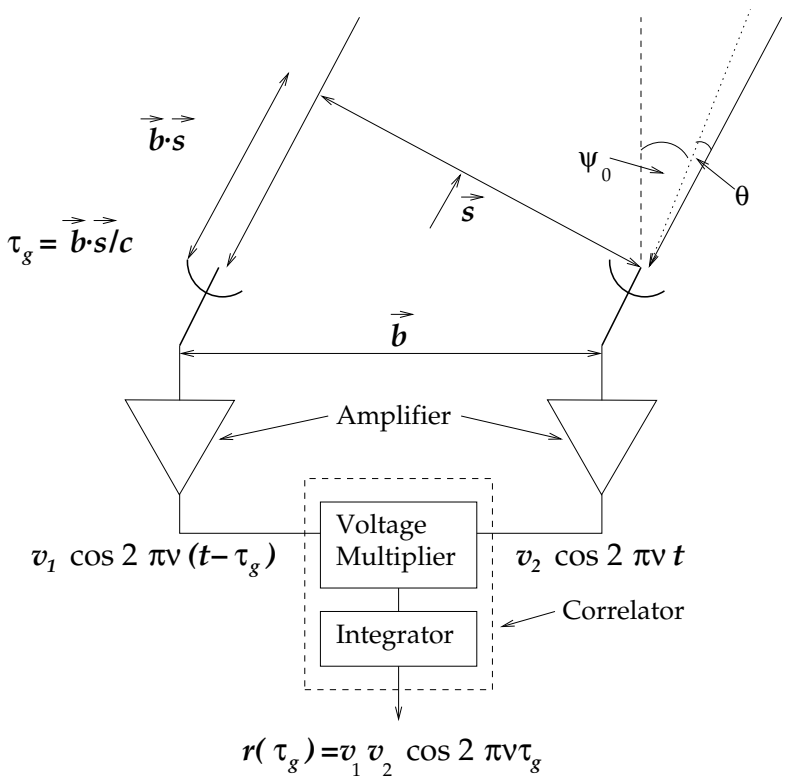

Figure 1.3 Schematic of two-element interferometer (after, e.g., Thompson et al. (1998))
.

1.5.2 Advantages of Observing the SZE with an Interferometer

An interferometer baseline measures fluctuations on a particular size scale, and anything larger than this is "resolved out," so any constant background signal is automatically rejected by the telescope, making control of systematic effects more straightforward. Interferometers also produce maps, rather than a single temperature measurement, allowing for more direct comparisons with X-ray observations. However, most interferometers are too large to observe nearby clusters. Since the CBI was built to observe fluctuations of the CMB primary anisotropies on arcminute scales, it is a much smaller instrument than most interferometer arrays, and its angular resolution is very well matched to the size scales of nearby clusters. (At $z = 0.1$, an object with a physical size of 1 Mpc would have an angular size of $13h$ arcmin, which is comparable to the angular resolution of the CBI). Figure 1.4 shows A478, a cluster at $z = 0.088$ represented as an isothermal β-model. The top plot shows the SZE image profile, and the bottom plot is the visibility profile for the CBI (including the primary beam) as a function of projected baseline length in wavelengths. The visibility profile drops off rapidly as baseline length increases. Thus a large interferometer such as the Very Large Array (VLA), or even the BIMA or OVRO mm arrays would not be able to observe this cluster, since the minimum baseline length for those arrays is 7 meters, giving a baseline length of about 700λ where the visibility is very low.

1.6 Thesis Overview

This thesis reports results from a program to determine H_0 through observations of the SZE in a complete sample of low-redshift ($z < 0.1$) galaxy clusters using the CBI. The CBI is ideal for observing low-z clusters with high resolution and sensitivity, and we take advantage of these capabilities to minimize potential systematic errors discussed. In Chapter 2, we describe the CBI in more detail and discuss our sample selection and observing strategy. We explain how the CBI SZE observations were taken and calibrated, and we discuss the point source removal through observations with the OVRO 40-meter telescope. In Chapter 3 we present the CBI cluster images and briefly describe

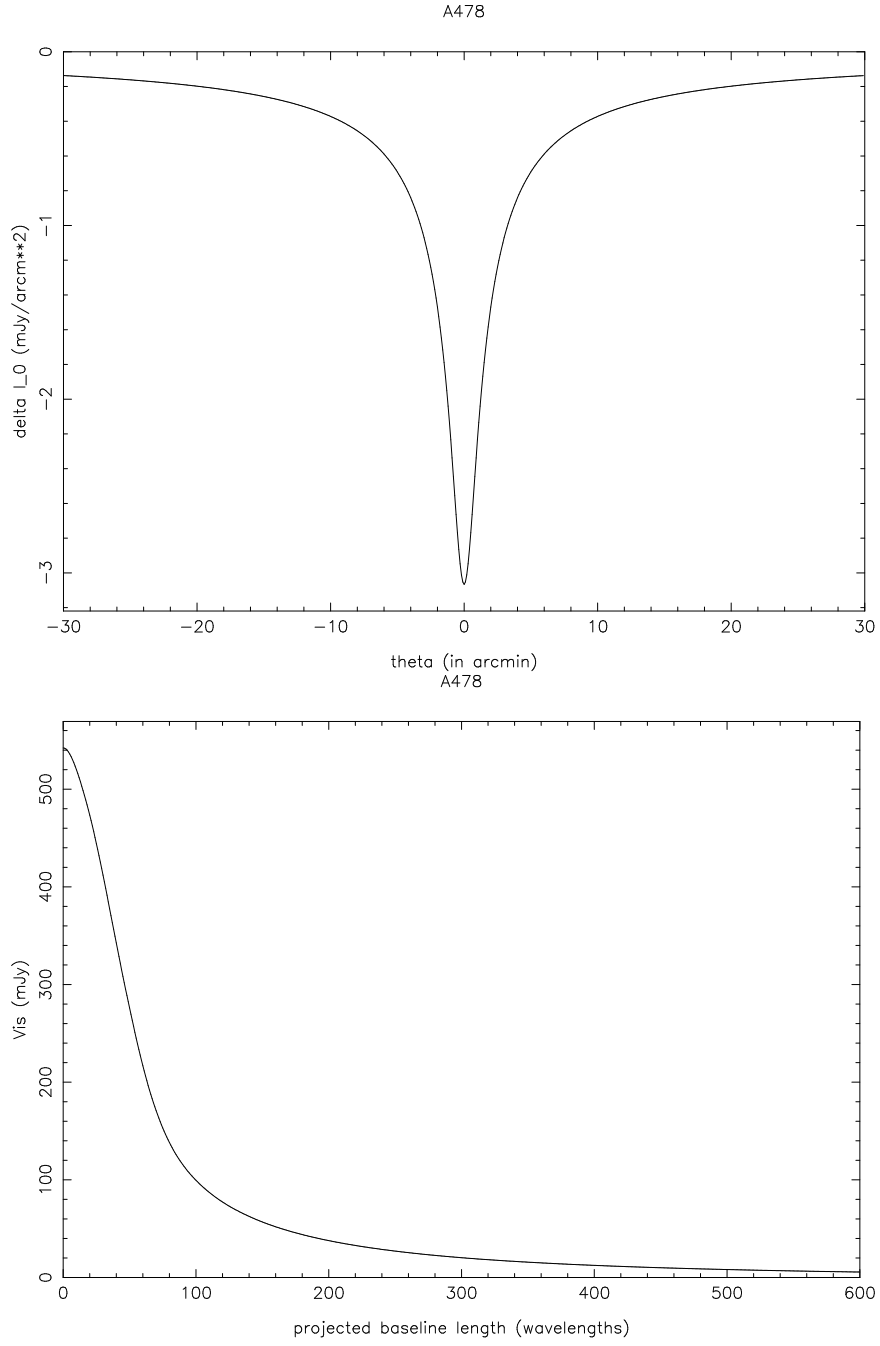

Figure 1.4 SZE image and visibility profiles for A478 ($z = 0.088$) assuming an isothermal β-model with $\beta = 0.64$, θ_0=1′, $n_{e0} = 27.0 \times 10^{-3} h^{1/2}$ cm^{-3}, and $T_e = 7.9$ keV.

each object, focusing on any features that might make a cluster especially suitable (or not so) for studying cosmology with the SZE. In the first part of Chapter 4 we detail the analysis method used to determine the Hubble constant from the clusters in our sample using CBI SZE observations and published X-ray data. In the second part of the chapter, we study various sources of uncertainty in our measurement including observational errors from calibration accuracy, thermal noise, primary anisotropy fluctuations in the CMB, and residuals from point source subtraction mainly through Monte Carlo simulations. We also quantify errors from model-dependent sources such as cluster density profiles and electron temperature. Finally we discuss possible errors from the assumptions that the cluster gas has a smooth and isothermal distribution. Chapter 5 describes an improved analysis method that takes into account the known CMB power spectrum to minimize its effect on the SZE H_0 results. Finally, we discuss our conclusions in Chapter 6. Throughout the thesis, we use $H_0 = 100\ h$ km s^{-1} Mpc^{-1}, and we assume a flat Λ-CDM universe with Ω_m=0.3, Ω_Λ=0.7.

Chapter 2

Observations

This chapter is divided into two main sections. First we build upon the discussion from Chapter 1 and describe the selection of the CBI cluster sample. We have already emphasized the importance of observing a complete, orientation-unbiased sample; here, we describe how we assemble such a sample from a variety of X-ray selected cluster surveys. Details of the SZE observations are presented in the second part of this chapter, which is further divided into subsections beginning with a discussion of the CBI telescope and the specific features that make this experiment possible. Next, we describe the SZE observing strategy, data acquisition and calibration, and finally, we discuss the point source removal using the Owens Valley Radio Observatory (OVRO) 40-meter telescope.

2.1 Cluster Sample Selection

Myers et al. (1997) were the first group to stress that only by studying a complete, orientation-unbiased sample can one derive cosmological parameters that are free of bias when using the SZE. Cooray (2000) showed based on the distribution of observed two-dimensional cluster shapes (Mohr et al., 1995), that 25 randomly oriented clusters drawn from an intrinsically prolate (cigar shaped) distribution would yield a sample error in H_0 of $< 3\%$ due to asphericity. If the clusters have an intrinsically oblate (pancake shaped) distribution, the uncertainty in the sample increases to 8%. However, this scenario is less likely in the modern view of structure formation, where clusters formed along cosmological filaments would tend to become prolate.

Early on, deciding what makes up a galaxy cluster was a subjective process. Abell (1958) defined

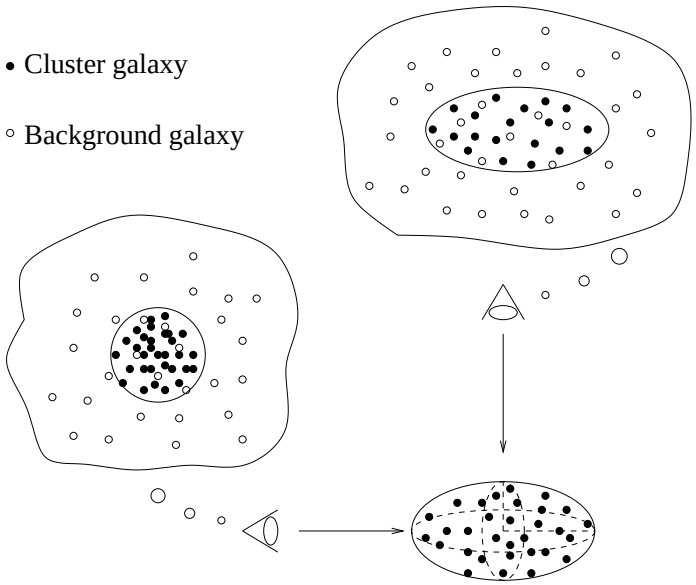

Figure 2.1 A schematic showing how a cluster viewed from a sight line parallel to the long axis of the cluster is easier to detect than the same cluster viewed from a sight line perpendicular to this axis.

his catalog by searching for galaxy overdensities in the Palomar Sky Survey plates by eye. Since then, methods for automating optically based cluster searches have improved significantly, but the catalogs almost always suffer from a bias because it is easier to detect a non-spherical cluster oriented along the line of sight than one that is perpendicular to the line of sight. As Figure 2.1 shows, projection effects produce a larger galaxy overdensity when the observation sightline is parallel to the long axis of the cluster. Otherwise, it is possible for the cluster to blend in with the background galaxies and go undetected.

The discovery that diffuse intracluster gas is a strong X-ray emitter gave astronomers an important new tool to use in the process of identifying galaxy clusters. The extended X-ray emission is less subject to projection effects, and it provides a concrete way to define a gravitationally bound cluster. The original Myers et al. (1997) study is based on a survey compiled from older X-ray satellite missions including *Einstein Observatory*, *HEAO-1*, and *EXOSAT* (Edge et al., 1990). Since then, the improved sensitivity and resolution of the *ROSAT* All Sky Survey (RASS) has allowed significant advances in the field of X-ray cluster searches. Several X-ray cluster catalogs have been constructed based on the RASS. The following section describes four of these cluster surveys and

how we use them to assemble the CBI SZE cluster sample.

2.1.1 RASS Surveys

Most of the available studies employ some combination of X-ray and optical selection, with an emphasis on the X-ray. In this section, we describe in chronological order each of the surveys that we used in assembling the CBI cluster sample. The surveys apply different analysis methods, allowing comparisons to be made in their regions of overlap. Table 2.1 summarizes the key features of the different RASS cluster surveys.

- **X-ray-brightest Abell-type Clusters of Galaxies: XBACs** (Ebeling et al., 1996)

  This is an older catalog of 242 Abell clusters covering both the northern and southern hemispheres, with $|b| \geq 20^{\circ}$. It is complete at the 80% level to a flux limit of 5.0 $\times 10^{-12}$ erg s^{-1} cm^{-2} in the 0.1-2.4 keV band. The sample was constructed by cross-correlating cluster positions from Abell (1958) and Abell et al. (1989, hereafter, ACO) with RASS sources that had count rates in excess of 0.1 s^{-1}. Since the XBACs catalog is made up entirely of Abell and ACO clusters, this survey is especially reliant on the completeness of the parent optical samples. There are 121 ACO clusters with $z \leq 0.05$, and only 60 of these are in the XBACs list. The algorithm used to process the RASS for this particular survey was designed to detect point sources and hence had trouble with the more extended very nearby sources. The other 61 clusters had to be explicitly added to the sample. Since the CBI sample is also at low-redshift ($z < 0.1$), this is a potential worry. Mason & Myers (2000) used the XBACs sample (Ebeling et al., 1996) to define a 90% complete, volume-limited sample of 31 clusters with $z < 0.1$ for the OVRO-5 meter telescope SZE study.

- **The *ROSAT* Brightest Cluster Sample: BCS** (Ebeling et al., 1998)

  This catalog of 201 clusters also covers $|b| \geq 20^{\circ}$, but with $\delta \geq 0^{\circ}$, $z < 0.3$, and is complete at the 90% level to a flux limit of 4.4 $\times 10^{-12}$ erg s^{-1} cm^{-2} in the 0.1-2.4 keV band. Of these, 71% are Abell clusters, 10% are Zwicky clusters, 19% are not in either catalog. The authors

searched explicitly for X-ray emission around Abell and Zwicky clusters, but also examined bright X-ray sources in the RASS which their algorithm found to be significantly extended. They then performed follow-up optical observations to confirm identifications as clusters and to obtain redshifts.

- **The Northern *ROSAT* All-Sky Galaxy Cluster Survey: NORAS** (Böhringer et al., 2000)

  This is a purely X-ray selected survey, covering $\delta \geq 0^\circ$ and $|b| \geq 20^\circ$. The authors studied a sample of 495 sources which were shown in the RASS to be extended and had a count rate $\geq$ 0.06 counts s^{-1}. An optical follow-up identification program found 378 (76%) of these sources to be clusters, discovering 98 previously unknown clusters. The region between 9^h and 14^h in right ascension was studied in further detail to determine the overall completeness of the sample. In this range, they searched for X-ray emission of known clusters and looked again for extended X-ray sources from a second processing of the RASS database, which was better suited to detecting extended sources. They found emission from 85 additional Abell clusters and 56 cluster candidates among the extended sources that had been missed in the previous analysis. The authors estimate that the NORAS sample is complete at the 50% level at a flux of 3×10^{-12} erg s^{-1} cm^{-2} in the 0.1-2.4 keV band, and in the region with the additional study, by adding the new clusters, they achieve 82% completeness relative to the REFLEX survey, described next[1].

- **The *ROSAT* -ESO Flux Limited X-ray Cluster Survey: REFLEX**[2] (Böhringer et al., 2001; Boehringer et al., 2003)

  The REFLEX group identified clusters by looking for galaxy overdensities around each source in the RASS above a particular count rate. The optical survey they used for this is the COSMOS (MacGillivray & Stobie, 1984) digitization of the SERC Southern Sky Survey plates. Follow-up optical observations were taken to confirm identifications of clusters and to determine

[1]The NORAS team has planned follow-up work similar to that done for REFLEX to improve the completeness of the survey.

[2]We thank the REFLEX team for providing us with a portion of their catalog in advance of publication.

Table 2.1 RASS X-ray cluster survey parameters, compared to those chosen for the CBI cluster sample. All surveys exclude $|b| < 20^\circ$ and use the 0.1–2.4 keV bandpass.

Survey	N clusters	δ range	flux limit 10^{-12}erg s^{-1} cm^{-2}	Est. Completeness	Notes
XBACs	242	All-sky	5.0	80%	ACO parent
BCS	201	$\delta \geq 0^\circ$	4.4	90%	ACO, Zwicky, and X-ray
NORAS	378	$\delta \geq 0^\circ$	3.0	50%	purely X-ray selected
REFLEX	452	$\delta < 2.5^\circ$	3.0	>90%	X-ray + Optical
CBI	25	$-70^\circ < \delta < 24^\circ$	10.0	$\gtrsim$95%	

redshifts. Their catalog contains 452 clusters with a flux limit of 3×10^{-12} erg s^{-1} cm^{-2} in the 0.1–2.4 keV band. The survey encompasses the region with $\delta < 2.5^\circ$ and galactic latitude $|b| \geq 20^\circ$, covering an area of 4.34 ster. The completeness exceeds 90%, and extends out to a redshift of $z < 0.5$ (Böhringer et al., 2001).

2.1.2 CBI Sample

We now discuss how we built the CBI cluster sample from the RASS surveys described. We wanted to focus our study on nearby clusters, so we chose a redshift limit $z \leq 0.1$. To maximize completeness of our sample, we chose a high flux limit of 1.0 $\times10^{-11}$ erg s^{-1} cm^{-2} in the 0.1-2.4 keV band. This is significantly higher than the flux limits of all the surveys. We then selected a volume-complete sample using the redshift and flux cutoffs. We derived the sample luminosity limit by calculating the luminosity distance at $z = 0.1$ in an $\Omega_0 = 1, \Omega_\Lambda = 0$ universe with H_0=50 km s^{-1} Mpc^{-1}, which is the cosmology assumed in all the cluster catalog papers. For these parameters, the luminosity distance is given by

$$D_L = \frac{2c(1+z)}{H_0}\left(1 - \frac{1}{\sqrt{1+z}}\right), \tag{2.1}$$

so $D_L = 614.3$ Mpc at $z = 0.1$. Using

$$L_x = 4\pi D_L^2 f_x, \tag{2.2}$$

where f_x is equal to the flux limit of the sample, we obtain a luminosity cutoff of 4.52 $\times10^{44}h_{50}^{-2}$ erg s^{-1} in the 0.1 to 2.4 keV band. This luminosity cutoff corresponds to clusters that have high mass

($M > x$) and are optically rich[3].

Due to the CBI elevation limit of $> 43°$ and latitude of $-23°$, we were restricted to observing sources with declinations $-70° < \delta < 24°$. Table 2.2 lists 26 clusters that meet our selection criteria and indicates the RASS catalog in which they were found. The positions of the clusters fields were taken primarily from Ebeling et al. (1996), since these are what were available for most of the CBI clusters when we began our observations. These positions are obtained from *ROSAT* All-Sky Survey data, and they often differ from centroid derived from pointed PSPC and HRI observations by $\sim 1'$, a substantial fraction of the CBI $5'$ synthesized beam. Where available, we use the centroid positions from the pointed observations in our analysis. All the surveys exclude galactic latitudes $|b| < 20°$ in order to minimize contamination from dense stellar fields in the Milky Way. BCS and NORAS both cover the northern half of the sky with $\delta \geq 0°$, while REFLEX covers the southern portion with $\delta < 2.5°$, and XBACs covers both hemispheres.

We use Table 2.2 to assess the completeness of our sample. XBACs missed three clusters found in other catalogs, giving an incompleteness of 12%, which is better than the quoted 80% level of the catalog. This is expected given the higher flux limit we have chosen for our sample. One Zwicky cluster, Z5029, and one new cluster found by REFLEX are among those missed, showing the limitation in XBACs of only correlating X-ray sources with a limited number of optical catalogs of known clusters. BCS finds all five of the northern clusters listed, while NORAS finds only three. NORAS is known to have had difficulty with extremely nearby clusters because the earliest processing of the RASS data was not optimized to detect extended sources. Missing two of five clusters is consistent with the catalog completeness of 50%. BCS correlated the RASS data with several optical catalogs in addition to doing blind searches of extended X-ray emission, and should be the most complete survey in the northern hemisphere. Given the BCS completeness limit of 90%, we estimate that we may have missed at most one northern cluster.

Of the 21 southern clusters, XBACs missed two found by REFLEX, and REFLEX does not list two found by XBACs, A2384 and A2426. Boehringer (priv. comm.) explained that A2384 is

[3]It turns out anything much fainter than our flux limit which is within a $z < 0.1$ range does not have sufficient luminosity to be a significant SZE source anyway. Even some of the clusters in our sample are a bit marginal relative to the CMB, but we did not know this until after all the observations were planned and taken.

Table 2.2 Clusters found in each of the four RASS Surveys.

	Cluster	RA J2000	Dec J2000	XBACs All-sky	BCS Northern	NORAS Northern	REFLEX Southern
1	A85	00:41:48.7	−09:19:04.8	x	-	-	x
2	A399	02:57:49.7	+13:03:10.8	x	x	x	-
3	A401	02:58:56.9	+13:34:22.8	x	x	x	-
4	A3112	03:17:56.4	−44:14:16.8	x	-	-	x
5	A3158	03:42:43.9	−53:38:27.6	x	-	-	x
6	A478	04:13:26.2	+10:27:57.6	x	x	x	-
7	A3266	04:31:25.4	−61:25:01.4	x	-	-	x
8	A754	09:09:01.4	−09:39:18.0	x	-	-	x
9	A780	09:18:06.7	−12:05:56.4	x	-	-	x
10	Z5029	12:17:41.3	+03:39:32.4		x		-
11	A1650	12:58:41.8	−01:45:21.6	x	-	-	x
12	A1651	12:59:24.0	−04:11:20.4	x	-	-	x
13	A3558	13:27:57.8	−31:29:16.8	x	-	-	x
14	A3571	13:47:28.1	−32:51:14.4	x	-	-	x
15	A2029	15:10:55.0	+05:43:12.0	x	x		-
16	PKS1550-140				-	-	x
17	A3667	20:12:23.5	−56:48:47.0	x	-	-	x
18	A3695	20:34:46.6	−35:49:48.0	x	-	-	x
19	A2384	21:52:16.6	−19:36:00.0	x	-	-	
20	A3827	22:01:56.6	−59:57:14.4	x	-	-	x
21	A2420	22:10:20.1	−12:10:49.0		-	-	x
22	A2426	22:14:32.4	−10:21:54.0	x	-	-	
23	A3911	22:46:20.9	−52:43:30.0	x	-	-	x
24	A3921	22:49:48.0	−64:23:00.0	x	-	-	x
25	A2597	23:25:16.6	−12:07:26.4	x	-	-	x
26	A4010	23:31:14.2	−36:30:07.2	x	-	-	x

x: the cluster was found by the survey
-: the cluster falls outside the sky coverage of that particular survey.
blank: the cluster was within the range of the survey but was not detected.

actually a double cluster whose components are separated by about $12'$, and in their catalog, they list them as separate clusters. Their combined flux would have met our sample criteria, but given the complexity of the system, we exclude the source from our sample[4]. The REFLEX group found a redshift of 0.1001 for Abell 2426, barely putting it outside the range of the sample. Thus, none of the other surveys found any clusters missed by REFLEX, and we presume that REFLEX is relatively complete within the redshift and flux limits of our sample. Overall, we estimate that the CBI sample contains >95% of clusters with $L_{0.1-2.4\mathrm{keV}} \geq 1.13 \times 10^{44} h_{100}^{-2}$ erg s^{-1} within a redshift of $z < 0.1$.

We list in Table 2.3 the 25 clusters that meet our selection criteria[5]. Since the X-ray surveys list redshifts from heterogeneous sources, where possible we use those from Struble & Rood (1999). One would expect the X-ray luminosity to correlate with SZE signal strength, so we list the clusters in order of descending X-ray luminosity, using values from REFLEX for the southern clusters (except for A2426), and from XBACs or BCS for the northern clusters. We converted the luminosities to units of h_{100} instead of h_{50}.

Of these 25 clusters, 18 are accessible with the CBI, as well as the OVRO 40-meter telescope and the VLA, which are necessary for foreground point source subtraction. An additional 7 clusters are too far south to be observed by the 40-meter and the VLA, but are accessible with the Australia Telescope Compact Array. We have noted in the table which clusters have public *ROSAT* and *ASCA* data available, as well as which clusters have been or are scheduled to be targeted with the *XMM-Newton* and *Chandra* observatories. The 15 most luminous clusters ($L_{0.1-2.4\mathrm{keV}} \geq 1.46 \times 10^{44} h_{100}^{-2}$ erg s^{-1}) still constitute a volume-complete sample, and since they have near complete X-ray observations available, we define this group to be our primary sample. For this sub-sample, we expect the completeness to be close to 100%. In our H_0 analysis we rely on X-ray models determined by Mason & Myers (2000). The clusters for which these are available are marked in Table 2.3.

[4]We did not obtain this information about A2384 being a double source until after we had already observed it with the CBI, so we have data for it, but it is not in our primary sample.

[5]We exclude the double cluster A2384, but include A2426.

Table 2.3 CBI SZE cluster sample, compiled from *ROSAT* cluster surveys (Ebeling et al., 1996, 1998; Boehringer et al., 2003). All redshifts are from Struble & Rood (1999) except those for Z5029 (Ebeling et al., 1998) and PKS1550-140 (Boehringer et al., 2003). Luminosities are from Boehringer et al. (2003) and Ebeling et al. (1996), except for Z5029 which is from Ebeling et al. (1998). The 15 clusters above the line represent the primary CBI sample.

Cluster	z	$L_{0.1-2.4\mathrm{keV}}$ $(h^{-2}10^{44}\mathrm{erg/s})^a$	*ROSAT*	*ASCA*	*XMM-Newton*	*Chandra*	CBI
A2029	0.0773	3.84	P*	y	G	S	y
A478	0.0881	3.24	P*	y	G	S	y
A401	0.0737	2.47	P*	y	G	I	y
A3667^S	0.0556	2.32	P*	y	G	I	y
A85	0.0555	2.15	P*	y	B	I	y
A3827^S	0.0984	1.95	H		B		y
A3571	0.0391	1.94	P*	y	B		y
A3266^S	0.0589	1.89	P*	y	G	I	y
A1651	0.0844	1.85	P*	y	B	I	y
A754	0.0542	1.80	P*	y	G	I	y
A3112^S	0.0750	1.79	P*	y	G	S	y
A399	0.0724	1.61	P*	y	G	I	y
A1650	0.0845	1.61	P	y	B		y
A2597	0.0852	1.48	P*	y	G	S	y
A3558	0.0480	1.46	P*	y	G	S	y
A3695	0.0894	1.44	H		B		
PKS1550-140	0.0970	1.42					
A3158^S	0.0597	1.37	P*	y		I	y
A3921^S	0.0936	1.32	P*	y	G		y
Z5029	0.0750	1.32				I	
A2426	0.0978	1.28			B		
A780	0.0539	1.23	P*	y	G	I,S	
A3911^S	0.0965	1.23	P		B		
A2420	0.0846	1.16					
A4010	0.0957	1.16					y

[a] XBACs, BCS, and REFLEX assume $h = 0.5$. We convert their luminosities to units of $h = 1.0$.
[S] Southern Source, not accessible with OVRO 40-meter or VLA
ROSAT : P = Public PSPC, H = Public HRI only, *=included in Mason & Myers (2000)
ASCA : y = public data available
XMM-Newton : G = Guaranteed Time Target, B = General Observer Target
Chandra : I = ACIS-I, S = ACIS-S

Figure 2.2 The Cosmic Background Imager at its site in northern Chile.

2.2 The Cosmic Background Imager

Now that we have described our sample, we proceed with a discussion of the observations undertaken for this thesis. The Cosmic Background Imager (CBI), pictured in Figure 2.2, is a 13-element radio interferometer operating at 26–36 GHz. It is located at an altitude of 5080 m (16,700 ft) in the Andes mountains near San Pedro de Atacama in northern Chile. The CBI is a specialized telescope that was designed to image CMB anisotropies on angular scales of $5'$ to 1°. At 31 GHz the telescope has a field of view of $44'$ FWHM (set by an antenna primary beam) and has resolution ranging from $4.5'$ to $10'$ (set by the synthesized beamwidth). The telescope specifications, summarized in Table 2.4, are extremely well matched to observations of the SZE in nearby rich clusters which have typically have size scales $\sim$tens of arcminutes.

Several design elements (Padin et al., 2002) are key to achieving the goals of the CMB and SZE observation programs. To attain arcminute resolution at 30 GHz (1 cm), the interferometer must have a compact design. The thirteen 0.9 cm CBI antennas are mounted on a single 6.5 m platform. Located on the antenna mount are 52 1-meter triangular cells, each with four possible antenna locations, which allow for a wide variety of array configurations. Figure 2.3 shows one configuration. Possible baseline lengths span a range from 1 m to 5.5 m, corresponding to $30'$ to $5'$ at 30 GHz.

Table 2.4 CBI specifications.

Observing frequency:	26–36 GHz (wavelength 1 cm)
Number of channels:	10 channels, each 1 GHz wide
Number of antennas:	13
Number of baselines:	78
Receivers:	HEMT amplifiers, cooled to 6 K
Correlator:	780 analog complex correlators
Antenna:	Cassegrain, 0.90 m diameter
Primary beam:	Gaussian FWHM 44 arcmin
Minimum baseline:	1.00 m ($\ell \sim 630$), or 0.58 m with smaller antennas
Maximum baseline:	5.51 m ($\ell \sim 3500$)
Synthesized beamwidth:	FWHM 4.5 - 8.0 arcmin, depending on configuration
System temperature:	20 K
Noise in visibility measurements:	3.3 Jy $s^{-1/2}$ rms in each 1-GHz channel
Noise in image from a single pointing:	4 mJy/beam rms in 900 s, 10 channels, at center of primary beam
Polarization:	Circular (RCP), giving images of Stokes I. Images of Q and U can be made (more slowly) by switching some antennas to LCP and cross-correlating L and R

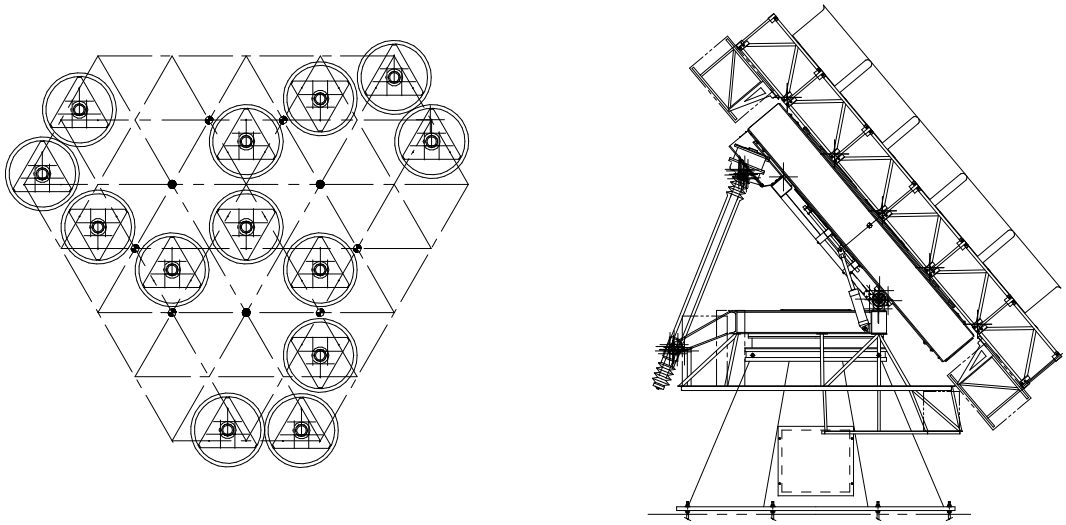

Figure 2.3 CBI mount design.

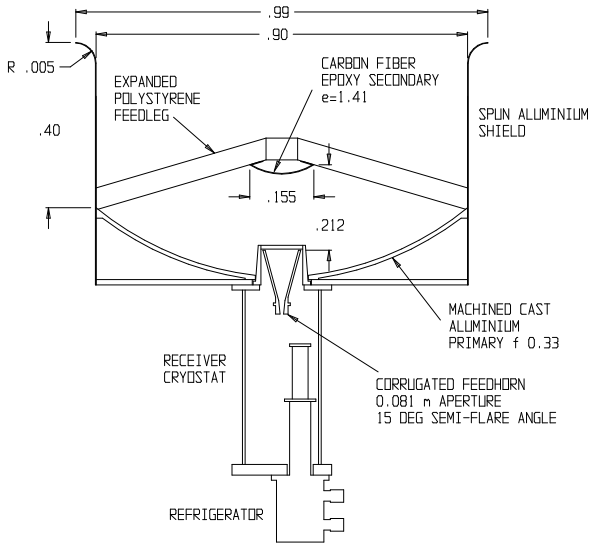

Figure 2.4 CBI antenna design. Dimensions listed are in meters.

The planar array design has many advantages. In a close-packed array, any cross talk between antennas remains constant while tracking a source. Also, the signal processing is simplified since fringe rotators or tracking delays are unnecessary. The CBI has an elevation-azimuth mount which includes an extra degree of freedom where the entire telescope platform can be rotated about the optical axis of the telescope. The ability to rotate the platform (known as a "deck rotation") is useful in many ways. It provides a straightforward method of improving the (u, v) coverage of the interferometer, and it allows many important diagnostic checks on our observations. For example, antenna cross talk and other constant spurious signals stay the same as the deck is rotated, while astronomical sources do not. The rotating deck also allows us to track a source with constant parallactic angle, which is normally not possible for an elevation-azimuth telescope. The CBI telescope mount yields $\sim 2''$ axial errors, and has a worst case gravitational deformation of 50 μm in the surface of the antenna platform. These correspond to a maximum visibility phase error of $\sim 5^\circ$ on the longest baselines.

For CMB anisotropies $\frac{\Delta T}{T} \sim 10^{-5}$, and for typical clusters, the SZE gives $\frac{\Delta T}{T} \sim 10^{-4}$. Observations of such small signals require extremely high sensitivity. This is achieved by working with a large bandwidth (ten 1-GHz channels), and minimizing noise. Because the antennas are so compact,

the far field is only ∼100 m from the telescope, so most of the atmosphere is imaged, and a high, dry site was chosen to decrease atmospheric brightness fluctuations. The antenna receivers have been equipped with low-noise high electron mobility transistor (HEMT) amplifiers which provide receiver temperatures of 15 K to 20 K across the ten CBI channels. All receiver components, including the feed horn are cooled to 6 K. The antennas have a Cassegrain design, with secondaries made from lightweight carbon fiber reinforced epoxy. The feedlegs supporting the secondaries are made from expanded polystyrene foam which is essentially transparent at 1 cm and scatter very little. A close-packed array with a high filling factor provides the greatest sensitivity. To reduce cross talk, each antenna is shielded with cylindrical metal cans whose edges have been rolled with a radius of a few wavelengths, to minimize scattering from the shield itself. With the shields in place, maximum coupling between antennas in each 1 GHz band is -110 to -120 dB (a factor of 10^{-11} to 10^{-12}). Assuming a receiver temperature of 15 K, the level of expected false signals is $\sim 0.5-1.5\mu$K, compared to a typical cluster signal of several hundred μK. A schematic of the CBI antenna design is shown in Figure 2.4.

The final major factor in the success of the CBI is the correlator design. The 13 antennas yield 78 baselines; 10 separate channels mean that 780 complex correlations must be performed for each integration. The CBI budget did not allow for a digital correlator, so an analog was used. A cooled downconverter shifts the input 26–36 GHz band to 2–12 GHz. Each receiver signal is then split into ten 1 GHz bands which are each downconverted to 1–2 GHz. An array of Gilbert Cell multipliers then computes the real and imaginary parts of each cross correlation. Each of the 10 correlators (one for each channel) handles 78 baselines and measures 3"×5"; one is shown in Figure 2.5.

2.2.1 CBI Observations

After a period of extensive testing on the Caltech campus during the summer of 1999, the CBI was shipped to its current site. The small CBI group size led to a great deal of hands-on experience for the graduate students. I participated in activities ranging from cataloguing the entire contents of the CBI shipment to Chile for customs, to exciting events such as obtaining "first light" on Jupiter

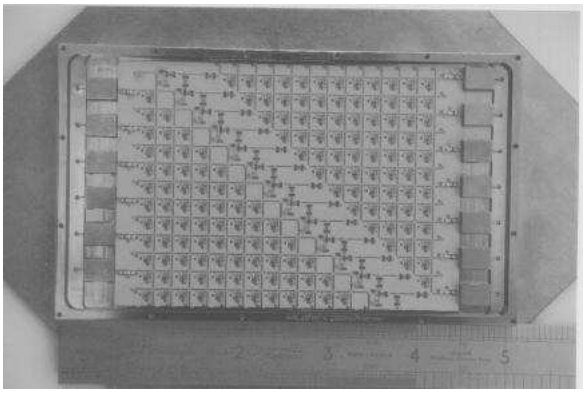

Figure 2.5 One of 10 CBI analog correlators, about the size of a postcard.

during testing on the Caltech campus. Being neither terribly proficient with hardware, nor much good at heavy lifting, my main contribution to the project outside of running the SZE program has been in observing. After the telescope became operational in November 1999, I was summoned for my first of four trips to Chile four days before Thanksgiving and experienced the stimulating early detective work required to debug the new system. Ultimately, I spent a total of 8 months in Chile (November–December 1999, January–March 2000, August–November 2000, and April-May 2001), logging about 80–90 nights of observing.

The main observational difficulty we encountered early on was ground spillover contamination, which on 1-meter baselines generally contributes between a few tens and a few hundreds of mJy of signal, but can be as high as a few Jy. We ran multiple tests in an effort to understand how the spillover was entering the feeds. For example, we placed shields of various heights between a pair of antennas to see if increasing the shield can heights would reduce the problem, but we found that they usually made the problem worse somewhere else. Spillover is most severe for sources at low elevation when the fringe pattern on some of the short baselines can remain roughly parallel to the horizon as we track a source. We considered building a ground shield, but in order to block out low horizon signals entering via the distant antenna side lobes, the shield would have been impractically large, especially given the site wind levels, which have peaked as high as 45 m s^{-1}. Also, a rigid structure that could withstand the wind would have accumulated snow during the winter. Tests showed that the spillover signal remains very constant on hour timescales, since the ground temperature does not

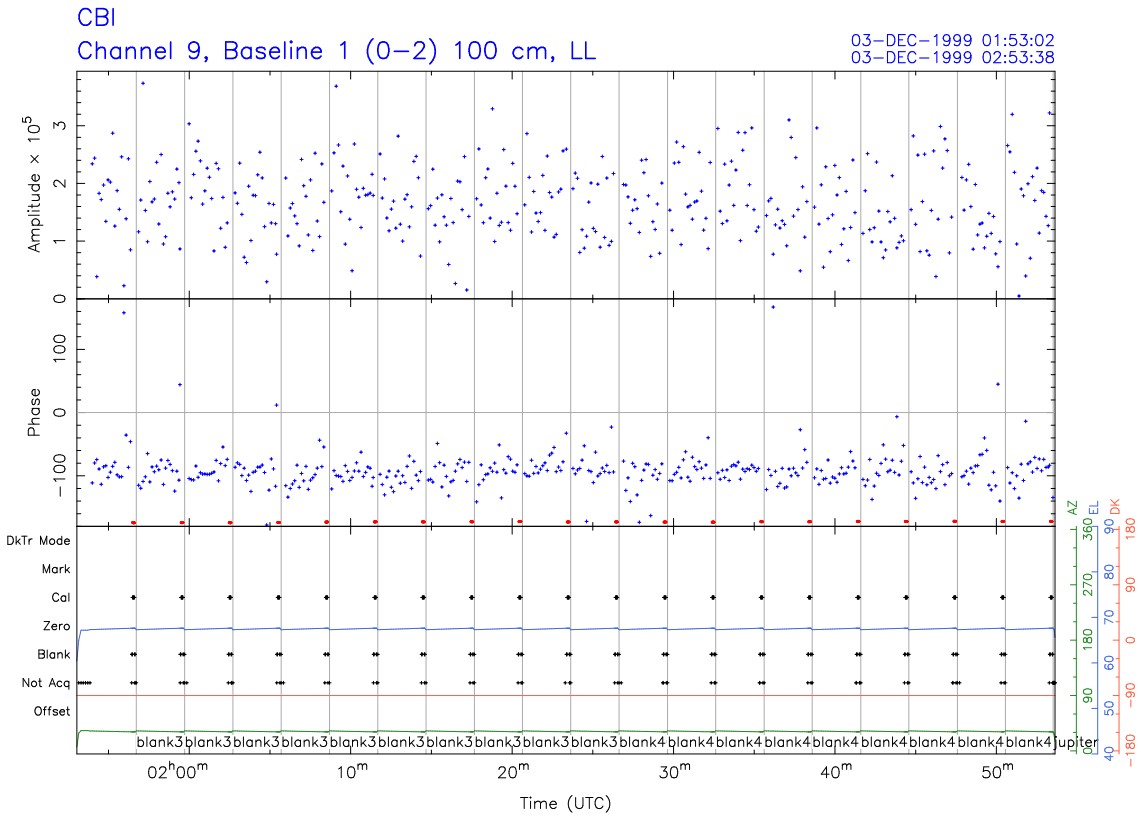

Figure 2.6 Plot of CBI visibilities with time for consecutive blank patches of sky used to measure the repeatability of the ground signal.

change significantly over the night. Figure 2.6 shows a plot of CBI observations from December 3, 1999, of blank patches of sky observed in succession over the same hour angle range. This particular plot shows the visibility data for one of 780 CBI baselines, with the top plot being the amplitude, the middle the phase, and the bottom tracking various telescope parameters including the azimuth, elevation, and deck angles. Each of the blank sky patches was observed for about three minutes, and the telescope tracked over the same elevations and azimuths with respect to the ground signal each time. Shown in the plot is a signal which is clearly not consistent with the random noise expected for a blank field, and is very constant with time. This is the ground spillover.

Given the repeatability of the ground signal with time, we chose to remove it from the data by employing a differencing scheme like that used by Myers et al. (1997) and Mason et al. (2001) in their OVRO 5-meter SZE observations. In the differencing scheme, we observe two or three fields

in succession at the same hour angle, so the orientation of the telescope relative to the ground is identical for each scan. For observations of CMB fields, we used a lead-trail (L-T) differencing scheme where two different CMB fields are observed in succession. Since the CMB appears as Gaussian fluctuations, the differencing simply increases the signal by a factor of $\sqrt{2}$, which is taken into account in the analysis. This removes the ground signal and any other spurious signals, with the level of potential residuals being $< 1.3\%$ of the primary anisotropy signal (Padin et al., 2002).

The CMB primary anisotropies are the largest source of contamination in the SZE observations, and L-T differencing would also increase this source of noise by $\sqrt{2}$. For cluster observations, we therefore used a lead-main-trail (LMT) differencing scheme where an average of the lead and trail fields was subtracted from the main field. This increases the required observing time by 50%, but it reduces the increase in CMB noise from $\sqrt{2}$ to $\sqrt{3/2}$. While we have not measured the level of residual contamination from the LMT differencing scheme, it should be better than that from L-T differencing, since any linear changes in time will cancel out in the lead and trail fields. Furthermore, any residual signal will be much smaller than the primary anisotropy signal, and would be negligible by comparison.

Other observational issues that appeared early on included understanding the telescope pointing. During the diagnostic phase, we performed regular pointing tests, where an optical telescope mounted on the antenna platform was used to observe a series of bright stars. The stars chosen were distributed over a range of elevations and azimuths, and one star of average elevation was used to measure the pointing over a 360° range of deck angles with spacings of 30°. A camera connected to a monitor in the control room showed the observer where the star was located relative to where the telescope was actually pointing, and the observer could input pointing offset corrections to adjust for the observed errors. Given the offsets across the sky, a new pointing model could be derived. Early on, we found that the pointing model was changing significantly by about $20''$– $30''$from night to night, and even over the course of one night. We determined that the pointing changes were caused by expansion and contraction of the telescope due to temperature fluctuations, as well as from the entire telescope platform settling into the ground at its new site. Tilt meters which measured how the telescope was

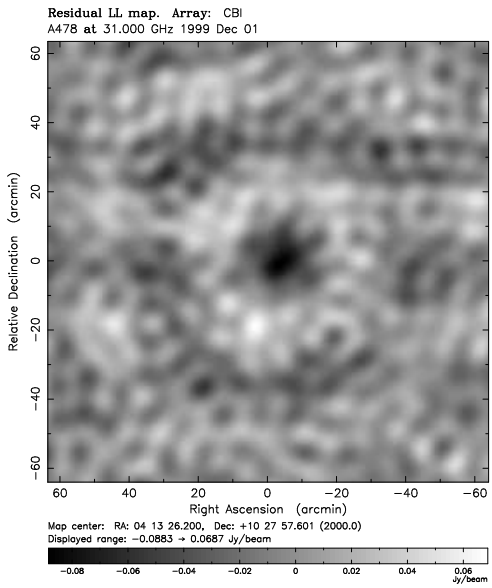

Figure 2.7 First cluster image taken with the CBI. The dark central region shows the SZE decrement from the cluster. This is a dirty map, so the bright ring around the cluster is due to the synthesized beam sidelobes.

oriented relative to the ground were successful in maintaining more stable pointing at the $\sim 15''$level. To monitor pointing offsets, we also observed a bright ($\sim$ 1 Jy) source near the fields ($\lesssim 20^\circ$) at each deck angle, which allowed us to determine the magnitude of pointing errors. We found that the absolute rms radio pointing was $\sim 22''$, and the rms tracking errors were $\sim 2''$. These errors are very small compared to the CBI $45'$ primary beam and the $4'$ synthesized beam, and we have performed Monte Carlo simulations which show that random pointing errors of this magnitude do not bias our H_0 results.

After the debugging and initial test phase, the first science observations taken were of a cluster, A478. This cluster is one of the strongest in the sample, and is relatively free of point source contamination. Figure 2.7 shows the first map of A478 made on December 1, 1999 after 1 night of observing, with 1.3 hours spent on each of the lead, main, and trail fields. The noise in the map is 13 mJy/beam, but already the cluster is clearly visible. Soon after we took these observations and determined that the telescope was operating properly, a regular nightly observing routine was established.

We now discuss a few other factors we had to consider in planning CBI observations. The CBI

1-meter baselines are most sensitive to emission on $\sim 30'$ scales, so contributions from the sun and moon are potential contaminants. To avoid the sun, we observed only at night, and observations of CMB and SZE fields were used only if the angular separation from the moon was at least 60°. We estimate any residual contamination from the moon to be $< 1 - 2\mu$K.

Another feature of the CBI is its reconfigurability. We changed the telescope configuration several times during this period, optimizing the system at different times for the CBI's polarization study (Cartwright et al., in prep), and intrinsic anisotropy observations at both low ℓ (Pearson et al., 2003) and high ℓ (Mason et al., 2003). The sensitivity of the SZE observations was not significantly affected by the changing configurations.

We also took advantage of the CBI design which allows us to rotate the telescope about the optical axis, increasing the (u, v) coverage in our observations. We rotated the deck about the telescope optical axis by 10° between LMT groups. To demostrate the improvement gained from being able to observe with multiple deck angles, Figure 2.8 shows two plots of the (u, v) coverage and their corresponding beam maps with and without deck rotations[6]. The closely spaced radial spokes in groups of ten indicate the slightly different (u, v) locations produced by the ten different frequency channels.

2.2.2 SZE Observations

We took observations of the SZE between November 1999 and September 2001, with a few supplemental observations taken in April 2003. Early simulations showed that integration times of 5 hours on each LMT field per cluster would yield sufficient sensitivity for the H_0 analysis. For some southern clusters, we acquired significantly more data than this because they were often the only CBI sources that could be observed during certain periods because of the moon. Since independent observations of the point sources are not yet available for these particular clusters, the extra data will allow us to remove the point sources using the long CBI baselines. To minimize variability

[6]In retrospect, we may have gone a little bit overboard in performing so many closely spaced deck rotations. The data sets ended up being rather unwieldy in size since there are a large quantity of non-redundant data points. This has implications for determining covariance matrices as discussed in Chapter 5, but we did not know when we planned the observations that this would be an issue.

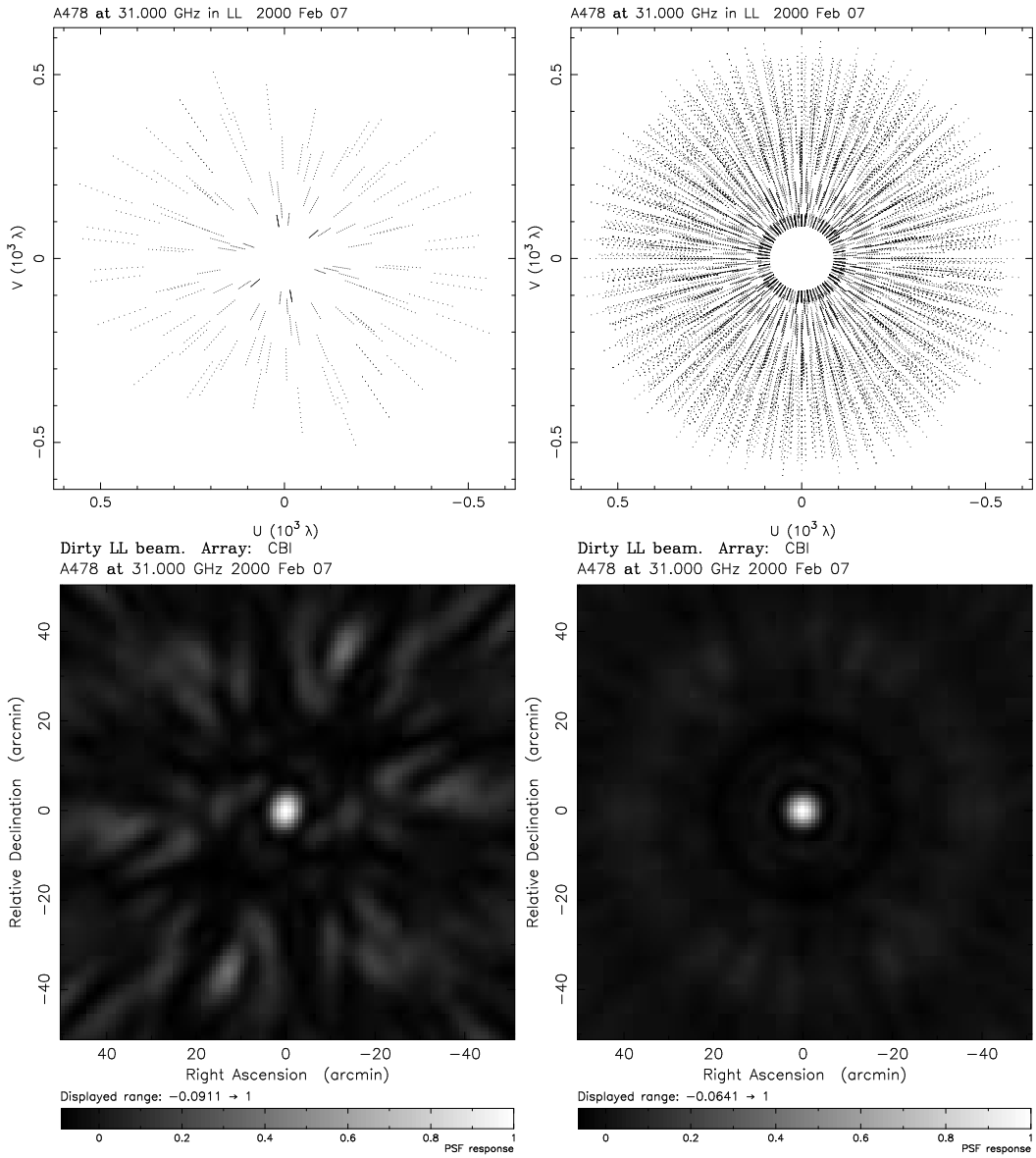

Figure 2.8 Examples of the actual (u, v) coverage for the CBI and corresponding beam maps without deck rotations (left) and with multiple deck rotations (right).

Table 2.5 Summary of SZE observations. The offsets in R.A. for the lead and trail fields are listed in minutes. The listed rms noise is for the map where the average of the lead and trail fields has been subtracted from the main field, M-(L+T)/2. The clusters below the line had been observed before we redefined the sample. Most of those are low luminosity and not good detections.

Cluster	L&T offsets (min)	Hours Observed (L+M+T)	rms noise (mJy/beam)	Beam FWHM (′)
A85	±16.5	16.6	1.8	5.3
A399	±12.5	15.6	2.0	5.4
A401	±12.5	15.7	2.0	5.4
A478	±10	12.2	2.4	5.2
A754	±9	16.0	1.9	5.4
A1650	±13.5	15.4	2.3	5.0
A1651	±11	16.3	2.0	4.9
A2029	±10.5	14.5	2.3	5.0
A2597	±15.5	11.6	2.3	5.5
A3112	±8	19.5	1.8	5.4
A3266	±8	25.4	1.7	5.4
A3558	±8.5	14.7	2.0	4.9
A3571	±9.5	15.8	1.7	4.8
A3667	±8	19.3	1.7	4.9
A3827	±8	16.8	1.7	4.8
A2384	±16	15.4		
A3158	±8	21.2		
A3921	±8	9.6		
A4010	±8	7.9		

from foreground point sources, we tried to observe each cluster within as short a time span as was feasible, given the constraints of other observational programs. Many clusters were observed over 4−5 consecutive nights, although some clusters were observed over up to 10 nights spanning a few months.

Table 2.5 summarizes the cluster observations, listing the dates they were taken, the total integration time on source, and the sensitivity achieved. We used the NRAO VLA Sky Survey (NVSS, Condon et al., 1998) to select lead and trail fields where the contamination from point sources was minimized. For southern clusters outside the range of NVSS, we chose a standard separation of 8 minutes. LMT separations range from 8 minutes to 16.5 minutes in right ascension. Table 2.5 also lists the lead, main, and trail pointing positions used for each cluster.

2.2.3 Calibration

The basic calibration process includes quadrature calibration, noise-cal calibration, and astronomical calibration. The quad cal adjusts the correlator output to match the real and imaginary gains and to give their phases the expected 90° offset. In the noise-cal procedure, an internal noise source injected into the front of each receiver is used to calibrate the amplitude and phase of the visibilities. After correction, the correlated response to the noise source has a zero phase and amplitude proportional to the noise strength as measured by an independent power meter. Finally, the phase calibrated data are then tied to an astronomically based flux scale through comparisons with sources of known flux density.

2.2.3.1 Quadrature Calibration

In an ideal correlator, the real and imaginary visibilities have identical amplitudes, and their phase offset is 90°. In an actual correlator, instrumental imperfections cause mixing between the real and imaginary channels, leading to mismatched gains and phase shifts which may deviate from 90°. Such an instrument's output can be modelled as

$$\begin{aligned} R' &= R \\ I' &= (H\cos\phi)I - (H\sin\phi)R, \end{aligned} \tag{2.3}$$

where R and I are the actual real and imaginary amplitudes, R' and I' are the output real and imaginary amplitudes, H is the gain of I relative to that of R, and ϕ is the quadrature phase error. The quadrature error, $He^{i\phi}$, is measured via a "quad" procedure, where the internal noise source is injected into each receiver with and without a 90° phase shift, and the visibilities with all the other receivers are measured. The quadrature calibrated correlator output is then

$$\begin{aligned} R &= R' \\ I &= \frac{I'+(H\sin\phi)R'}{H\cos\phi}, \end{aligned} \tag{2.4}$$

for each of the 78 baselines and 10 channels. The corrections are stable over timescales of several weeks, but since quad procedures only take about 5 minutes, we performed them at the beginning and end of every night of observing. The rms quadrature phase error among baselines was $\sim 5^\circ$, and the rms gain error was $\sim 10\%$.

2.2.3.2 Noise-cal Calibration

We bracketed each of the LMT cluster scans and calibrator scans with 10 second measurements of an internal noise source, whose equivalent flux density ($\sim$2000 Jy) for each baseline and channel is referenced from the celestial primary calibrators. We originally intended to use the noise source to remove instrumental gain fluctuations throughout the night, but we found that the gain fluctuations ($\sim$ 3% rms variations) were more stable than the fluctuations in the noise source itself, so all of the noise source measurements were averaged together over the night. The individual baselines were then rescaled to give the same response. This removed baseline-based gain and phase calibration errors, but introduced antenna based amplitude errors which were removed through the subsequent primary flux density calibration.

2.2.3.3 Antenna Calibration

The data were calibrated through nightly observations of one or more primary flux calibrators, Taurus A, Virgo A, Jupiter, or Saturn, which were chosen for their brightness and lack of variability at the CBI frequencies. A set of secondary flux calibrators (3C279, 3C273, J1743−038, B1830−210, and J1924−292) were observed regularly and were used to calibrate the data on nights when all primary calibrators were not visible or were too close to the moon to be observed. On those nights, the flux densities of the secondary calibrators were bootstrapped from observations of the primary calibrators which were nearest in time. The CBI flux density scale is based on single dish measurements of Jupiter, showing $T_{\rm Jup} = 152 \pm 5$ K at 32 GHz (Mason et al., 1999). Jupiter has a complicated spectrum across the CBI bandpass, so we determined flux scales for the other 9 channels by transferring the Jupiter 32 GHz flux to TauA, which has a known power-law spectrum

of $\alpha = -0.299$ (Baars et al., 1977), where $S_\nu \propto \nu^\alpha$. We estimate that there is a 5% systematic uncertainty in our absolute calibration (Padin et al., 2001; Mason et al., 2003). Observations of the primary calibrators during the year 2000 showed random errors in calibration of 3% night-to-night. All the clusters were observed over at least 5 nights, so the maximum expected random calibration error for each cluster is $3\%/\sqrt{5} = 1.3\%$.

2.2.4 Data Editing

Data editing was done both automatically and manually. The telescope control system automatically flagged data taken during periods when the data may have been unreliable, such as when the telescope was not tracking properly, a receiver was warm, a local oscillator was not phase locked, or the total power of a receiver was outside the normal range. Notes in the observer log were used to examine periods where there were instrumental problems or bad weather, indicated by visible cloud cover or corrupted visibilities on the short baselines. Two percent of the data were removed on the basis of these inspections.

To perform the ground subtraction, we read in the CBI UV FITS files for the LMT fields, searched for scans with matching hour angles, averaged the visibilities of the L and T scans, and subtracted that average from the M scan. The large data files were compressed by averaging multiple integrations from a single scan. We calculated statistics on the noise of each scan, as shown in Figure 2.9. These noise plots assist the observer in monitoring whether a particular receiver or channel is beginning to have problems, and they allow us to visually inspect the data, looking for spurious signals from instrumental glitches or from the atmosphere during less optimal weather which were occasionally missed by the automatic flagging system in the control program. To reject these observations, we filtered out data with amplitudes that differed from the scan mean by more than five times the scan rms. This criterion rejected a negligible fraction of the data, and our results are not sensitive to the precise level of the cut. We also filtered out data whose scatter was more than two times the noise expected based on the integration time and the system properties. This rejected less than 0.1% of the data.

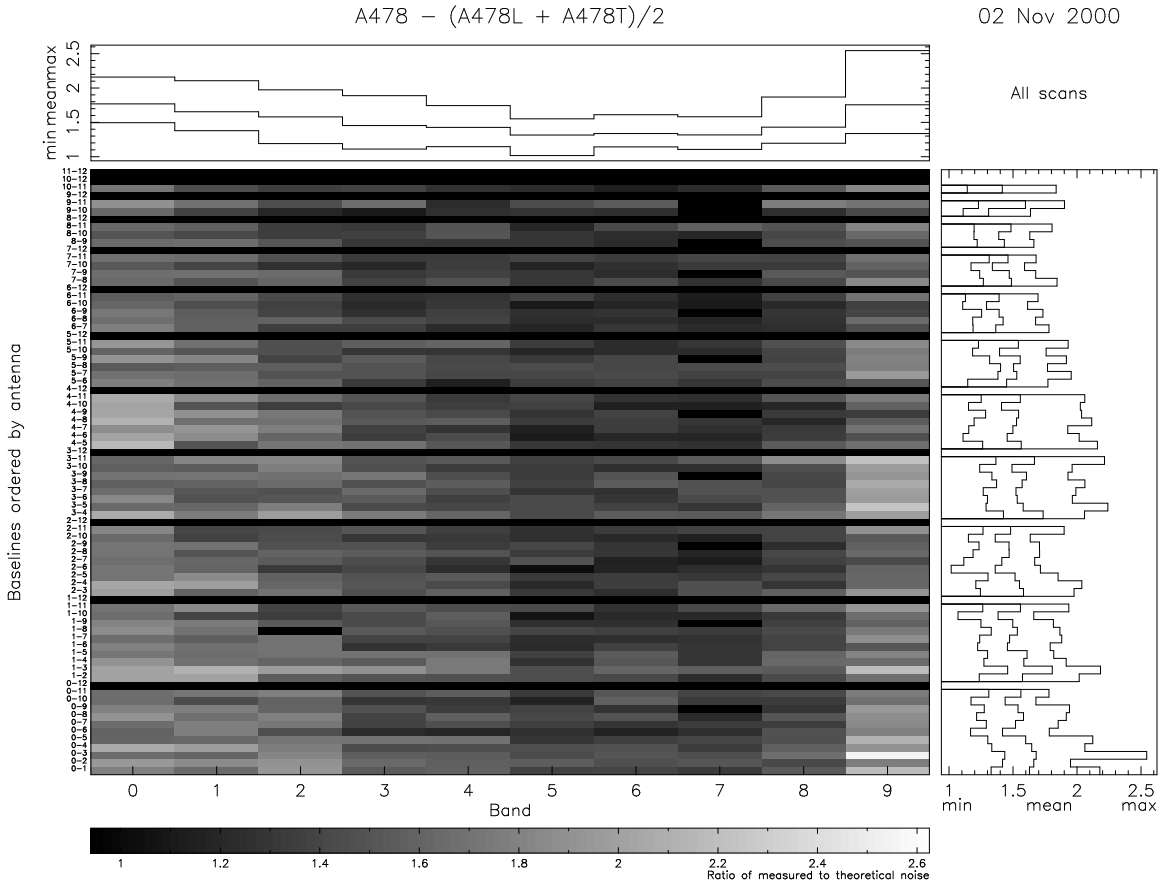

Figure 2.9 Example UVSUB plot showing measured noise on each baseline and channel.

2.3 Point Source Observations

Foreground radio point sources are the main source of contamination in CMB experiments at 30 GHz. The requirements for removing point sources are less stringent for the SZE observations, as we will detail in Chapter 4. Radio point sources present in all of the observations were subtracted through a combination of fitting on the CBI long baselines (> 2.5 m) and observations with the OVRO 40-meter telescope. Here we describe the 40-meter observations. Further details of the point source subtraction are presented in Section 4.4.4.

2.3.1 OVRO 40-meter Telescope Observations

The Owens Valley Radio Observatory is located at an elevation of about 1,200 m, and is 7 km north of Big Pine, CA, immediately east of the Sierra Nevada mountains. The OVRO 40-meter (130-foot) telescope, built in 1966, has an elevation-azimuth mount, and the dish is an f0.4 paraboloidal reflector made from 852 precision-contoured, lightweight aluminum panels. The surface accuracy is $\sim$1.1 mm rms, providing a maximal efficiency of about 10–15% at 30 GHz when the telescope elevation is about 50°. In 1998, a new Ka-band (26–34 GHz) receiver with four 2-GHz channels was built for the OVRO 40-meter telescope, which was then dedicated to CBI support observations.

2.3.1.1 Single Dish Telescope Basics

We first briefly describe basic observing and calibration techniques with a single dish telescope. A detailed overview can be found in Leitch (1998). The Ka-band receiver has two feed horns offset from each other in the azimuthal direction; one is called the antenna (ANT) horn and the other is the reference (REF). The horns have nearly identical Gaussian response patterns with a FWHM of $\sim 1.35'$, and the beam throw (the separation between the horns), is $7.6'$. The signals from the ANT and REF enter a Dicke switch which toggles between them at a rate of 125 Hz. The output signal is passed through an amplifier chain which includes a HEMT that is identical to those used in the CBI receivers. The measurements from each horn are accumulated over a 1 s integration period, and both the mean difference and the standard deviation of the mean difference are recorded over the 1

s period. This rapid switching removes noise from system gain variations in the amplifier system.

The standard radiometry measurement is a FLUX procedure, where 4 successive measurements are taken with the REF on source for integration A, the ANT on source for B and C, and the REF on source again for D. During each integration period (the same for all steps and typically ∼20 s), the switched difference between the ANT and REF temperatures is recorded, and the individual integrations are normalized and calibrated. The FLUX is then given by

$$\mathrm{FLUX} = \frac{1}{4}(B + C - A - D). \tag{2.5}$$

This second level of switching removes power gradients due to atmospheric and ground emission signals that are stable on minute timescales.

The data are calibrated through comparisons with an internal noise diode measurement. Nonlinearity in the receiver response causes the system to respond differently depending on the total power entering the system. The system uses a 16-bit digitizer, with a detectable power range between 0–65,536 digitizer units (DU). For a measurement made in the presence of a typical background level of 30,000 DU, the power increment at the front of the feeds can be underestimated by as much as 10–20% due to nonlinearity, and this must be corrected for. Because of the nonlinearity, two diodes are used. One of the two diodes, called the CAL, is injected behind an attenuator, producing a small power increment which is suitable for comparisons with astronomical signals. The stronger NOISE diode provides a significant power increase that is used to calibrate the system temperature. By comparing its output power with hot (300 K) and cold (77 K) loads filling the beams, we can measure the NOISE diode temperature as well as the receiver temperature. The CAL diode temperature is obtained through a comparison with the NOISE diode temperature, combined with a measurement of the nonlinearity.

System gain fluctuations are removed by dividing FLUX measurements by CAL measurements over the same time period. A CAL procedure is performed every 10–20 minutes and is similar to a FLUX procedure in that it has four segments, but instead of switching the ANT and REF on and off

source, the CAL diode is switched off during the A and D integrations, and on during the B and C integrations, while the telescope remains stationary. After the FLUX measurements are divided by the CAL measurement, they are converted to antenna temperature by multiplying by the measured CAL diode temperature. A conversion to standard flux density units can be made by comparing the CAL diode with radio sources of known strength. The equivalent flux density of the CAL diode is given by

$$\frac{S_{\rm cal}}{T_{\rm cal}} = \frac{2k_B}{A_p \eta_A}, \tag{2.6}$$

where A_p is the physical area of the telescope, and η_A is the telescope efficiency.

2.3.1.2 System Characterization

The 40-meter telescope was designed to operate at much lower frequencies than 30 GHz, and we had to characterize both the new receiver and the properties of the telescope at high frequencies. Before any observation is taken, the telescope must be focused and pointed. The optimal focus changes with elevation because gravity deforms the telescope dish. The pointing procedure involves observing a bright radio point source at several positions offset by half a beam FWHM in the positive and negative azimuth (AZ) and ZA (zenith angle) directions, and solving for a pointing offset that would yield a maximum in flux, assuming a gaussian beam. We found early on that the control program was having difficulty finding optimal solutions for faint and moderately bright sources. We had thought that perhaps the default pointing model was inaccurate, but we found the problem to be with the focus curves, which appeared to be changing with time. At first, we thought the focus curve could be a function of both elevation and temperature, since the telescope did focus accurately during certain times of day. Including a temperature component improved the focusing considerably, but the solutions were not repeatable over long periods. In other words, the focus curve in January 1999 for 5° C did not agree well with the curve for the same temperature in Februrary 1999.

The standard procedure to measure a focus curve is to observe a bright source over a range of elevations, stepping the focus over a range of positions and fitting for the positions which gives the maximum flux. In order to determine how the focus curves were changing, we needed to quickly

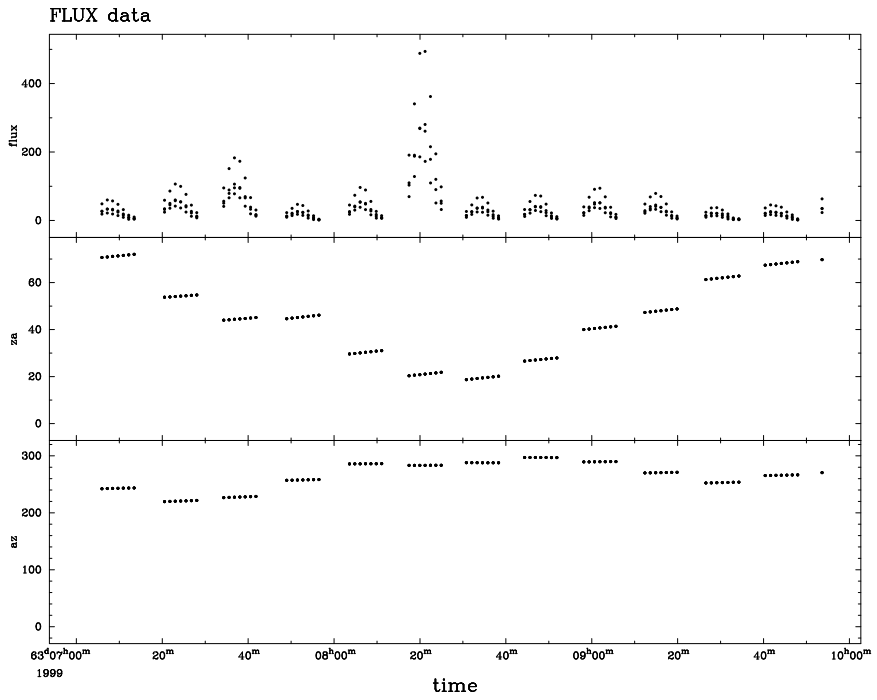

Figure 2.10 Focus data from CMBPROG.

measure a single focus curve over a range of elevations in a short amount of time. Instead of waiting for a single source to cross the sky, we selected the brightest calibrator sources from the VLA Calibrator Manual (Perley & Taylor, 2003), and selected groups of sources that spanned a range of elevations and could be used to determine a focus curve within about an hour. Figure 2.10 shows an example of 40-meter data taken in this way. The top panel shows the response to the source in each of the four channels, and the resulting parabolas from stepping through the different focus positions. The middle plot shows the source ZA, and the bottom plot shows the source AZ. We tried correlating the focus curve solutions with various other parameters, and found through trial and error that the focus curves are a function of elevation and sun angle. The top plot in Figure 2.11 shows a focus curve derived for one particular range of sun angles, and the bottom plot shows the fit residuals. We wanted to be sure that the residuals would not cause errors in flux greater than 2%; the dashed curve in the bottom plot shows the boundary, outside which flux errors would be greater than 2%. For sun angles >70°, we found that the rms of the residuals to the fit in each sun angle bin is of order 1 mm, and the fraction of points with residuals large enough to produce flux

Table 2.6 40-meter Ka-band system temperature (from Sep 99). $T_{\rm sys} = T_{\rm rx} + T_{\rm sky} + T_{\rm grd} + T_{\rm CMB}$

Band (GHz)	$T_{\rm rx}$ (K)	$T_{\rm sky}$/Airmass (K)	$T_{\rm grd}$ (K)	$T_{\rm sys}$ (K)
26–28 (A)	38.7±0.6	12.8 ±3.0	8.2±3.0	59±4
28–30 (B)	22.1±0.3	13.4 ±0.3	9.0±0.3	46±1
30–32 (C)	20.0±0.2	13.0 ±0.3	9.2±0.3	46±1
32–34 (D)	23.9±0.2	11.7 ±0.3	11.7±0.3	54±1

errors greater than 2% is fewer than 5%.

The observed fluxes must also be corrected for the telescope gain which is also a function of elevation, since the dish deformation varies with elevation. In October 1999 and May 2000, we observed 3C345 and 3C84 to determine the gain curves by tracking both sources over a wide range of elevations. The rms of the residuals to the gain curve fit in each band were about 2% for 3C84, which was observed mostly at night, and about 4% for 3C345, which was observed mostly during the day. The gain curves fitted to both sources yielded an rms of about 3% in each band. In all bands, the gain curves derived from 3C84 and 3C345 agreed with each other to about 5% between 0 and 60 degrees ZA. Figure 2.12 shows the gain curves for all four bands derived during different epochs, demonstrating the repeatability of the measurement over long time periods with varying weather conditions. The focus curves as a function of sun angle and elevation have been very repeatable over timescales of a year.

Atmospheric opacity also attenuates the measured flux and must be corrected for. The attenuation reduces the source intensity by a factor $e^{-\tau \sec \theta_Z}$, where θ_Z is the zenith angle, and τ is the optical depth. By performing sky dips (a measurement of antenna temperature vs. airmass), one can measure the opacity and the ground temperature. At 31 GHz, $\tau \sim 0.045$. Typical receiver, sky, and ground temperatures are listed in Table 2.6. Those plus the CMB temperature give the total system temperature. The CAL temperatures, and the telescope efficiency and beam sizes are listed in Table 2.7.

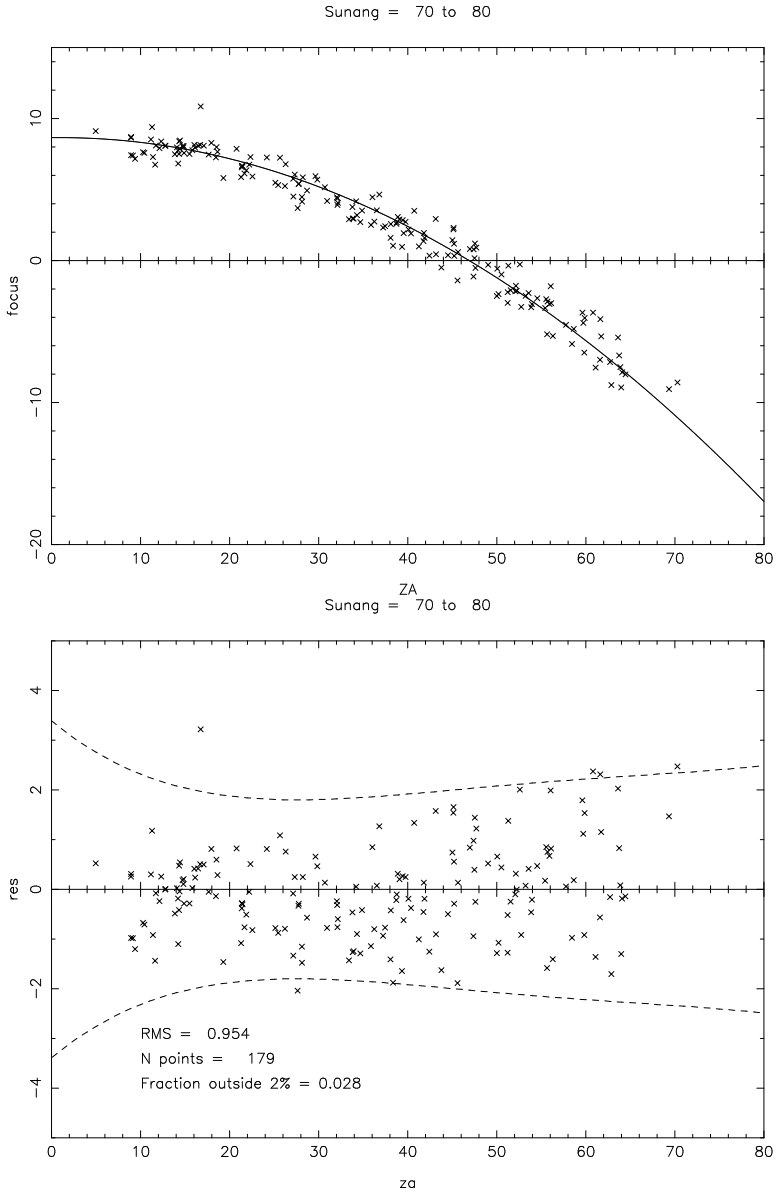

Figure 2.11 Focus curve and residuals for one sun angle bin. The y-axis units are mm. The dashed curve in the bottom plot bounds the region outside which flux errors would be greater than 2%.

Table 2.7 40-meter system properties

Band (GHz)	$T_{\rm CAL}$ (K)	η_A (%)	Beam FWHM ($'$)
26–28 (A)	0.34±0.01	14.7	1.44
28–30 (B)	0.73±0.01	14.4	1.38
30–32 (C)	1.28±0.01	13.4	1.34
32–34 (D)	1.76±0.01	11.6	1.28

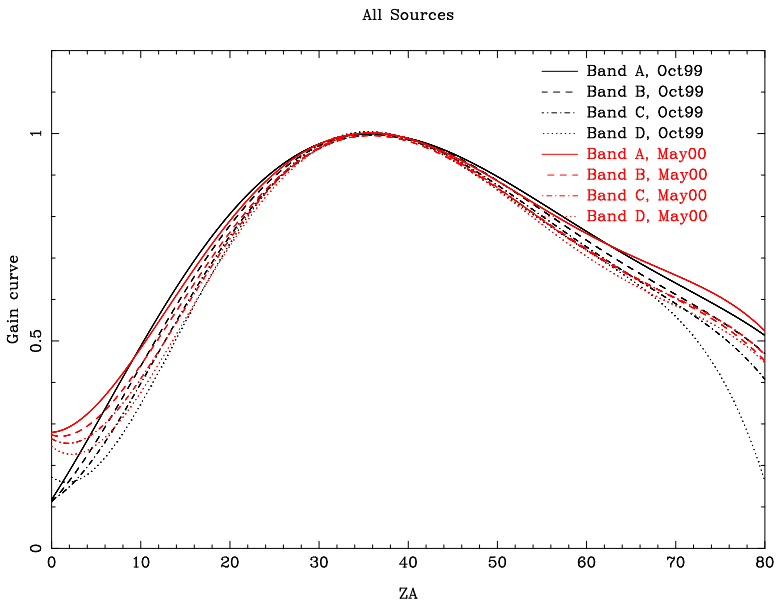

Figure 2.12 40-meter gain curves for all four bands during different epochs, to demonstrate repeatability.

2.3.2 OVRO 40-meter Measurements for SZE Clusters

After the initial calibration phase in the spring (and rechecked in the fall) of 1999, we observed point sources for both the CMB and SZE programs continuously until the telescope was decommissioned in the fall of 2002. For the SZE observations, we can usually fit for the flux density of bright sources using the long CBI baselines. However, this process is unreliable for sources close to the cluster centers, and we rely on 40-meter observations for all NVSS (with $S_{1.4\mathrm{GHz}} > 2.5$ mJy) point sources within $10'$ of the LMT pointing centers of each cluster. The sources we observed and the measured flux densities are presented in Table 2.8. Most of the sources have steep spectra and are not detected at 31 GHz. The sources which we detect at the 3-σ level are listed in the table in boldface. In total, we observed 126 sources in 9 clusters, with 27 3-σ detections. Six of the clusters in our sample are lacking point source measurements because they are too far south to be observed with the OVRO 40-meter.

Table 2.8. 40-meter observations of SZE point sources.

Cluster (L+M+T=N Sources)	Source	RA (J2000)	Dec (J2000)	Flux (mJy)	Error (mJy)
A85	002509-0918	00:25:09.90	−09:18:22.5	-0.2	1.6
(2+11+8=21)	002545-0922	00:25:45.21	−09:22:40.4	0.3	1.3
	004129-0922	00:41:29.21	−09:22:40.0	-3.4	1.6
	004130-0915	00:41:30.36	−09:15:45.9	-0.7	1.5
	004131-0927	00:41:31.86	−09:27:55.6	1.4	1.7
	004134-0920	00:41:34.83	−09:20:57.9	-1.9	1.1
	004141-0914	00:41:41.35	−09:14:13.6	-0.1	1.1
	004147-0916	00:41:47.91	−09:16:41.6	-1.5	1.4
	004148-0920	00:41:48.12	−09:20:41.7	-1.1	1.2
	004150-0918	00:41:50.38	−09:18:13.7	-0.1	1.1
	004151-0925	00:41:51.49	−09:25:48.5	6.1	1.5
	004156-0925	00:41:56.43	−09:25:41.2	2.0	1.6
	004158-0916	00:41:58.61	−09:16:46.8	2.4	1.5
	005740-0917	00:57:40.60	−09:17:44.3	7.0	1.9
	005752-0921	00:57:52.30	−09:21:28.4	1.8	1.6
	005752-0917	00:57:52.46	−09:17:17.3	-5.5	2.0
	005801-0921	00:58:01.31	−09:21:22.8	-2.8	1.9
	005809-0922	00:58:09.21	−09:22:49.1	-1.3	1.8
	005836-0919	00:58:36.16	−09:19:01.9	-0.1	1.4
	005838-0925	00:58:38.74	−09:25:52.9	2.4	1.6
	005855-0917	00:58:55.88	−09:17:52.1	-0.2	2.0
A399	024458+1257	02:44:58.70	+12:57:32.2	0.0	0.6
(4+5+2=11)	024510+1257	02:45:10.23	+12:57:16.1	-0.8	0.7
	024524+1304	02:45:24.33	+13:04:59.9	2.0	0.9
	024547+1305	02:45:47.61	+13:05:59.2	2.6	0.7
	025725+1257	02:57:25.89	+12:57:48.1	3.2	0.7
	025737+1300	02:57:37.20	+13:00:49.4	12.3	0.7
	025750+1259	02:57:50.83	+12:59:03.0	0.5	0.8
	025802+1309	02:58:02.31	+13:09:33.9	3.0	0.7
	025806+1302	02:58:06.04	+13:02:02.7	1.4	0.7
	031012+1309	03:10:12.88	+13:09:18.3	-0.2	0.8
	031020+1306	03:10:20.51	+13:06:34.5	3.5	0.9
A401	**024548+1333**	02:45:48.17	+13:33:48.4	3.6	0.8
(3+9+3=15)	024608+1330	02:46:08.79	+13:30:20.3	1.4	0.8
	024616+1327	02:46:16.12	+13:27:33.9	3.7	0.8
	025826+1331	02:58:26.58	+13:31:09.7	1.7	0.8
	025829+1333	02:58:29.45	+13:33:28.3	12.5	1.0
	025831+1334	02:58:31.89	+13:34:17.4	35.2	1.0
	025859+1335	02:58:59.00	+13:35:46.8	-4.9	0.9
	025902+1342	02:59:02.98	+13:42:16.3	1.2	1.0
	025907+1343	02:59:07.71	+13:43:27.1	1.0	1.0
	025910+1337	02:59:10.34	+13:37:21.5	-3.8	1.2
	025914+1327	02:59:14.92	+13:27:35.2	8.5	1.0
	025915+1328	02:59:15.51	+13:28:49.9	0.7	1.0
	031109+1329	03:11:09.12	+13:29:07.8	1.0	1.1
	031141+1337	03:11:41.96	+13:37:36.0	-0.6	1.0
	031158+1340	03:11:58.00	+13:40:52.4	-1.3	1.3

Table 2.8 (cont'd)

Cluster (L+M+T=N Sources)	Source	RA (J2000)	Dec (J2000)	Flux (mJy)	Error (mJy)
A478	041306+1026	04:13:06.49	+10:26:37.0	0.4	0.4
(0+6+4=10)	041324+1035	04:13:24.57	+10:35:54.4	-0.1	0.4
	041325+1027	04:13:25.18	+10:27:54.1	-2.7	0.5
	041332+1028	04:13:32.34	+10:28:43.7	-2.3	0.5
	041332+1019	04:13:32.76	+10:19:03.4	-0.9	0.4
	041337+1028	04:13:37.31	+10:28:16.8	0.8	0.4
	042307+1027	04:23:07.41	+10:27:08.6	0.2	0.4
	042316+1037	04:23:16.57	+10:37:12.0	1.9	0.5
	042322+1036	04:23:22.66	+10:36:02.4	3.0	0.5
	042351+1027	04:23:51.78	+10:27:19.1	0.6	0.4
A754	085933-0944	08:59:33.21	−09:44:56.6	0.6	0.6
(4+9+3=16)	085955-0944	08:59:55.01	−09:44:30.6	-0.2	0.7
	090025-0936	09:00:25.04	−09:36:18.9	1.2	0.7
	090033-0941	09:00:33.37	−09:41:19.0	-1.4	0.7
	090835-0942	09:08:35.24	−09:42:19.1	1.4	0.7
	090839-0937	09:08:39.39	−09:37:50.1	-3.7	0.7
	090847-0941	09:08:47.17	−09:41:20.6	-1.9	0.7
	090851-0931	09:08:51.52	−09:31:20.6	-2.8	0.7
	090855-0940	09:08:55.22	−09:40:41.0	1.4	0.7
	090905-0939	09:09:05.51	−09:39:25.9	2.6	0.7
	090907-0941	09:09:07.54	−09:41:01.3	0.2	0.7
	090918-0943	09:09:18.13	−09:43:15.7	5.0	0.7
	090919-0941	09:09:19.27	−09:41:53.9	-0.8	0.7
	091802-0947	09:18:02.77	−09:47:50.7	-0.7	0.7
	091806-0933	09:18:06.15	−09:33:32.6	0.0	0.7
	091825-0938	09:18:25.22	−09:38:53.7	3.0	0.8
A1650	124452-0136	12:44:52.32	−01:36:57.9	0.4	1.6
(3+3+3=9)	124515-0150	12:45:15.85	−01:50:40.1	0.9	1.4
	124526-0136	12:45:26.66	−01:36:58.7	-1.5	1.3
	125820-0140	12:58:20.19	−01:40:30.6	8.3	1.5
	125849-0136	12:58:49.61	−01:36:13.5	-7.3	1.6
	125906-0150	12:59:06.60	−01:50:58.1	56.0	1.7
	131201-0144	13:12:01.92	−01:44:14.0	-1.7	2.1
	131228-0139	13:12:28.75	−01:39:50.7	-10.1	2.3
	131230-0138	13:12:30.27	−01:38:12.8	-3.8	1.5

Table 2.8 (cont'd)

Cluster (L+M+T=N Sources)	Source	RA (J2000)	Dec (J2000)	Flux (mJy)	Error (mJy)
A1651	124749-0412	12:47:49.55	−04:12:02.0	-2.5	1.7
(7+3+3=13)	124805-0414	12:48:05.83	−04:14:01.2	-1.5	1.8
	124811-0413	12:48:11.49	−04:13:39.3	2.1	2.0
	124812-0401	12:48:12.25	−04:01:52.3	-6.8	2.3
	124835-0410	12:48:35.42	−04:10:45.4	17.1	1.6
	124842-0406	12:48:42.54	−04:06:49.6	-7.1	1.6
	124844-0414	12:48:44.83	−04:14:14.1	-1.9	3.4
	125856-0411	12:58:56.48	−04:11:27.0	0.2	2.1
	125922-0411	12:59:22.21	−04:11:44.2	1.9	1.6
	130001-0411	13:00:01.56	−04:11:50.3	4.3	1.9
	131018-0404	13:10:18.03	−04:04:27.1	-0.8	2.7
	131034-0418	13:10:34.75	−04:18:56.7	-4.9	4.5
	131038-0418	13:10:38.55	−04:18:07.5	2.9	3.8
A2029	150010+0535	15:00:10.40	+05:35:50.6	0.7	1.0
(2+9+5=16)	150027+0535	15:00:27.09	+05:35:35.4	-0.4	1.0
	151038+0540	15:10:38.77	+05:40:38.6	0.2	0.8
	151047+0538	15:10:47.21	+05:38:28.5	1.1	0.9
	151053+0545	15:10:53.15	+05:45:12.9	-2.3	0.9
	151055+0536	15:10:55.77	+05:36:56.3	4.2	1.0
	151055+0544	15:10:55.87	+05:44:39.3	-1.6	1.0
	151100+0549	15:11:00.49	+05:49:16.6	2.2	1.4
	151106+0541	15:11:06.13	+05:41:21.2	-1.5	1.1
	151119+0539	15:11:19.82	+05:39:14.7	3.2	1.2
	151124+0540	15:11:24.89	+05:40:52.1	0.3	0.7
	152121+0550	15:21:21.59	+05:50:26.8	2.2	0.8
	152138+0537	15:21:38.30	+05:37:36.5	2.4	0.6
	152143+0540	15:21:43.16	+05:40:30.4	2.8	0.7
	152143+0536	15:21:43.63	+05:36:04.9	-0.4	0.7
	152157+0548	15:21:57.15	+05:48:25.6	1.6	0.8
A2597	230910-1203	23:09:10.72	−12:03:19.2	-1.2	1.1
(6+5+4=15)	230917-1210	23:09:17.08	−12:10:00.4	0.9	1.0
	230928-1213	23:09:28.62	−12:13:04.6	2.0	1.1
	230930-1214	23:09:30.76	−12:14:17.0	1.9	0.9
	231009-1211	23:10:09.34	−12:11:57.3	3.7	1.0
	231014-1212	23:10:14.51	−12:12:33.3	-0.9	0.9
	232438-1207	23:24:38.31	−12:07:44.4	-1.7	0.9
	232519-1207	23:25:19.82	−12:07:28.6	41.5	0.8
	232526-1210	23:25:26.83	−12:10:30.8	-2.1	0.8
	232535-1159	23:25:35.84	−11:59:35.6	3.5	0.9
	232545-1204	23:25:45.02	−12:04:04.4	0.9	0.9
	234032-1202	23:40:32.84	−12:02:06.4	0.9	1.0
	234047-1205	23:40:47.95	−12:05:01.1	-1.2	0.9
	234119-1212	23:41:19.10	−12:12:38.8	-3.5	1.0
	234122-1208	23:41:22.09	−12:08:59.5	-2.0	0.9

·We observed all NVSS sources within $r < 10'$ of LMT pointing centers. Fluxes listed are for 31 GHz. Sources which were detected at the 3-σ level are listed in boldface. The remaining sources were observed but were non-detections.

Chapter 3

SZE Images

Figures 3.1 to 3.15 show images of all the clusters in the CBI primary sample. All the clusters except A1650 and A3827 have density models and temperatures derived from X-ray observations. The left hand figures are dirty images, and point sources have not been subtracted. The middle figures show the clusters after point source subtraction, and the images have been deconvolved using the CLEAN algorithm. The right hand figures show the grayscale from the deconvolved CBI maps with X-ray contours from *ROSAT* PSPC data (Mason & Myers, 2000). A1650 and A3827 do not have *ROSAT* images available.

3.1 A85

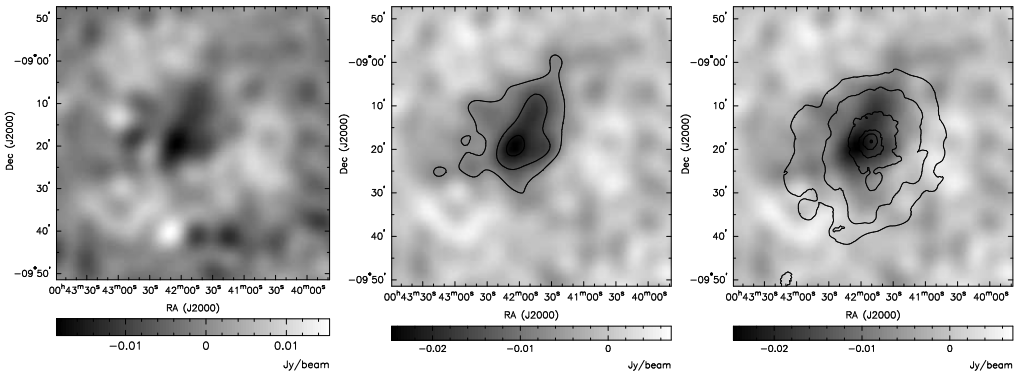

Figure 3.1 The figure on the left is a dirty CBI image of A85 before point source subtraction. The center figure shows the point sources subtracted, and the image has been deconvolved using the CLEAN algorithm and smoothed with a 5′ Gaussian restoring beam. The SZE contour levels in the center plot are -0.0074, -0.015, -0.022 Jy beam^{-1} (30%, 60%, 90% of the peak of -0.0246 Jy beam^{-1}). The figure on the right shows the same grayscale image with *ROSAT* PSPC contours overlaid. The X-ray contour levels in the plot are 0.0005, 0.001, 0.005, 0.02, 0.05, 0.35, 0.5 counts s^{-1} pixel $^{-1}$.

We observed A85 over 11 nights between July and December 2000. X-ray observations show that A85 has a central cooling flow, but this cluster also shows signs of merger activity. There is a smaller group of galaxies just south of the cluster, which can be seen in the X-ray contours. *ASCA* and *BeppoSAX* temperature maps show that this "southern blob" is slightly hotter than the rest of the cluster, indicating that it is likely interacting with the cluster, rather than a foreground projection (Markevitch et al., 1998; Lima Neto et al., 2001). If the subcluster were independent, one would expect it to be cooler than the main cluster given its smaller size. Kempner et al. (2002) study the merger of the subcluster in detail through *Chandra* observations. Lima Neto et al. (2001) determine an overall temperature for the cluster of 6.6±0.3 keV, in agreement with the *ASCA* and De Grandi & Molendi (2002) results.

VLA observations show some extended emission from a very steep spectrum radio source (VSSRS) just southwest of the cluster center at 333 MHz (Bagchi et al., 1998; Lima Neto et al., 2001). Although there is a brighter patch in the CBI map at this location, one would not expect to see emission from the VSSRS at 31 GHz. Bagchi et al. (1998) measure a flux of 3.15±0.15 Jy at 326.5 MHz. If we extrapolate the spectral index of $\alpha = -2.97$ between 300 MHz and 3 GHz, we expect a flux at 31 GHz of 4 μJy, and the bright blob in the CBI is more likely a CMB hot spot. The presence of the VSSRS, however, indicates a possibility of Compton scattering from relativistic nonthermal electrons in this region. See Section 4.4.5.4 for details on how this could affect our H_0 derivation.

We take the *ROSAT* HRI centroid of 00:41:50.94,−9:18:10.7 (J2000) (Prestwich et al., 1995) to be the location of SZE centroid in our fits. Of all the clusters presented here, A85 has the largest number of radio point sources (21) within $10'$ of the cluster center.

3.2 A399/A401

We observed A399 and A401 over 6 nights during October and November 2000. A399 and A401 are a pair of clusters which are close together on the sky and in redshift. X-ray observations indicate that the clusters likely have interacted in the past or are currently interacting (Fujita et al., 1996; Fabian et al., 1997). The scenario favored by Fabian et al. (1997) is that the clusters collided some time

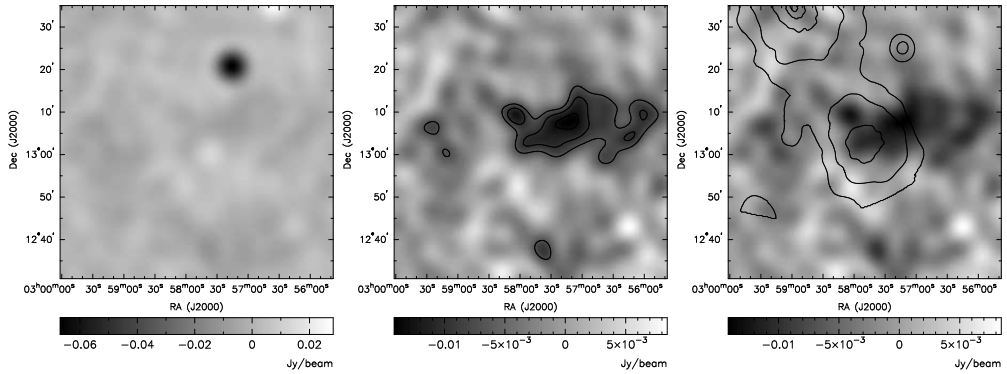

Figure 3.2 A399: Same as in Figure 3.1. The X-ray contours show A399's companion, A401, which does not appear in the SZE map due to attenuation by the CBI primary beam. The SZE contour levels in the center plot are -0.007, -0.010, -0.013 Jy beam^{-1} (50%, 70%, 90% of the peak of -0.0141 Jy beam^{-1}). The X-ray contour levels in the plot are 0.0005, 0.001, 0.005, 0.02, 0.05 counts s^{-1} pixel $^{-1}$.

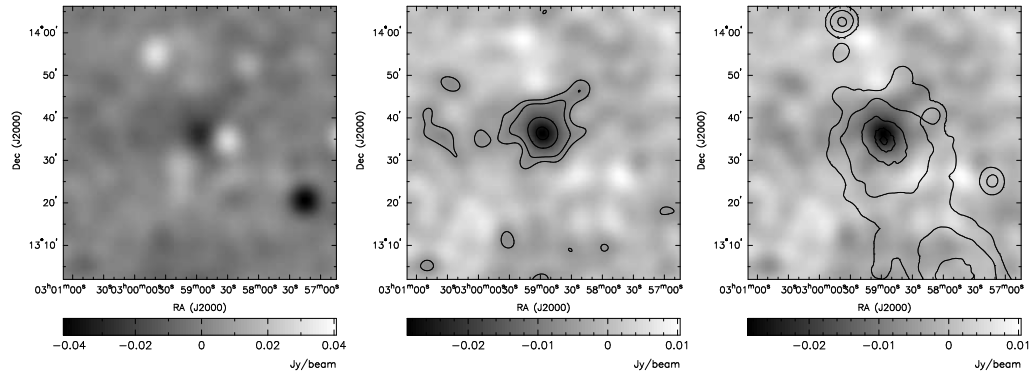

Figure 3.3 A401: Same as in Figure 3.2. The SZE contour levels in the center plot are -0.0055, -0.0086, -0.017, -0.026 Jy beam^{-1} (20%, 30%, 60%, 90% of the peak of -0.0287 Jy beam^{-1}). The X-ray contour levels in the plot are 0.0005, 0.001, 0.005, 0.02, 0.05 counts s^{-1} pixel $^{-1}$.

in the past, disrupting their respective cooling flows, features which are normally associated with clusters containing cD galaxies. The collision could also be responsible for the radio halo associated with A401. The halo has a steep spectrum $\alpha \sim -1.4$ and a total flux density of 21 mJy at 1.4 GHz (Bacchi et al., 2003). Extrapolating the spectral index to 31 GHz, the halo would have a flux of 0.3 mJy at the CBI frequencies and is not expected to be a significant source of contamination. A nonthermal SZE from the halo electrons is possible but difficult to quantify (see Section 4.4.5.4).

The clusters are separated by only about $30'$, which is smaller than the CBI primary beam. The primary beam attenuates the cluster signal so much that the companions do not appear in the respective maps, but we take into account the presence of the A401 when fitting for H_0 from the

A399 data, and vice versa.

The cluster pair has several very bright radio sources in the field of view and appear very "dirty" in the unsubtracted CBI maps. However, those sources can be accurately fitted out. (See Section 4.4.4 for details.) There is a bright spot SW of A399 that appears in the A399 map at 10.1 mJy which does not correspond to any NVSS sources. It is possible this is an inverted spectrum source which falls below the NVSS detection limit at 1.4 GHz. If that is the case, its spectral index would be $\alpha > 0.45$, which is reasonable considering the distribution of spectral indices we discuss in Section 4.4.4. If we assume it is a genuine source and we fit for its flux, our H_0 result changes by $< 6\%$, a small amount compared to the uncertainty from the CMB.

3.3 A478

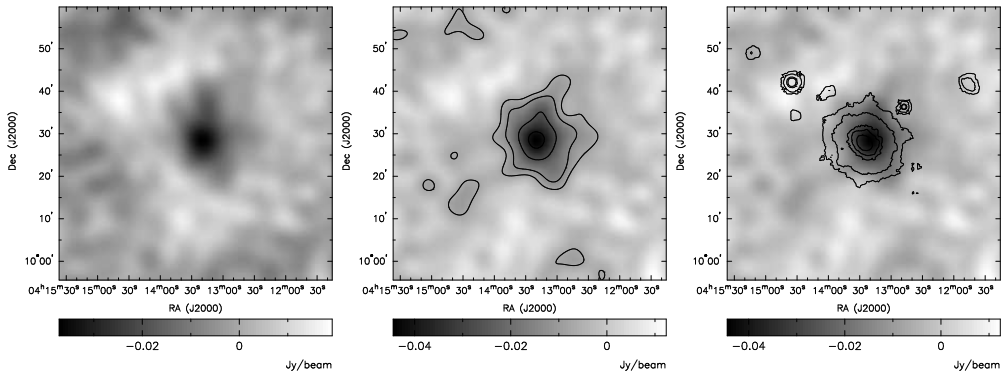

Figure 3.4 A478: Same as in Figure 3.1. The SZE contour levels in the center plot are -0.007, -0.013, -0.0266, -0.04 Jy beam^{-1} (15%, 30%, 60%, 90% of the peak of -0.0444 Jy beam^{-1}). The X-ray contour levels in the plot are 0.0005, 0.001, 0.005, 0.01, 0.03 counts s^{-1} pixel $^{-1}$.

We observed A478 over 11 nights during February, November, and December 2000. A478 is one of the most X-ray luminous clusters in the sample. It has very little point source contamination, and its X-ray profile is extremely regular. A478 is the largest cooling flow cluster within $z < 0.1$ (White et al., 1994), an indication of its relaxed state. From the *ROSAT* HRI observations, White et al. (1994) find the centroid of the X-ray emission to be RA=04:13:25.5, Dec=10:27:58 (J2000). Although we have used slightly different coordinates as our pointing center, in our analysis, we take this position to be the centroid of the SZE emission as well. A478 is one of the cleanest clusters in

our sample in terms of point source contamination. There are very few central sources, and a very small number of sources at large radius whose fluxes need to be fitted.

3.4 A754

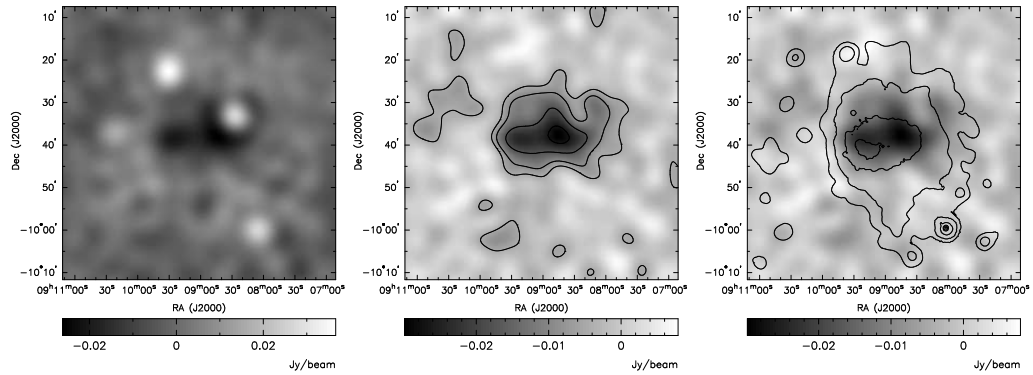

Figure 3.5 A754: Same as in Figure 3.1. The SZE contour levels in the center plot are -0.0045, -0.009, -0.0178, -0.0267 Jy beam^{-1} (15%, 30%, 60%, 90% of the peak of -0.0297 Jy beam^{-1}). The X-ray contour levels in the plot are 0.0005, 0.001, 0.005, 0.02, 0.05, 0.2 counts s^{-1} pixel $^{-1}$.

We observed A754 over 15 nights during February, October, and November 2000. A754 is an irregular cluster which is considered to be a prototypical merging system (e.g., Henry & Briel, 1995; Henriksen & Markevitch, 1996). Although we have included this cluster in our sample to maintain completeness, we recognize that such a disturbed cluster could contribute biases of its own. In the final sample, we therefore present values of H_0 with and without A754.

The cluster is also known to have a strong radio halo. At 74 MHz and 330 MHz, the halo flux is 4 Jy and 750 mJy, respectively (Kassim et al., 2001). Bacchi et al. (2003) find a flux of 86 mJy at 1.4 GHz, and a spectral index of $\alpha = 1.5$ from comparisons to observations at 330 MHz. Assuming this spectral index, we would expect the halo flux at 31 GHz to be 0.8 mJy.

A754 is very heavily contaminated with bright point sources. One source in particular about 15′ NW of the cluster appears in the CBI map to be badly subtracted. This is most likely due to the fact that a spherical β-model is not a good approximation to this elliptical disturbed cluster, leaving a 10 mJy residual in the point source fit. The level of subtraction for this particular source does not change the value of H_0 determined for this cluster.

3.5 A1650

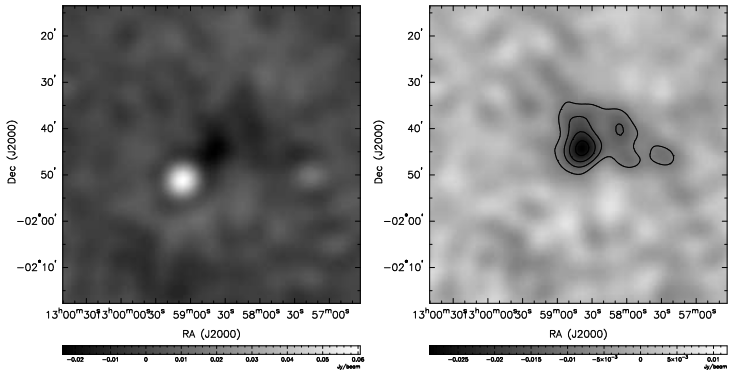

Figure 3.6 A1650: Same as in left and center plots of Figure 3.1. We do not have an X-ray PSPC model or image for this cluster, so we only present the CBI data here. The SZE contour levels in the center plot are -0.009, -0.0145, -0.020, -0.026 Jy beam^{-1} (30%, 50%, 70%, 90% of the peak of -0.0289 Jy beam^{-1}).

On the long baselines, A1650 has a bright central negative source that lines up with a faint point source from NVSS in the trail field ($\sim$ 10 mJy in the LMT subtracted image, so the actual source flux would be $\sim$ 20 mJy). This source is not detected by the 40-m, and it is unlikely that we would have missed a 20 mJy ($\sim 10 - \sigma$) source. Therefore, we conclude that the cluster is fairly compact and still shows strong signal on the long baselines. Since we do not have an X-ray model for this cluster, we cannot verify this currently. When modelfitting for the cluster after point source subtraction (leaving in the bright central negative source), it is best fit by a 2-component model - one large angular component and one smaller one. A possible explanation is that the compact cluster is sitting on a large cold-spot in the CMB.

3.6 A1651

We observed A1651 over 8 nights during February 2000 and April and May 2001. A1651 appears to be a dynamically relaxed cD cluster with a regular *ROSAT* PSPC profile (Gonzalez et al., 2000; Markevitch et al., 1998, e.g). However, in their analysis of *ASCA* observations, Markevitch et al. (1998) find that a cooling component is not required in the fit. This cluster appears to be unremarkable, although it has a large number of bright point sources which need to be subtracted from

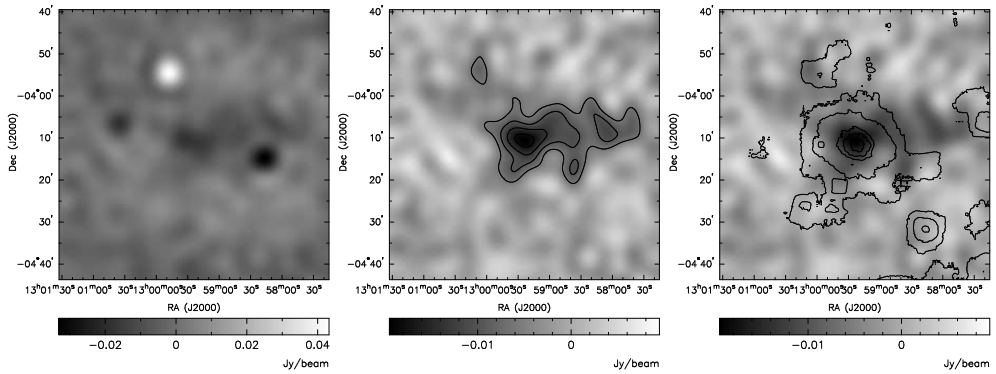

Figure 3.7 A1651: Same as in Figure 3.1. The SZE contour levels in the center plot are -0.006, -0.0097, -0.0136, -0.0175 Jy beam^{-1} (30%, 50%, 70%, 90% of the peak of -0.0194 Jy beam^{-1}). The X-ray contour levels in the plot are 0.0005, 0.001, 0.005, 0.01, 0.03 counts s^{-1} pixel $^{-1}$.

the CBI data.

3.7 A2029

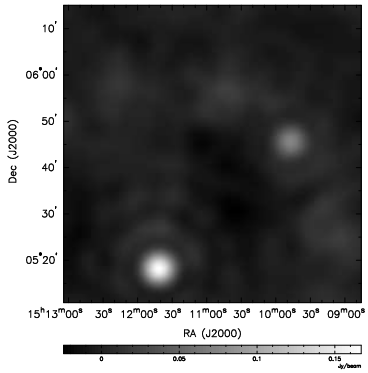

Figure 3.8 A2029: Dirty image of A2029. The southeastern foreground object is not a point source and could not be removed with existing software.

A2029 has foreground source which is not a point source, so cleaning it is more tricky. I haven't had time to incorporate subtraction of extended sources yet, so for now, we simply present the unsubtracted map.

3.8 A2597

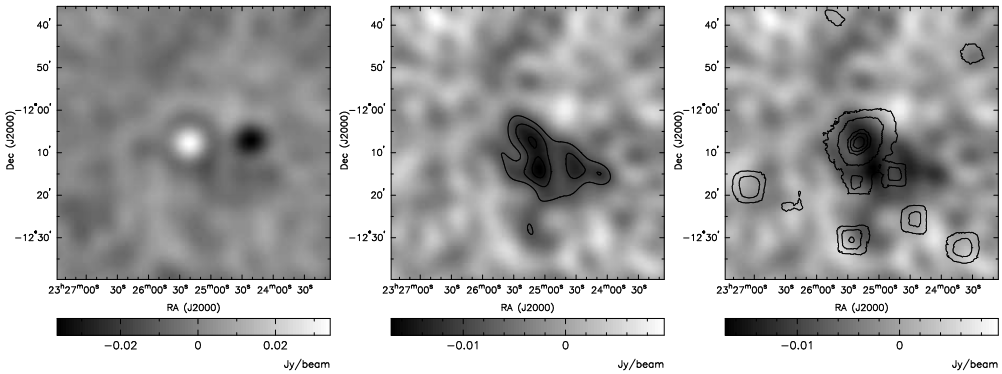

Figure 3.9 A2597: Same as in Figure 3.1. The SZE contour levels in the center plot are -0.0085 -0.0119 -0.0153 Jy beam^{-1} (50%, 70%, 90% of the peak of -0.017 Jy beam^{-1}). The X-ray contour levels in the plot are 0.0005, 0.001, 0.005, 0.01, 0.03 counts s^{-1} pixel $^{-1}$.

We observed A2597 over 5 nights during September, October, and November 2000. A2597 is another regular cD cluster with a cooling flow. Its X-ray luminosity is among the weakest in our sample, and the SZE maps indicate this. Our detection is marginal at best, and the error in deriving H_0 from this cluster is large. Sarazin & McNamara (1997) take the centroid of the cluster to be the position of the central cD galaxy (23:25:19.64,−12:07:27.4, J2000), which we also use as the centroid in the SZE fits. The cD galaxy is a strong emitter at 31 GHz. We determine a flux for the central source of 40 mJy, both from the OVRO 40-m and the CBI long baselines (> 3 m), giving us confidence in our measurement.

3.9 A3112

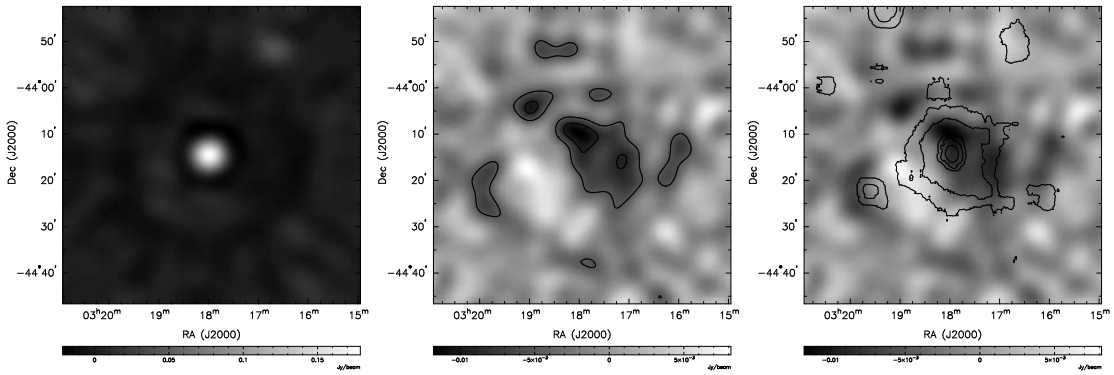

Figure 3.10 A3112: Same as in Figure 3.1. The SZE contour levels in the center plot are -0.005, -0.009, -0.012 Jy beam^{-1} (40%, 65%, 90% of the peak of -0.0136 Jy beam^{-1}). The X-ray contour levels in the plot are 0.0005, 0.001, 0.005, 0.01, 0.03 counts s^{-1} pixel $^{-1}$.

A3112 has a very bright point source from the central galaxy with a flux ∼200 mJy. Because A3112 is a southern cluster, we have not been able to obtain independent measurements of the point source flux. We can fit for the flux of the central source using the CBI long baselines, but this may not be reliable. In any case, A3112 is one of the less luminous clusters in the sample and probably would not contribute significantly to the sample average.

3.10 A3266

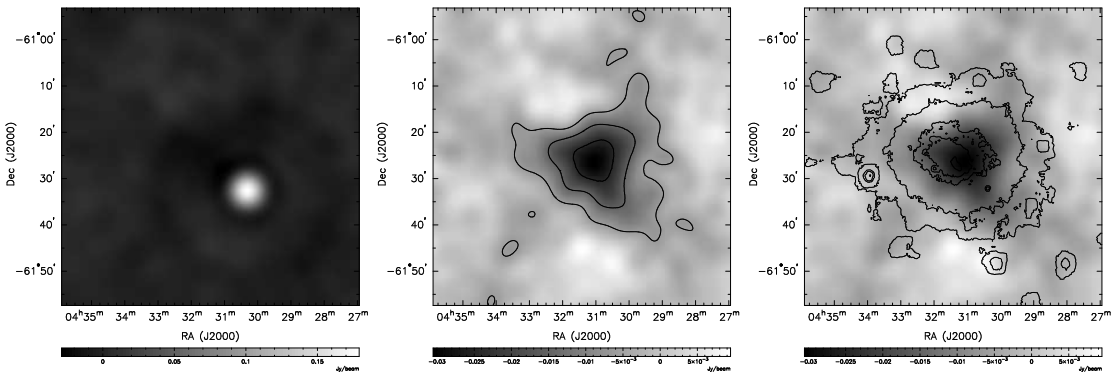

Figure 3.11 A3266: Same as in Figure 3.1. The SZE contour levels in the center plot are -0.006, -0.015, -0.0244 Jy beam^{-1} (20%, 50%, 80% of the peak of -0.0305 Jy beam^{-1}). The X-ray contour levels in the plot are 0.0005, 0.001, 0.005, 0.01, 0.03 counts s^{-1} pixel $^{-1}$.

A3266 is also a southern cluster that was too far south to be observed by the VLA or the OVRO 40-m, so we do not have data on point source locations or fluxes.

3.11 A3558

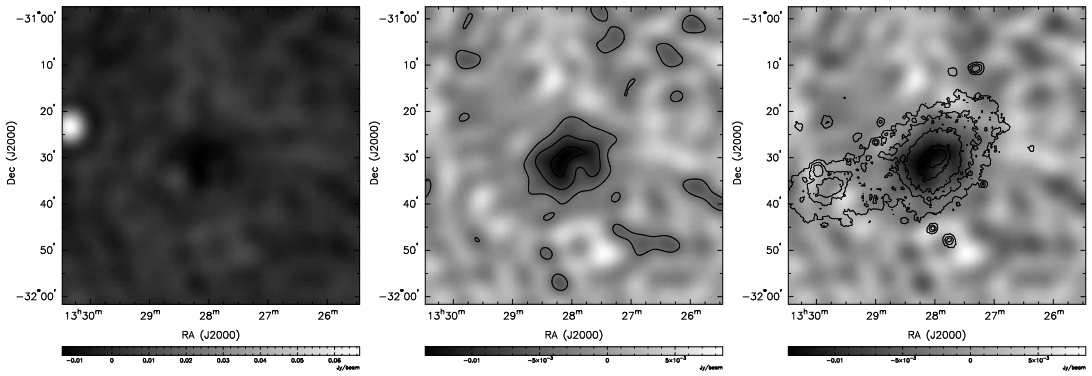

Figure 3.12 A3558: Same as in Figure 3.1. The SZE contour levels in the center plot are -0.004, -0.008, -0.012 Jy beam^{-1} (30%, 60%, 90% of the peak of -0.0134 Jy beam^{-1}). The X-ray contour levels in the plot are 0.0015, 0.003, 0.006, 0.015, 0.03 counts s^{-1} pixel $^{-1}$.

A3558 is at intermediate declination, so we do have NVSS data for this cluster, but not 40-m observations of central sources.

3.12 A3571

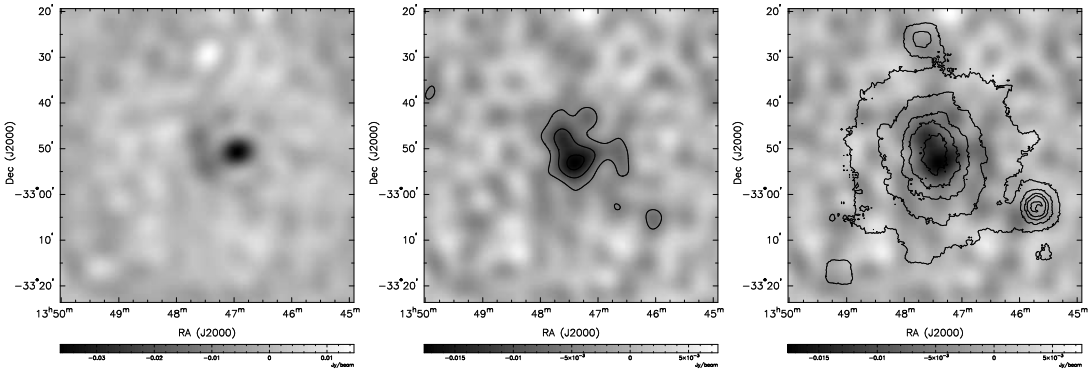

Figure 3.13 A3571: Same as in Figure 3.1. The SZE contour levels in the center plot are -0.005, -0.011, -0.016 Jy beam^{-1} (30%, 60%, 90% of the peak of -0.0175 Jy beam^{-1}). The X-ray contour levels in the plot are 0.0008, 0.002, 0.005, 0.01, 0.03 counts s^{-1} pixel $^{-1}$.

Like A3558, A3571 is at intermediate declination, so we do have NVSS data for this cluster, but not 40-m observations of central sources.

3.13 A3667

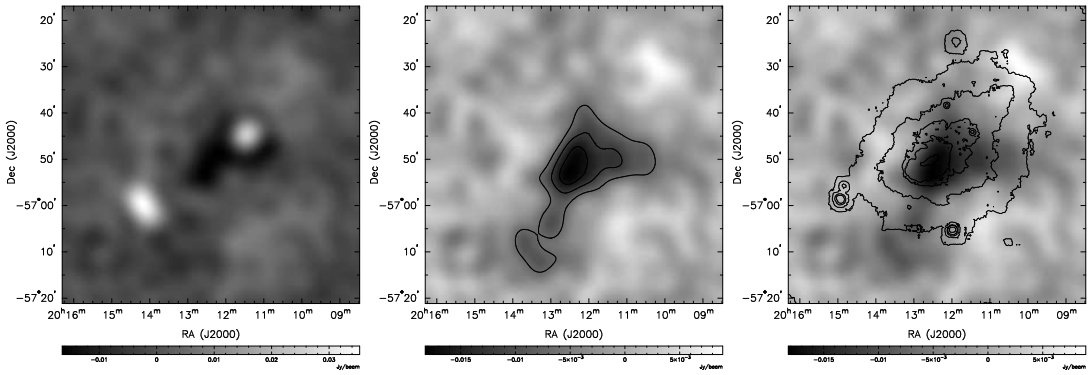

Figure 3.14 A3667: Same as in Figure 3.1. The SZE contour levels in the center plot are -0.007, -0.012, -0.016 Jy beam^{-1} (40%, 65%, 90% of the peak of -0.0182 Jy beam^{-1}). The X-ray contour levels in the plot are 0.0008, 0.002, 0.005, 0.01, 0.03 counts s^{-1} pixel $^{-1}$.

This is a southern source without NVSS or 40-m observations.

3.14 A3827

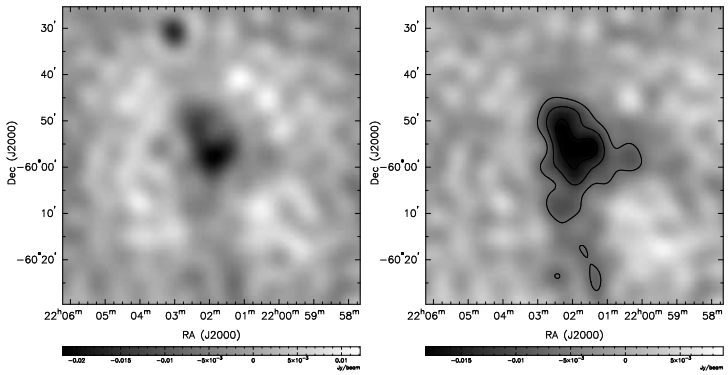

Figure 3.15 A3827: Same as in Figure 3.1. The SZE contour levels in the center plot are -0.007, -0.012, -0.017 Jy beam^{-1} (35%, 60%, 85% of the peak of -0.0197 Jy beam^{-1}). No Xray contours.

This is a southern source without NVSS or 40-m observations. We also do not currently have X-ray observations for this cluster.

Chapter 4

H_0 Analysis

In the previous chapter we described how we acquired the SZE data, and we briefly explained how foreground point sources were removed through observations with the OVRO 40-m telescope. In this chapter, we discuss how we determine H_0 from the SZE data. We needed density and temperature models for the gas from X-ray observations, and we used published data from *ROSAT* , *ASCA* , and *BeppoSAX* (Mason & Myers, 2000; Markevitch et al., 1998; White, 2000; De Grandi & Molendi, 2002). We explain how we used the models to calculate the expected SZE visibility profiles, which we fitted to the observed CBI data to measure the best-fit value of H_0 for each cluster. We also describe our point source subtraction method in more detail. Finally, we detail the simulations performed to determine the magnitude of errors expected from various sources including the CMB primary anisotropies, modelling uncertainties, and point source subtraction.

4.1 Deriving Density Models from X-ray Imaging Observations

We combine density profile results from *ROSAT* (Mason & Myers, 2000) with temperature measurements from *ASCA* (Markevitch et al., 1998; White, 2000) and *BeppoSAX* (De Grandi & Molendi, 2002). The *ROSAT* PSPC has a spatial resolution of $30''$ FWHM and a field of view of 1.5 degrees in diameter, which makes it well suited for observations of the low-redshift clusters in our sample. At a redshift of 0.05, the field of view corresponds to 3.7 h^{-1} Mpc, which is significantly larger than

the expected virial radius for the clusters. Due to its small energy range (0.1–2.4 keV) and spectral resolution, it is not possible to obtain sufficiently accurate temperatures from *ROSAT* data. *XMM-Newton* and *Chandra* are ideal for determining both accurate density and temperature profiles, and we will combine those spectral imaging data with our SZE observations in a future paper. Here, we use published data from *ASCA* and *BeppoSAX* observatories, which both have energy ranges from 1–10 keV, making them useful for determining temperatures of the hot gas in galaxy clusters. Mason & Myers (2000, hereafter MM2000) derived density profiles for 14 of the clusters in our sample using archival *ROSAT* PSPC data, and we use their models in our H_0 analysis.

As described in Section 1.3, it is common to assume that the cluster gas is well fitted by a spherical isothermal β-model (Cavaliere & Fusco-Femiano, 1978), with the gas distribution given by Equation 1.11. Combining this with Equation 1.10 yields the β-model X-ray surface brightness profile

$$I(\theta) = I_0 \left(1 + \frac{\theta^2}{\theta_0^2}\right)^{-3\beta+1/2}, \tag{4.1}$$

from which the parameters β and θ_0 can be derived by fitting to the X-ray imaging observations.

The β-model density normalization, n_{e0}, can be calculated from the total X-ray flux measured over the observed bandpass. We summarize here the analysis method used by MM2000. First, the bremsstrahlung emission is modelled as a Raymond-Smith (Raymond & Smith, 1977) plasma that is photo-electrically absorbed by intervening neutral hydrogen along the line of sight to the cluster. The X-ray spectrum modelling software, XSPEC (Arnaud, 1996) reports the normalization of the spectrum through the parameter K, defined in cgs units as

$$K = \frac{10^{-14}}{4\pi D_L^2} \int n_e n_p dV, \tag{4.2}$$

where n_e is the electron density, n_p is the proton density, the luminosity distance, $D_L = D_A(1+z)^2$, and the integral is over all space. The emission measure is defined as

$$EM = \int n_e n_p dV. \tag{4.3}$$

For a β-model, the emission measure in an annular region between θ_1 and θ_2 is

$$EM(\theta_1,\theta_2) = \frac{n_p}{n_e} n_{e0}^2 D_A^3 \theta_0^3 \sqrt{\pi} \frac{\Gamma(3\beta-1/2)}{\Gamma(3\beta)} \times \frac{2\pi}{3(2\beta-1)} [C(\theta_1) - C(\theta_2)], \tag{4.4}$$

where

$$C(\theta) = \left[1 + \left(\frac{\theta}{\theta_0}\right)^2\right]^{-3\beta+3/2}. \tag{4.5}$$

For a plasma with the cosmic helium mass fraction $Y = 0.24$ and metal abundances of 30% solar, $n_p/n_e = 0.862$; this is the value we adopt. The central density is then

$$n_{e0} = 4.151\times10^{-3}\mathrm{cm}^{-3} h^{1/2} \times \left[\frac{n_e/n_p}{1.16}\left(\beta-\frac{1}{2}\right)\frac{\mathrm{arcmin}^3}{\theta_0^3}\frac{(1+z)^6}{1+z-\sqrt{1+z}} \times \frac{\Gamma(3\beta)}{\Gamma(3\beta-1/2)}\frac{K/10^{-2}}{C(\theta_1)-C(\theta_2)}\right]^{1/2}. \tag{4.6}$$

Note that this expression from MM2000 assumes $q_0 = \frac{1}{2}$ in substituting for D_A; for a more general cosmology,

$$n_{e0} = 3.215\times10^{-1}\mathrm{cm}^{-3} h^{1/2} \times \left[\frac{n_e/n_p}{1.16}\left(\beta-\frac{1}{2}\right)\frac{\mathrm{arcmin}^3}{\theta_0^3}(1+z)^4\frac{\mathrm{Mpc}}{D_A} \times \frac{\Gamma(3\beta)}{\Gamma(3\beta-1/2)}\frac{K/10^{-2}}{C(\theta_1)-C(\theta_2)}\right]^{1/2}. \tag{4.7}$$

Table 4.1 lists the best fit model parameters from MM2000 which we use in our SZE analysis. To account for the differences due to our assumed cosmologies and slight differences in the redshifts and electron temperatures assumed in some cases, we have recalculated the n_{e0} normalization values using Equation 4.7. We used redshifts from the compilation of Struble & Rood (1999).

4.2 Cluster Temperatures

Cluster temperatures T_e can be determined through spectral modeling, where high-resolution X-ray spectra are fitted with a thermal emission model for a low-density plasma in collisional ionization equilibrium (i.e., the *mekal* or Raymond-Smith models in XSPEC), which has been absorbed by Galactic hydrogen. If an X-ray detector has sufficient spatial resolution, such as *XMM-Newton* or *Chandra* , temperature profiles can be measured by binning the spectral data into different regions

Table 4.1 Cluster redshifts and parameters derived from X-ray observations. The redshifts are from the compilation of Struble & Rood (1999). The other parameters are taken from Mason & Myers (2000), but the densities have been recalculated to account for slightly different temperatures, redshifts, and cosmology assumed in this paper. (See text for details.)

Cluster	θ_0 (arcm)	β	n_{e0} ($10^{-3}h^{1/2}$ cm^{-3})
A85	2.04±0.52	0.600±0.05	10.20±3.40
A399	4.33±0.45	0.742±0.042	3.22±0.46
A401	2.26±0.41	0.636±0.047	7.95±0.98
A478	1.00±0.15	0.638±0.014	27.88±6.39
A754	5.50±1.10	0.713±0.120	3.79±0.07
A1651	2.16±0.36	0.712±0.036	6.84±1.79
A2597	0.49±0.03	0.626±0.018	42.99±3.82

across the detector. Here, we rely on published *ASCA* and *BeppoSAX* results. *ASCA* has an energy dependent PSF which makes it difficult to obtain accurate temperature profiles from the data. Single emission weighted temperatures over the entire cluster derived from *ASCA* should be reliable, and we use these as estimates for "isothermal" temperatures in our SZE analysis. *BeppoSAX* has good spatial resolution ($1'$) and a better understood PSF, making it a better candidate for determining temperature profiles. *BeppoSAX* results are available for 2 clusters whose results are reported here. De Grandi & Molendi (2002) report average temperatures for the clusters, excluding cooling flow regions. Where available, we combine these with the *ASCA* results, and in Section 4.4.3 we use their mean profile results to determine the magnitude of error we might expect from our isothermal assumption.

Table 4.2 lists temperature results obtained from *ASCA* data by Markevitch et al. (1998) and White (2000). The results are in fair agreement, except for the cooling flow clusters, where assumptions used in the energy-dependent PSF matter more. Until we can conclusively resolve these discrepancies using observations from current missions, we adopt the average of the results from both these papers. Given that the results are based on the same observational data, the errors are likely to be correlated. As a conservative estimate of the error in the mean of the temperatures, we use the larger of the two sets of error bars, and we include an extra component to the uncertainty to account for systematic offsets between the two measurements. Note that Markevitch et al. (1998) quote 90% confidence errors, while White (2000) uses 68% confidence intervals. For consistency, we

Table 4.2 Cluster temperatures from *ASCA* and *BeppoSAX* . All errors are 68% confidence

Cluster	*ASCA* White (keV)	*ASCA* MFSV (keV)	*ASCA* Avg (keV)	*BeppoSAX* DM2002 (keV)	*BeppoSAX* & *ASCA* average	error in $h^{-1/2}$	Cooling Flow or Single Component
A85	6.74±0.50	6.9±0.2	6.8±0.5	6.83±0.15	6.8±0.2	±2.9%	CF
A399	6.80±0.17	7.0±0.2	6.9±0.2			±2.9%	SC
A401	8.68±0.17	8.0±0.2	8.3±0.4			±4.8%	SC
A478	$7.42^{+0.71}_{-0.54}$	$8.4^{+0.5}_{-0.8}$	7.9±0.8			±10.1%	CF
A754	9.83±0.27	$9.5^{+0.4}_{-0.2}$	9.7±0.3	$9.42^{+0.16}_{-0.17}$	9.5±0.2	±2.1%	SC
A1651	$6.21^{+0.18}_{-0.17}$	6.1±0.2	6.2±0.2			±6.3%	SC
A2597	$3.91^{+0.27}_{-0.22}$	$4.4^{+0.2}_{-0.4}$	4.2±0.4			±9.5%	CF
A2029	8.22±0.21	9.1±0.6	8.7±0.7	7.77±0.28	7.9±0.6	±7.6%	CF
A3112	4.69±0.27	4.4±0.6	4.5±0.6			±13.3%	CF
A3266	8.34±0.17	8.0±0.3	8.2±0.3	8.97±0.30	8.6±0.4	±4.7%	SC
A3558	6.60±0.50	5.5±0.2	6.1±0.7			±11.5%	CF
A3571	8.12±0.42	6.9±0.1	7.5±0.7	7.23±0.17	7.2±0.2	±2.8%	CF
A3667	8.11±0.82	7.0±0.4	7.6±1.0			±13.2%	CF

convert Markevitch et al. (1998) errors to 68% confidence. Since we do not have knowledge of the actual likelihood distribution, we assume a Gaussian distribution, symmetrize the errors, and scale them by 1.65. Two of the clusters here have *BeppoSAX* observations which have been analyzed in detail (De Grandi & Molendi, 2002). These results are independent of the *ASCA* temperatures, and Table 4.2 shows them to be in excellent agreement. Where available, we average the *BeppoSAX* temperatures with the mean *ASCA* temperatures. The temperatures and errors we assume are listed in Table 4.2.

4.3 Modeling the Expected SZE Profile

With the density and temperature parameters, we can calculate the expected SZE image profile,

$$\frac{\Delta I_{\rm SZE}}{I}(\theta) = \frac{k_b T_e}{m_e c^2}\sigma_T f(x,T_e) n_{e0}\sqrt{\pi}\frac{\Gamma(\frac{3\beta}{2}-\frac{1}{2})}{\Gamma(\frac{3\beta}{2})} D_A \theta_0 \left(1+\frac{\theta^2}{\theta_0^2}\right)^{-\frac{3}{2}\beta+\frac{1}{2}}, \tag{4.8}$$

obtained by substituting Equation 1.11 into Equation 1.9, where $f(x,T_e)$ is $\frac{xe^x}{e^x-1}$ multiplied by the expression in brackets (divided by $\frac{k_b T_e}{m_e c^2}$) from Equation 1.9. We then FFT the CBI image to the visibility domain using numerical recipes (Press et al., 1996). No software existed to analyze the CBI

SZE data, so I wrote a C program called SZBETA, using the DIFMAP (Shepherd, 1997) interface to perform all the simulations and modelling. The program is described in detail in Appendix A. As we discuss later, the CMB contamination is sufficiently large that we cannot accurately determine the β-model parameters from the CBI data. The parameters are, however, very well constrained by the *ROSAT* imaging observations, and we hold the model parameters fixed. For each CBI frequency channel, Equation 4.8 can then be reduced to

$$\Delta I_{\rm SZE}(\theta) = I_0 \left(1 + \frac{\theta^2}{\theta_0^2}\right)^{-\frac{3}{2}\beta+\frac{1}{2}}, \tag{4.9}$$

where $I_0 (\propto h^{-1/2})$ is a constant.

An interferometer measures the Fourier transform of this profile multiplied by the primary beam of the telescope:

$$V(u,v) = I_0 \int_{-\infty}^{\infty}\int_{-\infty}^{\infty} B(\theta) \left(1 + \frac{\theta^2}{\theta_0^2}\right)^{-\frac{3}{2}\beta+\frac{1}{2}} e^{2\pi i(ux+vy)}\, dx\, dy, \tag{4.10}$$

where x and y are positions on the sky ($\theta^2 = x^2 + y^2$), and u and v are the baseline projections in units of wavelength. Details of the CBI primary beam, B, are presented in Pearson et al. (2003). We fit the visibility model in Equation 4.10 to the observed CBI data by minimizing χ^2 with respect to I_0 to obtain the best-fit SZE decrement and $h^{-1/2}$. The best-fit visibility profiles are plotted with the radially averaged, point source subtracted CBI data in Figure 4.1. Table 4.3 lists results from the fits to the CBI observations in mJy arcm^{-2} and gives the χ^2 values for the fits.

In the context of interferometer observations, it is convenient to use intensity units of Jy sr^{-1}, but more traditional single dish observations quote SZE decrements in μK. We use

$$\Delta I_{\rm SZE} = \frac{2\nu^2 k T_{CMB}}{c^2} \frac{x^2 e^x}{(e^x-1)^2} \frac{\Delta T}{T_{CMB}} \tag{4.11}$$

to convert from intensity to μK. Table 4.6 lists results from the fits to the CBI observations in μK, and gives the χ^2 values for the fits. Another useful quantity is the Compton-y parameter, defined

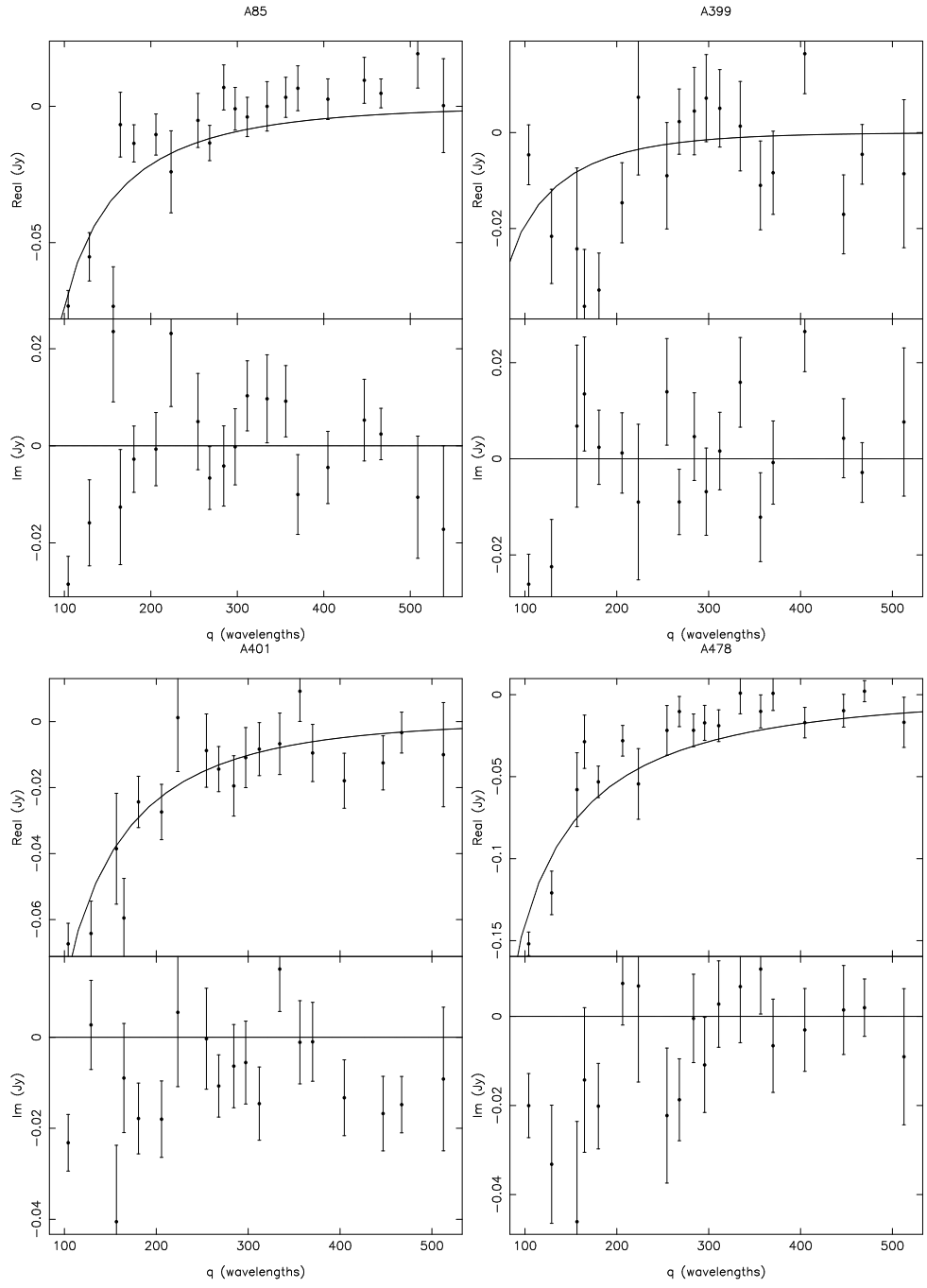

Figure 4.1 Real and imaginary visibilities showing radially averaged CBI data with best fit model profiles. The radial length of the visibility in wavelengths is given by $q = \sqrt{u^2 + v^2}$. At 30 GHz, 100 wavelengths = 1 m.

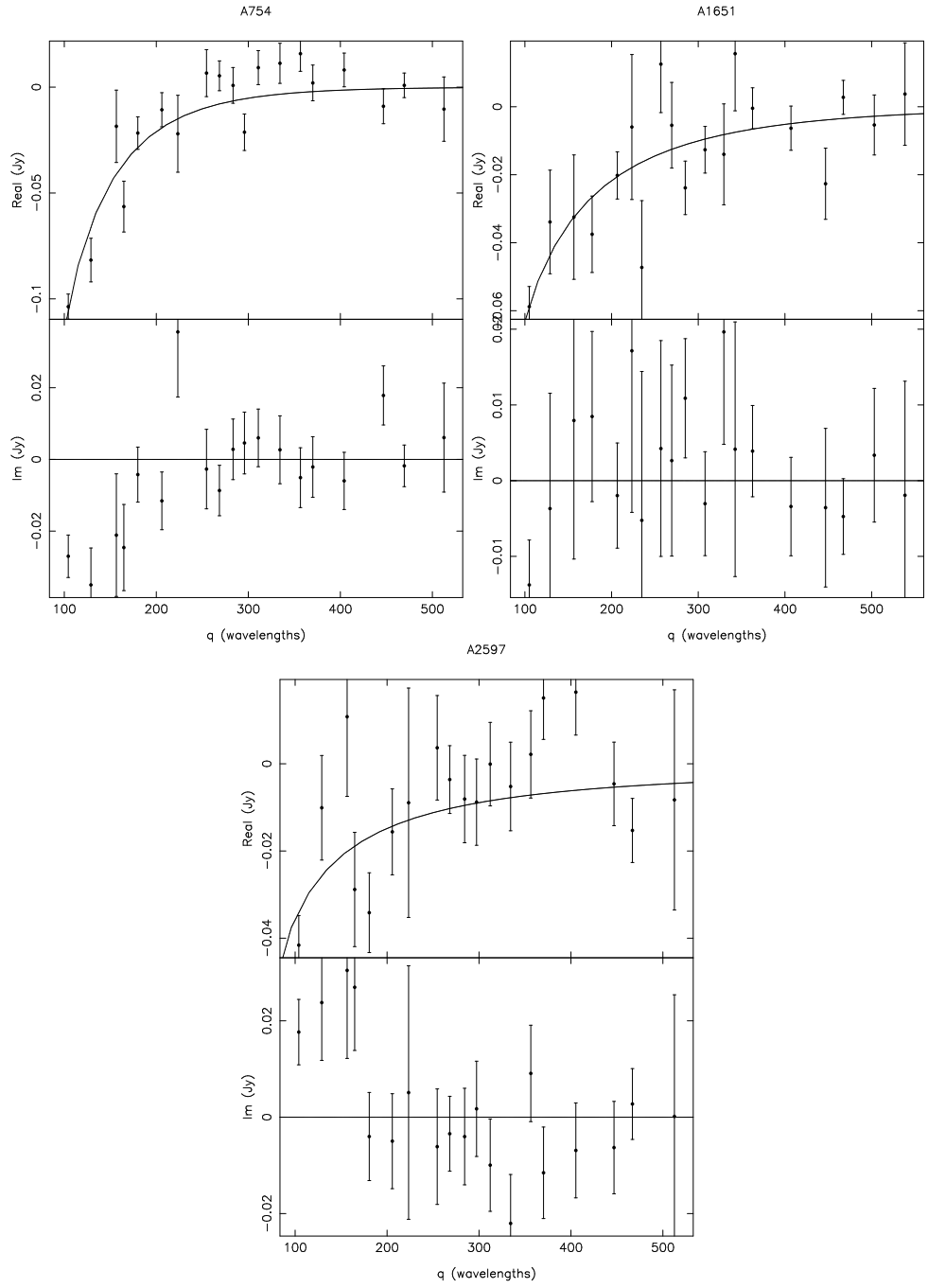

Figure 4.2 As in Figure 4.1, for A754, A1651, and A2597

Table 4.3. Fit results

Cluster	Best fit ΔI_0 (mJy/arcm^2)	Predicted ΔI_0 (mJy/arcm^2)	Best fit $h^{-1/2}$	Reduced χ^2	degrees of freedom
A85	-1.43	-1.16	1.24	1.05	12814
A399	-0.17	-0.76	0.23	1.04	19659
A401	-1.48	-1.46	1.01	1.03	19653
A478	-4.39	-2.49	1.76	1.06	20658
A754	-1.38	-1.25	1.11	1.06	15950
A1651	-1.27	-0.89	1.43	1.14	19628
A2597	-1.81	-1.05	1.72	1.07	13856

The values in this table are the raw numbers obtained from the fits to the CBI visibility data and do not include corrections from X-ray model bias or unsubtracted point sources.

as

$$y = \frac{k_b T_e}{m_e c^2} \tau, \tag{4.12}$$

which is independent of the frequency of observation. We list y_0, the central Compton-y value for each cluster in Table 4.6.

4.4 Error Analysis

The analysis method described above makes several idealizing assumptions about galaxy clusters - that they are spherical, smooth, and isothermal. In this section we discuss possible implications of deviations from these assumptions. So far, we also have not considered effects of contaminating factors such as observational noise, CMB primary anisotropies, foreground point sources, nonthermal radio emission from relics or haloes, and kinematic SZE signals from peculiar velocities. We address all these different sources of error in this section. Since the SZE model-fitting is performed in the visibility domain (the Fourier transform of the image plane), the error sources have relationships which are not analytical and whose interpretations are not always intuitive. Therefore, to characterize their effects, we use Monte Carlo simulations, mimicking the real observations and various error sources.

In the simulations, we attempted to reproduce as accurately as possible all the components that

enter a real CBI observation. We derived an SZE model "image" using the cluster gas parameters obtained from the X-ray data as described in Section 4.3. We multiplied the image by the CBI primary beam, and performed a Fourier transform to obtain our simulated model visibility profile. We used the observed CBI visibility data as a template, maintaining identical $u - v$ coverage to the real observation by replacing the observed visibility data with the simulated data and adding Gaussian noise with the variance observed in the data. We then analyzed each mock data set in the same way as the actual observation, fitting for the "observed" SZE decrement. We repeated this process 10^3 times for each cluster, randomizing the thermal noise and the error source whose impact we were attempting to quantify. This yielded a distribution of best-fit I_0's, which is equivalent to the distribution of $h^{-1/2}$ for that error source, which we use to obtain 68% confidence intervals. As we discuss below, several sources of error are not independent, and must be considered together in the Monte Carlo simulations. The largest source of random error is the intrinsic CMB anisotropy. It has a significant impact on almost all the other error sources, so we include it in most of the other simulations.

4.4.1 Intrinsic CMB Anisotropies

The CBI has measured the CMB on arcminute scales, finding bandpower levels of $2067 \pm 375\ \mu\mathrm{K}^2$ at $\ell \sim 600$ (1 m baseline), and $1256 \pm 284\ \mu\mathrm{K}^2$ at $\ell \sim 1200$ (2 m baseline) (Pearson et al., 2003). Figure 4.1 shows that the SZE cluster signal is strongest on the 1 m and 2 m baselines, where the CMB is a significant contaminant. The SZE data is effectively radially averaged in the visibility fitting, and the rms of the CMB averaged in this way on the 1 m and 2 m baselines is 30 mJy and 7 mJy, respectively. We cannot remove the intrinsic CMB anisotropies from our data without observations at other frequencies, so we need to estimate its impact on our results.

We generated 10^3 randomized simulated images of the CMB from an input power spectrum using the method described below:

1. Specify N_1 and N_2, the number of pixels in the image; δx and δy, the size of each pixel; $C_l, l = 2, \ldots, l_{\max}$, a tabulated angular power spectrum; and a random number seed.

2. Compute the cell size in the (u, v) plane, $\delta u = 1/N_1\delta x$, $\delta v = 1/N_2\delta y$.

3. Create a complex array of size $N_1 \times N_2$, with indices $-N_1/2 \leq k_1 \leq N_1/2 - 1$, $-N_2/2 \leq k_2 \leq N_2/2 - 1$.

4. For each element in this array, compute $l = 2\pi\sqrt{(k_1\delta u)^2 + (k_2\delta v)^2} - \frac{1}{2}$, find the corresponding C_l in the tabulated power spectrum, and compute $\sigma = \sqrt{\overline{C_l}\delta u\delta v}$ where $\overline{C_l}$ is the sum of 1/12 of each corner value and 8/12 of the central value (an approximation of the integration of C_l over the cell; cf. Simpson's rule). The l's for the cell corners are given by

$$2\pi\sqrt{([(k_1 \pm \tfrac{1}{2})\delta u]^2 + [(k_2 \pm \tfrac{1}{2})\delta v]^2} - \tfrac{1}{2}. \tag{4.13}$$

5. Assign to both the real and imaginary parts of each element numbers taken from a gaussian distribution $N(0, \sigma/\sqrt{2})$. To take into account conjugate symmetry, one half of the array must be copied from the other half, and the central $(0, 0)$ element must be real; for simplicity, we set this element (corresponding to C_0) to zero so the sum of the sky image pixels is zero.

6. Perform the FFT to obtain a real (not complex) sky image of size $N_1 \times N_2$.

7. Scale the image by $T_0 = 2.725$ K to get an image of ΔT.

Each of these "sky" realizations was then added to the simulated clusters described above, and we fitted for the value of $h^{-1/2}$ which minimized χ^2. The input power spectrum we used is the best fit model to the CBI power spectrum observations, combined with Boomerang-98, DASI, Maxima, VSA, and *COBE* DMR measurements (Sievers et al., 2003):$\Omega_{\rm tot} = 1.0$, $\Omega_b h^2 = 0.02$, $\Omega_{\rm cdm} h^2 = 0.14$, $\Omega_\Lambda = 0.5$, $n_s = 0.925$, $\tau_c = 0$, $\mathcal{C}_{10} = 887\ \mu\mathrm{K}^2$. We list in Table 4.4 the 68% confidence intervals in $h^{-1/2}$ for each cluster, given the expected levels of CMB contamination based on the CBI's power spectrum measurements. These clearly dominate all other sources of error.

Table 4.4. Errors

Cluster	CMB error	X-ray mod bias	pt src bias	T_e error	$V_{\rm pec}$ error	CMB+Ther+ptso error
A85	$\pm$0.36	1.01	+0.00	0.03	0.05	$\pm$0.38
A399	$\pm$0.42	1.01	+0.02	0.03	0.05	$\pm$0.42
A401	$\pm$0.27	1.01	+0.03	0.05	0.04	$\pm$0.27
A478	$\pm$0.25	1.00	+0.00	0.10	0.04	$\pm$0.25
A754	$\pm$0.26	1.04	+0.02	0.02	0.04	$\pm$0.29
A1651	$\pm$0.43	1.00	+0.00	0.06	0.06	$\pm$0.44
A2597	$\pm$1.06	1.00	+0.01	0.09	0.08	$\pm$1.07

·The X-ray model bias is described in Section 4.4.2. One divides the raw $h^{-1/2}$ by this number to correct for the bias. The unsubtracted point source bias is described in the text. One adds the raw $h^{-1/2}$ to this number to correct for it. The T_e and $V_{\rm pec}$ errors are fractional; multiply $h^{-1/2}$ by these to get the error. The CMB and the CMB+Thermal noise+subtracted point source error listed is the additive error in $h^{-1/2}$.

4.4.2 Density Model Errors

Because the CMB contamination is so large, it is not meaningful to fit for the shape of the cluster gas profile from the SZE data. We therefore assume that the profile we derived from the X-ray data is correct, and hold the β-model parameters fixed. Here, we quantify errors due to possible deviations from this best fit X-ray model. To determine the error in the individual cluster density profile parameters MM2000 also used Monte Carlo simulations. For each cluster, they smoothed the original composite 0.5-2.0 keV count-rate image using a 30″ FWHM Gaussian. A set of 10^3 simulated observations were then created by multiplying the smoothed image by the exposure maps and adding random Poisson noise. For each simulated observation, they applied the same analysis procedure that was used to determine the cluster parameters from the original data set. We use their resulting distribution of β-model parameters, β, θ_0, and n_{e0} to determine the expected error in $h^{-1/2}$ due to possible ambiguities in the density profile modeling for each cluster. We generated 10^3 simulated CBI data sets using the different β-model parameter trios from the simulated X-ray observations to generate slightly different SZE profiles. We then fitted for the SZE decrement ΔI using the best fit X-ray parameters from the original *ROSAT* image. The resulting distribution in $h^{-1/2}$ provides expected errors due to possible inaccuracies in the density profile modeling. Because

the X-ray emission and SZE have different dependences on the model parameters, there is a slight bias in the SZE distribution relative to the X-ray distributions.

We can calculate this bias factor by showing the impact the distribution of model parameters has on the SZE model fitting. The best-fit model is calculated by minimizing χ^2:

$$\chi^2 = \sum_j \left(\frac{V_{dj} - V_{mj}}{\sigma_j} \right)^2, \tag{4.14}$$

where V represents the visibility data, which we write as $V(u,v) \equiv I\hat{V}(u,v)$, and the index j indicates a summation over each visibility data point. I represents the overall scaling, which is a simple function of θ_0, β, and n_{e0} (from the factors that come out of the SZE volume integral and is $\propto n_e \theta_0 \frac{\Gamma(3\beta/2-1/2)}{\Gamma(3\beta/2)}$)); $\hat{V}$ represents the part of the fit that depends on the shape of the cluster and is a more complicated function of θ_0 and β (i.e., it's the Fourier transform of the β-model image).

We use the subscripts d and m to represent the data and the model, respectively. In the model, we define $h \equiv 1$. I_d has an implicit dependence on $h^{-1/2}$, which is what we're ultimately fitting for. To be explicit,

$$I_d \propto n_d \theta_d \frac{\Gamma(3\beta_d/2 - 1/2)}{\Gamma(3\beta_d/2)} h^{-1/2} \tag{4.15}$$

and

$$I_m \propto n_m \theta_m \frac{\Gamma(3\beta_m/2 - 1/2)}{\Gamma(3\beta_m/2)} (h = 1). \tag{4.16}$$

After minimizing χ^2, we have

$$\sum \frac{I_d \hat{V}_{dj}^2}{\sigma_j^2} = \sum \frac{I_m \hat{V}_{mj} \hat{V}_{dj}}{\sigma_j^2}, \tag{4.17}$$

which we can rewrite as

$$n_d \theta_d \frac{\Gamma(3\beta_d/2 - 1/2)}{\Gamma(3\beta_d/2)} h^{-1/2} \sum \frac{\hat{V}_{dj}^2}{\sigma_j^2} = n_m \theta_m \frac{\Gamma(3\beta_m/2 - 1/2)}{\Gamma(3\beta_m/2)} \sum \frac{\hat{V}_{mj} \hat{V}_{dj}}{\sigma_j^2}. \tag{4.18}$$

By putting together all the above pieces, we see that the estimated value of $h^{-1/2}$ from the model-

fitting is represented by

$$h^{-1/2} = \left\langle \frac{n_m \theta_m \frac{\Gamma(3\beta_m/2-1/2)}{\Gamma(3\beta_m/2)} \sum \frac{\hat{V}_{mj}\hat{V}_{dj}}{\sigma_j^2}}{n_d \theta_d \frac{\Gamma(3\beta_d/2-1/2)}{\Gamma(3\beta_d/2)} \sum \frac{\hat{V}_{dj}^2}{\sigma_j^2}} \right\rangle, \tag{4.19}$$

which will not be the same as the actual value of $h^{-1/2}$ if the model parameters derived from the X-ray observations are slightly different from those of the actual data. To determine the bias in the distribution of $h^{-1/2}$ due to the model parameters, we calculate the quantity $(h_{obs}^{-1/2}/h_{true}^{-1/2})$ for each of the groups of model parameters in the distribution. The mean of this distribution is the X-ray model bias factor, listed in Table 4.4. The bias corrections are mostly negligible, but A754, a highly disturbed cluster with a larger degree of model parameter uncertainty, requires a correction of 3.6%.

4.4.3 Temperature Profiles

Our analysis also assumes that cluster gas is isothermal. If this assumption is correct, determining errors from inaccuracies in the value of T_e is straightforward; $h^{-1/2}$ is simply proportional to T_e. Whether the gas is in fact isothermal has been the subject of ongoing debate. In their analyses of the same *ASCA* data, Markevitch et al. (1998) find temperature profiles which decline with radius, while White (2000) finds isothermal profiles. De Grandi & Molendi (2002) also find declining profiles from their analysis of *BeppoSAX* data, but they find that the profiles have a slightly different slope and break radius from the Markevitch et al. (1998) profiles. *XMM-Newton* observations indicate that individual clusters may vary; A1795 has a temperature profile consistent with isothermal out to 0.4 $r_{\rm vir}$ while Coma shows a declining temperature profile (Arnaud et al., 2001b,a). Departures from isothermality can produce large errors in the derivation of H_0 from the X-ray/SZE method if an isothermal model is assumed, but the magnitude of the error depends on many factors.

To estimate the possible effect of an inaccurate temperature profile, we study the case of gas modelled as a hybrid isothermal-polytropic temperature profile, where the temperature is uniform out to a radius $r_{\rm iso}$, and declines outside this radius. This model was introduced by Hughes et al. (1988) and is similar to the profile found by Navarro et al. (1995) in N-body simulations. It is

represented by

$$T(r) = \begin{cases} T_0 & \text{if } r \leq r_{\rm iso} \\ T_0 \left(\frac{n(r)}{n(r_{\rm iso})} \right)^{\gamma - 1} & \text{if } r > r_{\rm iso} \end{cases} . \tag{4.20}$$

Theoretical calculations disagree on where the transition radius $r_{\rm iso}$ should occur, although it is generally taken to be of order a virial radius, $r_{\rm vir}$, which we approximate as r_{200}, defined in the manner of Evrard et al. (1996) as the radius which encloses a mean density 200 times the cosmological critical density.

In the limit where $r_{\rm iso} = 0$, the temperature profile is simply a polytropic model. We expect $1 < \gamma < 5/3$, where $\gamma = 1$ is the isothermal limit, and $\gamma = 5/3$ is the adiabatic limit. The expected central SZE decrement depends fairly strongly on γ and $r_{\rm iso}$, but the effect of these parameters on the derivation of H_0 using interferometric SZE data is not completely straightforward. A hybrid temperature profile will cause two changes relative to an isothermal model. The overall decrement will be smaller, and the cluster will appear more compact. The interferometer measures visibilities which are the Fourier transform of the image, so a steep image profile will have a shallower visibility profile and vice versa. Because the visibility profile shallows as $r_{\rm iso}$ is decreased, the hybrid profiles cross the isothermal profile at different points. Therefore, it is difficult to know whether we will overpredict or underpredict H_0 for different clusters without an accurate temperature profile.

We demonstrate this with a simulation which is summarized in Table 4.5. We generated false SZE data sets using hybrid models with different pairs of γ and $r_{\rm iso}$ where the input models all assumed $h = 1$. For each model, we rescaled T_0 such that the emission weighted temperature for that model agreed with the observed value. We then fitted an isothermal profile to the hybrid model data to determine the error in deriving H_0 due to the temperature profile. Table 4.5 lists our results for A478. We see that for steeply declining profiles, our error in h will be very large, and can be incorrect by a factor of 2 in the most extreme case. Some cases supported by observational data include $r_{\rm iso} = 0$, $\gamma = 1.2$ (Markevitch et al., 1998) and $r_{\rm iso} = 0.2$, $\gamma = 1.5$ or $\gamma = 1.2$ for non-cooling flow and cooling flow clusters, respectively (De Grandi & Molendi, 2002). If the Markevitch et al. (1998) profile is correct, then we overestimate h from A478 by 22%; if the De Grandi & Molendi

Table 4.5 Values of h for A478 from isothermal fits to nonisothermal cluster data. $r_{\rm iso}$ is in units of r_{200}.

$r_{\rm iso} \setminus \gamma$	1.6	1.5	1.4	1.3	1.2	1.1
0.0	2.06	1.81	1.59	1.39	1.22	1.10
0.1	1.42	1.33	1.24	1.16	1.09	1.04
0.2	1.01	1.00	0.99	0.98	0.98	0.98
0.3	0.90	0.91	0.92	0.93	0.95	0.97
0.4	0.88	0.89	0.91	0.92	0.94	0.97
0.5	0.89	0.90	0.92	0.93	0.95	0.97
0.6	0.91	0.92	0.93	0.95	0.96	0.98
0.7	0.94	0.94	0.95	0.96	0.98	0.99
0.8	0.96	0.96	0.97	0.98	0.98	0.99
0.9	0.97	0.98	0.98	0.99	0.99	1.00
1.0	0.99	0.99	0.99	0.99	1.00	1.00

(2002) profile is correct, then our value of h is largely unaffected by the temperature profile. The errors can be very different for different clusters, and in some cases go in the opposite direction, where h is underestimated for steeply declining temperature profiles. We summarize in Table 4.7 the levels of error expected if the mean *ASCA* and *BeppoSAX* profiles apply to each of our clusters. For the De Grandi & Molendi (2002) profiles, we have boldfaced the relevant column, based on whether a particular cluster is believed to have a cooling flow or not. Depending on which mean profile is assumed, for the sample of 7 clusters presented here, our value of h may be essentially correct, with an overestimate of only 1% based on the Markevitch et al. (1998) profile, or it could be underestimated by 14% assuming the De Grandi & Molendi (2002) mean profiles. This demonstrates that an accurate knowledge of the temperature profile is important for eliminating a bias in H_0 from non-isothermal cluster temperatures. To determine $r_{\rm iso}$ and γ, the profiles need to be probed to a large radius, typically tens of arcminutes for our clusters, which means that *Chandra* observations alone are usually not adequate for these purposes.

4.4.4 Errors from Foreground Point Sources

Foreground point sources are the largest source of contamination in CMB experiments at 30 GHz. We hope to limit the point source error in our H_0 determination to $< 2\%$ for the sample of 15 clusters, or $< 8\%$ per cluster. Our strategy for removing point source contamination involves a

combination of fitting for the fluxes of sources at known positions simultaneously with the cluster model, and independently measuring some source fluxes with the OVRO 40-m telescope and the VLA. The CBI short ($\leq$2 m) baselines are most sensitive to the signal from the extended cluster and CMB primary anisotropies. The strength of the cluster and CMB both decline significantly on longer baselines, making those baselines suitable for determining point source fluxes. However, this source fitting is not reliable for sources near the cluster center, and we use independent observations to accurately determine their fluxes. The advantage of fitting the source fluxes using the CBI data is that the point source and cluster observations are simultaneous, so source variability is not an issue, although most point sources in clusters are steep spectrum and non-varying (e.g., Slingo, 1974; Cooray et al., 1998). The disadvantage is that for sources close to the cluster center, the point source appears as an overall offset on all baselines in the visibility domain where we perform the fitting. The overall offset from the point source is difficult to distinguish from the cluster signal, especially in the less resolved, compact clusters such as A478 and A401, resulting in large errors in the H_0 analysis. We find that sources close to the cluster center within about $10'$ need to be observed independently with very high accuracy (about 1 mJy rms at 31 GHz), and sources outside this radius can be safely fitted using the CBI long baselines. We fit sources outside the $10'$ radius that have fluxes detectable at the 2.5-σ limit, and we account for the contribution of the remaining (unfitted and unsubtracted) sources statistically using Monte Carlo simulations which we describe below. As a basis for our study, we use the NVSS catalog, which is complete to 2.5 mJy at 1.4 GHz. We assume that all relevant sources at 30 GHz are in the NVSS catalog and that we do not miss any sources with inverted spectral indices. This assumption is supported by our OVRO study and VLA X-band survey of one of the blank CMB fields, as well as a study of point sources in the CBI Deep fields (Mason et al., 2003). Although Taylor et al. (2001) do find from their 15 GHz survey a large chance of missing inverted spectrum sources from extrapolations from low frequency, we estimate based on their source counts that the probability of such a source occuring in the crucial central $10'$ of our cluster centers is low. Sources outside this radius do not contribute a significant error, as we explain below.

To test our source subtraction method and quantify errors, we generated simulated cluster observations using the X-ray derived density models described above, including realistic thermal noise and CMB primary anisotropies. We added all NVSS sources (down to 2.5 mJy at 1.4 GHz) to each simulated cluster realization at the listed NVSS positions, but we varied the fluxes for each iteration by randomly selecting spectral indices from the distribution observed by Mason et al. (2003) to determine the source fluxes at each of the CBI channels from 26 to 36 GHz. We then defined specific criteria to determine how the different sources would be treated in the analysis.

If a source was within $10'$ of the LMT pointing centers, we "subtracted" the source, assuming its flux is known to a certain rms from an independent telescope. In the simulations we added at these source positions, random Gaussian noise with an rms equivalent to the levels observed with the OVRO 40-m telescope. The sensitivity achieved with the 40-m varied from 0.4 to 2.0 mJy rms for individual sources. The simulations show that these central point sources observed with the 40-m contribute $\sim 10\%$ error per cluster.

If a source was outside the $10'$ radius and could be detected at the 2.5-σ level on baselines longer than 2.5 m, we fitted for the flux of the source simultaneously with the cluster. Before selecting the 2.5-σ sources in the simulations, we added random fluctuations to the source fluxes to simulate possibly missing some sources due to noise. All other sources were ignored (i.e., not subtracted or fit for in any way). In the fitting, we fixed the source positions to the NVSS coordinates, which is reasonable since the rms error in the NVSS positions ranges from $< 1 - 7''$, much smaller than the CBI synthesized beam of a few arcminutes. We found that it was extremely inefficient to fit for the spectral indices of large groups of point sources over the CBI 10 GHz bandwidth, so we fixed them at the weighted mean value of the distribution found by Mason et al. (2003), $\alpha = -0.55$. To determine whether this assumption affects our results, we also tried fixing the spectral index to $\alpha = 0$. We found that the H_0 results change by $< 1\%$ in all cases. In the simulations the small number of sources whose fluxes are determined from the CBI data itself (typically 10-15 per cluster) contribute a negligible amount of error to the $h^{-1/2}$ fits.

All sources that were outside the $10'$ radius and were not at least 2.5-σ were ignored in the SZE

fitting. We compare these simulations with those described in Section 4.4.1, where only observational noise and CMB anisotropies are added. The 10^3 Monte Carlo iterations show that the unsubtracted sources contribute a small but consistent bias, tending to make the mean $h^{-1/2}$ for a cluster higher or lower, depending on the configuration of residual sources present in the LMT fields. The bias from the unsubtracted sources is an additive factor, and the values for the individual clusters are listed in Table 4.4.

The spectral index distribution determined by Mason et al. (2003) was derived for observations of cluster-free CMB fields. The point source populations in galaxy clusters can be considerably different, and have not been well studied at 30 GHz. Cooray et al. (1998) find a distribution of -0.77 ± 0.48, which is somewhat different from the Mason et al. (2003) distribution. We retest our method using the Cooray et al. (1998) distribution instead of the Mason et al. (2003) distribution, and find the results to be almost unchanged. The sample value of $h^{-1/2}$ changes by <0.3%, and the magnitude of the sample error changes by <1%.

4.4.5 Other Error Sources

4.4.5.1 Asphericity

Because of the CMB contamination, we cannot meaningfully study the cluster shapes as seen in the SZE from the CBI data. Any errors in $h^{-1/2}$ from slight pointing inaccuracies on the level seen in the CBI, offsets in x, y from the assumed cluster center up to a few arcminutes, or ellipticity in the plane of the sky are all dwarfed by the CMB, so we ignore them here. The 2-D shapes of clusters seen in X-ray emission provide a good indicator of the level of expected asphericity. Cooray (2000) has analyzed the 2-D distribution of X-ray cluster shapes observed by Mohr et al. (1995), showing that for a sample of 25 clusters randomly drawn from an intrinsically prolate distribution, the error in H_0 for the sample is less than 3%. Therefore, for our complete sample, we do not expect a large systematic error due to cluster asphericity. We estimate the uncertainty in H_0 for each cluster by taking $3\% \times \sqrt{25} = 15\%$, so the uncertainty for each cluster in $h^{-1/2} \sim 7.5\%$. For our primary sample of 15 clusters, the error in H_0 due to asphericity should be <4%, which is very reasonable.

4.4.5.2 Clumpy Gas Distribution

In the fitting, we assume that the density distribution is smooth, directly applying the density profile model derived from the X-ray observations to the SZE models. Because the CMB is such a large contaminant, and we cannot meaningfully obtain shape parameters from the SZE data, potential systematic errors due to clumpy gas cannot be addressed with our data and can probably only be understood in detail through hydrodynamical simulations. However, Equation 1.10 and Equation 1.12 show that $h \propto \langle n_e^2 \rangle / \langle n_e \rangle^2$, a quantity which is always greater than unity. Therefore, any clumpiness in the gas distribution will cause one to overestimate h by this factor, although as we saw from our study of different temperature profiles that the analysis for interferometer data could be more complicated than this.

4.4.5.3 Peculiar Velocities

The expression given for the thermal SZE in Equation 1.9 assumes that the cluster is not moving with respect to the Hubble flow. In reality, all clusters have some peculiar velocity $V_{\rm pec}$, taken to be at an angle θ relative to the vector drawn from the cluster to the observer. This produces a kinematic SZE given by

$$\frac{\Delta I_{\rm kin}}{I} = \tau \frac{x e^x}{e^x - 1} \left\{ \frac{V}{c}\mu + \left(\frac{V}{c}\right)^2 \left(-1 - \mu^2 + \frac{3 + 11\mu^2}{20} F \right) + \frac{V}{c} \frac{k_b T_e}{m_e c^2} \mu \left[10 - \frac{47}{5} F + \frac{7}{10}(2F^2 + G^2) \right] \right\} \tag{4.21}$$

(Sazonov & Sunyaev, 1998), where all quantities are as defined in Section 4.3, and $\mu = \cos\theta$. The first term is the kinematic SZE, which can be positive or negative, depending on whether the cluster is moving away from us or towards us. The second term is a relativistic correction to the kinematic SZE, and the third part of the expression is a cross-term between the thermal and kinematic effects. The last term is the dominant correction to kinematic SZE measurements in single clusters. For our purposes, we can assume that the clusters have random peculiar velocities along our line of sight, and the terms in V/c will average out over the sample, although we will consider their contribution to our error budget for each individual cluster below. The $(V/c)^2$ term will not average out for the

sample, but its magnitude is very small, even for large peculiar velocities.

Giovanelli et al. (1998) measured the peculiar velocities of 24 galaxy clusters with radial velocities between 1000 and 9200 km s^{-1} ($z < 0.03$). None of the peculiar velocities in the CMB reference frame exceed 600 km s^{-1}, and their distribution has a line of sight dispersion of 300 km s^{-1}. The mean magnitude of their observed radial peculiar velocities is $\sim$200 km s^{-1}. Slightly larger peculiar velocities are found in numerical simulations created by the Virgo Consortium (e.g., Kauffmann et al., 1999). Colberg et al. (2000) find from the simulations that for haloes with masses comparable to the clusters in our sample ($M > 3.5 \times 10^{14} h^{-1} \mathrm{M}_{\odot}$), the peculiar velocities range from about 100$-$1000 km s^{-1} for a ΛCDM cosmology, with 11 out of 69 clusters having $V_{\mathrm{pec}} > 600$ km s^{-1}. The average peculiar velocity for the ΛCDM model is about 400 km s^{-1}. We calculate the error in $h^{-1/2}$ due to the kinematic SZE for each cluster assuming V_{pec} =400 km s^{-1} and list the values in Table 4.4. For the weakest cluster in our sample, A2597, a large peculiar velocity of 1000 km s^{-1} produces an error in $h^{-1/2}$ of $\sim$0.04% from the $(V/c)^2$ term. Thus, there is no systematic error in the sample from ignoring the kinematic SZE relativistic correction. Errors due to the kinematic/thermal SZE cross term are negligible ($< 0.1\%$) for all cases.

4.4.5.4 Comptonization due to Nonthermal Populations of Electrons

Clusters which have recently merged are usually associated with radio relics or haloes. This non-thermal emission can affect our results in two possible ways. If the halo is extremely bright, it can cause contaminating foreground emission at 31 GHz. As noted in the sections on the individual clusters, two clusters discussed in this paper, A401 and A754, have haloes at lower frequencies, but due to their steep spectral indices, we do not expect them to contribute significant flux at 31 GHz. The second possible effect is a contribution to the SZE from the nonthermal population of electrons present in the cluster. Quantifying this effect is very difficult, even with detailed radio, EUV, and X-ray data because the electron population models are not well-constrained by the observational data. Shimon & Rephaeli (2002) have studied four different electron population models that can reproduce observed data from the Coma cluster and A2199. Three of the four models produce a

negligible contribution to the total SZE from the nonthermal population of electrons ($< 1\%$ in most cases). The fourth model nonthermal electron population contributes 6.8% and 34.5% of the total SZE flux in the two clusters, but that model is deemed to be unviable by the authors because the ratio of the total energy in the nonthermal electrons to that in the thermal electrons is too high to be realistic. One of the three viable models produces a contribution of 3% to the total SZE in A2199. Colafrancesco et al. (2003) also calculate the contribution to the SZE from nonthermal electrons, using fewer approximations than Shimon & Rephaeli (2002). Their results are similar in that the magnitude of the nonthermal SZE is highly dependent on the model used to represent the electron population. Here, we simply note that Comptonization by a nonthermal electron population is a possible source of additional error in our result, although current plausible models indicate that the magnitude of the error may be negligible.

4.5 Combined Results

To determine the total error for each individual cluster, we can combine independent sources of error by adding them in quadrature if they are Gaussian, or convolving the different likelihood distributions if they are not. However, since all the Monte Carlo simulations depend so heavily on the CMB noise, it is difficult to separate the independent components. For example, the CMB has a large effect on how well the point sources can be fitted, as do the X-ray models. In the point source fitting, we assume we completely understand the shape of the SZE profile based on the X-ray data. If the profile is slightly wrong, this can affect the point source subtraction. We therefore perform a final simulation set where all the major sources of error - CMB, point sources, and X-ray models - are varied simultaneously. Here we only consider the isothermal β-models described in MM2000. We list in Table 4.4 the 68% confidence intervals in $h^{-1/2}$ for each cluster, given the various sources of error. Note that these errors are absolute, not fractional. The reason is that the CMB dominates the error, and it effectively adds or subtracts flux to the cluster and is not a scaling factor, although the fractional expected error in $h^{-1/2}$ is a function of the cluster signal and shape, where brighter, more compact clusters experience less contamination.

Table 4.6. Final results

Cluster	Corrected $h^{-1/2}$ w/ total random error	ΔT_0 μK	Compton-y_0 ($\times 10^{-4}$)
A85	1.23±0.40	-580±190	1.13±0.37
A399	0.24±0.42	-80±130	0.15 ±0.26
A401	1.03±0.29	-620±170	1.20 ±0.34
A478	1.76±0.34	-1800±350	3.49±0.68
A754	1.09±0.31	-560±160	1.09±0.31
A1651	1.42±0.47	-520±170	1.00±0.33
A2597	1.74±1.10	-750±670	1.43±1.28
mean ± sd =	1.22±0.52		
(probability=21%)	$\frac{\chi^2}{\nu} = 1.47$ for 6 dof		
unweighted sample average: $h^{-1/2}$=	1.22±0.20		
→	$h = 0.67^{+0.30}_{-0.18}$		
weighted sample average: $h^{-1/2}$=	1.16±0.14		
→	$h = 0.75^{+0.23}_{-0.16}$		

The values in this table have been corrected for the X-ray and unsubtracted point source biases. The errors listed are 68% confidence random errors from the CMB anisotropies, thermal noise, calibration errors, point source subtraction, asphericity, temperature determination (within context of an isothermal model), and peculiar velocities.

The final $h^{-1/2}$ results, corrected for the X-ray model and unsubtracted point source biases, are presented in Table 4.6 with their 68% random uncertainties from CMB anisotropies, thermal noise, calibration errors, point source subtraction, asphericity, temperature determination (within context of an isothermal model), and peculiar velocities. Central values of ΔT_0 and y_0 which have also been corrected for the X-ray model and unsubtracted point source biases are listed as well.

As we have emphasized, a major potential bias in determining H_0 from combined SZE/X-ray observations is asphericity in the clusters. Weighting by the errors could possibly bias the sample average if the magnitudes of the errors correlate with properties of the cluster that relate to the asphericity bias. For example, an elongated cluster oriented along the line of sight would appear more compact than the same cluster oriented perpendicular to the line of sight. Thus, if the magnitudes of the errors in our determination of H_0 correlate with the sizes on the sky of the clusters, a sample result which has been weighted by the errors could potentially be biased. We determine the apparent sizes of each cluster by calculating the FWHM of the β-model. We plot the errors from our H_0 analysis against the apparent size for each cluster in Figure 4.3. The most compact cluster,

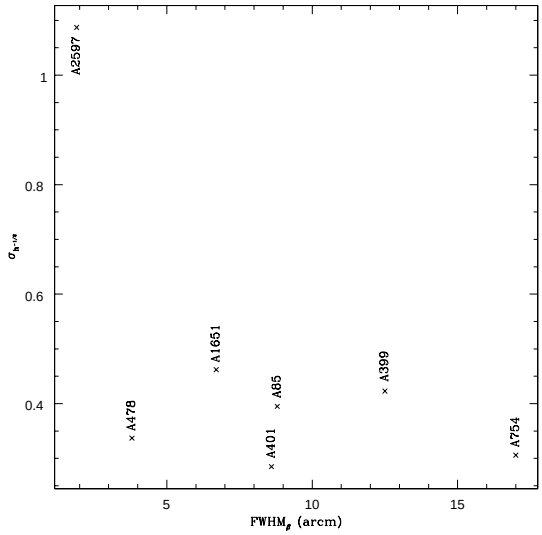

Figure 4.3 Plot of the uncertainty in $h^{-1/2}$ vs. the size of the cluster. For each cluster, the size is represented by twice the radius at which the β-model SZE signal is half that of the peak.

A2597, is also one of the least luminous objects in the sample. Since its signal is relatively weak, the error due to CMB contamination is significant. If we exclude this cluster, there is very little correlation between the errors and cluster size, with a correlation coefficient $r = -0.16$; with this one anomalous object, $r = -0.58$.

First, to avoid any possible bias, we simply take a straightforward average of the $h^{-1/2}$ results and errors. The unweighted average is $H_0 = 67^{+30+15}_{-18-6}$ km s^{-1} Mpc^{-1}for this sample of 7 clusters, where the first set of uncertainties represents the random error at 68% confidence, and the second set represents systematic errors corresponding to calibration uncertainties and possible bias due to a nonisothermal profile, for which we use the average sample biases from Table 4.7. As discussed in Section 2.2.3, A754 is a merging, disturbed cluster. If we exclude it from the final result, we obtain $H_0 = 65^{+34+14}_{-19-6}$ km s^{-1} Mpc^{-1}from the remaining 6 clusters. Given that the correlation between error and cluster size is not large, we also present a weighted sample average, with the caveat that there is a possibility of the result being biased. The sample average weighted by the errors gives $H_0 = 75^{+23+16}_{-16-7}$ km s^{-1} Mpc^{-1}. Weighting the average increases the sample result significantly, perhaps supporting our hypothesis above that A2597 (which contributes less to a weighted average

Table 4.7 Values of $h^{-1/2}$ for the clusters in our sample from isothermal fits to nonisothermal cluster data. $r_{\rm iso}$ is in units of r_{200}. The numbers in the DM2000 columns are boldfaced depending on whether each cluster is a cooling flow or not. The boldfaced values are the ones that we use in determining the sample error for the DM2000 mean temperature profile.

	MFSV	DM (no CF)	DM (CF)
$r_{\rm iso}, \gamma$	0,1.2	0.2,1.5	0.2, 1.2
A85	1.07	1.18	**1.09**
A399	1.07	**1.14**	1.08
A401	1.04	**1.12**	1.06
A478	0.90	1.00	**1.01**
A754	1.12	**1.22**	1.11
A1651	0.97	**0.99**	1.01
A2597	0.77	0.91	**0.97**
Avg $h^{-1/2}$	0.99	1.08	
h	1.01	0.86	

due to its large error bars) is an elongated cluster, since clusters elongated along the line of sight yield values of H_0 which are low.

There is a large scatter in the individual $h^{-1/2}$ results, but the scatter is entirely consistent with the uncertainties. The mean and standard deviation in $h^{-1/2}$=1.22±0.52. For the 7 clusters, the error in the mean is 0.20, which is equal to the sample uncertainty derived from the individual cluster errors of 0.20 from the unweighted average. The reduced χ^2 for the sample mean is 1.47 with 6 degrees of freedom, with a probability of 21% of exceeding this value by chance.

The uncertainties in the H_0 results presented here are dominated by confusion due to the CMB primary anisotropies. In this analysis, when fitting the SZE models to the visibility data, we weight only by the thermal noise. An obvious improvement would be to take advantage of the fact that we know the CMB's angular power spectrum (Mason et al., 2003; Pearson et al., 2003), and weight the visibility data by the level of power in the CMB on a particular angular scale when performing the modelfitting. However, the errors due to the CMB are highly correlated for visibilities which are close to each other, and this correlation must be removed by diagonalizing the CMB covariance matrix. Details of this method will be described in a future paper (Udomprasert & Sievers, in preparation). We note here that by using this improved weighting method, the errors in our result above would be reduced by $\sim 30\%$ for this sample of 7 clusters.

4.6 Comparison with Past SZE Observations

Mason et al. (2001) (hereafter MMR) and Myers et al. (1997) observed four of the clusters presented in this paper, A399, A401, A478, and A1651, with the OVRO 5-m telescope. We compare the CBI results with the OVRO 5-m observations. MMR reanalyzed A478 observations taken by Myers et al. (1997), and we use the MMR results here. There are a few differences between the CBI and OVRO 5-m observations which must be taken into account. First, for all 4 clusters, different lead and trail fields were observed by the 2 groups. These differing fields contribute significant errors to the results. Also, slightly different redshifts, electron temperatures, and cosmologies were assumed in the 2 analyses. If we take these into account and fit models to the CBI data using all the same parameters assumed by MMR, the results we would obtain are presented in Table 4.8. Errors from the CMB in the main fields will be correlated for the 2 observations, since the same patch of CMB is being observed. However, the CMB contribution should not be identical because the interferometer and single dish measurements are sensitive to different modes of the CMB. Calculating the correlated error in the main field is complicated, so instead we performed the following estimate. We compared our results to those of MMR assuming two different uncertainties. In our first comparison, we included the entire 68% confidence errors as quoted in MMR, which included errors due to contributions from the lead, main, and trail fields, whereas for the CBI measurements, we removed the contribution to the uncertainty from the CMB in the main field, but included uncertainties from CMB in the lead and trail field, as well as thermal noise from the main field. In the second comparison, we removed the contribution to the uncertainty from the main field CMB in the MMR result as well. Table 4.8 shows the results we obtain from these comparisons. We calculated χ^2 to determine the probability due to chance of our results differing by the observed amount, where

$$\chi^2 = \sum \frac{(h_{CBI}^{-1/2} - h_{MMR}^{-1/2})^2}{\sigma_{CBI,LT}^2 + \sigma_{MMR,L(M)T}^2}. \tag{4.22}$$

For the 4 clusters, we obtained χ^2/ν=1.53, for 4 degrees of freedom, with an associated probability of 19% when the main field CMB uncertainty is included once; χ^2/ν=2.43 when the main field

Table 4.8 Comparison of CBI H_0 results with Mason et al. (2001) results. The uncertainties listed for the CBI results only include statistical errors from the lead and trail CMB contamination, and errors from thermal noise in the main field. The MMR results list the quoted uncertaintiess from Table 2 of Mason et al. (2001). The final column lists the uncertainties for the MMR results if one ignores the contribution to the uncertainty from the main field CMB.

Cluster	CBI $h^{-1/2}$ w/ MMR param	MMR $h^{-1/2}$ w/ main CMB	MMR $h^{-1/2}$ uncertainty w/o main CMB
A399	0.23±0.26	$0.99^{+0.44}_{-0.31}$	±0.21
A401	1.06±0.16	$1.40^{+0.29}_{-0.27}$	±0.18
A478	1.65±0.16	$1.28^{+0.28}_{-0.25}$	±0.18
A1651	1.47±0.27	$1.67^{+0.52}_{-0.48}$	±0.33

CMB was ignored completely, with a probability of 5%. We expect the actual value to be something between these, showing that the CBI and OVRO 5-m results are in reasonable agreement.

Chapter 5

CMB Weighting

As discussed in Chapter 4, the most significant source of noise in SZE analyses at low redshift is the CMB intrinsic anisotropies[1]. In this chapter we describe a method designed to minimize the error in SZE measurements due to CMB fluctuations in the case of interferometric studies, and we apply our method to simulated CBI SZE observations.

5.1 CMB as Noise

Figure 5.1 shows the observed power spectrum measured by the CBI from three mosaics. The CBI observations tell us the magnitude of expected CMB contamination on all baselines for which we have SZE data, and we can use this information in our analysis. First, we consider the implications such a power spectrum has on the SZE data. We already examined this through Monte Carlo simulations in Chapter 4, but those do not provide an intuitive feel for how the CMB affects each baseline in different clusters. Here, we look at the simulated CMB maps in a slightly different way. Because the clusters are modeled as spherically symmetric objects, fitting a profile to the visibility data is essentially equivalent to azimuthally averaging the data, so we treat the CMB in the same way. First we calculate the rms of the radially averaged CMB visibility data over many CMB realizations. We multiply each of 10^3 simulated CMB maps described in Section 4.4.1 by the CBI primary beam and FFT the data to obtain the visibility grid. We then radially average the visibility data at several steps in q to obtain the "CMB profile" for that particular realization of the CMB. The visibilities

[1]Who would have thought that one of the most important signals in all of cosmology could cause a graduate student such headaches??

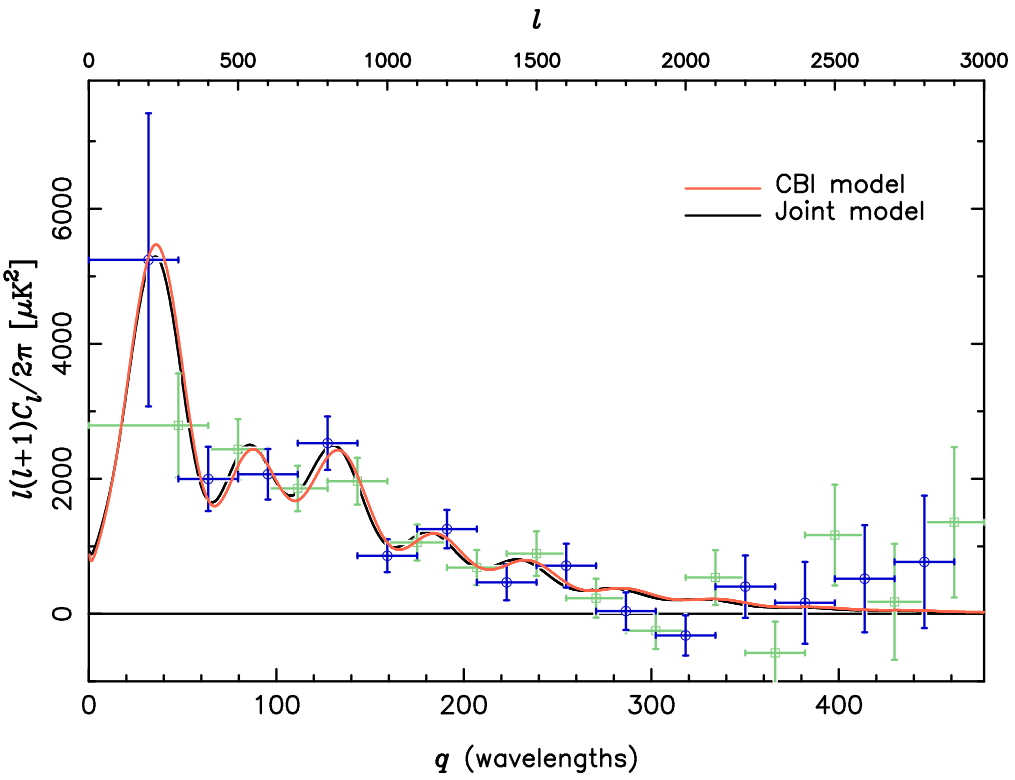

Figure 5.1 Joint power spectrum estimates for the three CBI mosaics (Pearson et al., 2003). Band-power estimates have been made for two alternate divisions of the ℓ range into bins: "even" binning (*green squares*) and "odd" binning (*blue circles*). The error-bars show $\pm 1\sigma$ uncertainties from the inverse Fisher matrix. Two minimal inflation-based models are shown. *Red:* fit to CBI plus *COBE* DMR; $\Omega_{\rm tot} = 1.0$, $\Omega_b h^2 = 0.0225$, $\Omega_{\rm cdm} h^2 = 0.12$, $\Omega_\Lambda = 0.6$, $n_s = 0.95$, $\tau_c = 0.025$, $\mathcal{C}_{10} = 786$ μK^2. *Black:* joint fit to CBI, DMR, DASI, BOOMERANG-98, VSA and earlier data; $\Omega_{\rm tot} = 1.0$, $\Omega_b h^2 = 0.02$, $\Omega_{\rm cdm} h^2 = 0.14$, $\Omega_\Lambda = 0.5$, $n_s = 0.925$, $\tau_c = 0$, $\mathcal{C}_{10} = 887$ μK^2. For details, see Sievers et al. (2003). (For reference, $\ell \sim 600$ corresponds to 100λ).

Table 5.1 RMS of radially averaged contribution of CMB for a range of baseline lengths.

q (wavelengths)	RMS of radially averaged CMB (mJy)
100	28.2
150	13.1
200	6.7
250	4.1
300	2.4
350	1.4
400	0.9
450	0.6
500	0.3
550	0.0

can be positive or negative at different baseline lengths and for different realizations depending on whether hot or cold spots happen to be produced in a particular map. We then calculate statistics for the ensemble of 10^3 realizations. Consider a single $q = 100$. First, we obtain a radially averaged value of the visibility profile at that q for each of the 10^3 simulations. Then we calculate the mean (consistent with zero as expected) and standard deviation of those radially averaged values. The standard deviation is what we take to be the expected rms due to the CMB of a radially averaged profile at $q = 100$. Table 5.1 lists the result of our calculations for a range of q typical of CBI observations.

We now compare these values with the SZE fluxes expected given our cluster models. Figures 5.2 and 5.3 show model SZE visibility profiles for cluster parameters presented in Tables 4.1 and 4.2, and assuming $h = 0.7$. Plotted as error bars are the rms values of the expected CMB contribution at each q. Because the clusters are extended sources, their signal is largest on short baselines and drops off fairly rapidly with baseline length. The shape of the power spectrum causes the CMB to behave in a similar way, and most of the CMB power is contributed on baselines where we expect the strongest SZE signal. Especially for some of the weaker clusters in our sample such as A2597, the CMB can overwhelm the expected SZE signal. This is also reflected in some of the CBI maps presented in Chapter 3; A2597 is a marginal detection at best.

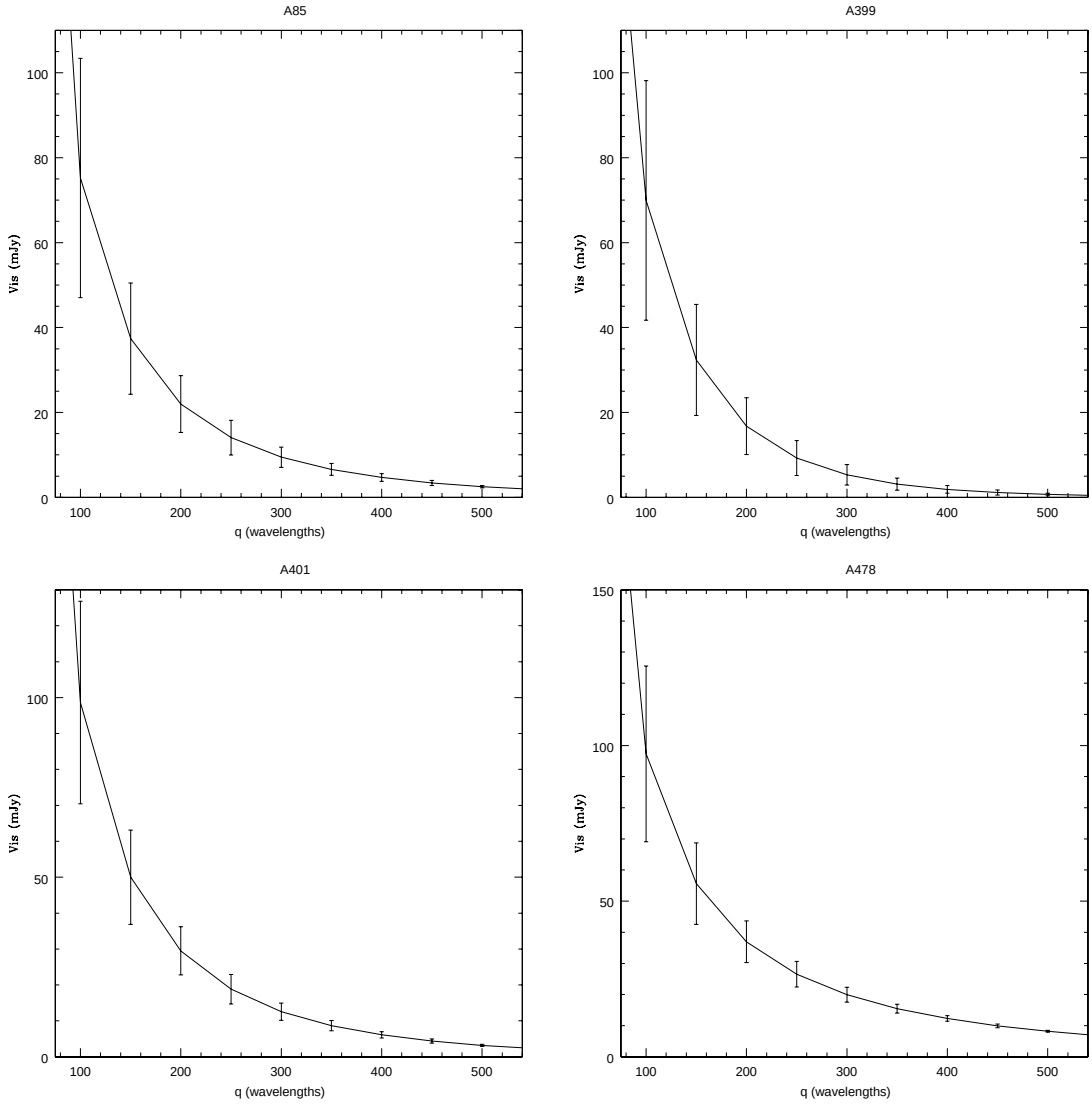

Figure 5.2 Model visibility profiles for A85, A399, A401, and A478 with error bars showing RMS of CMB at each q.

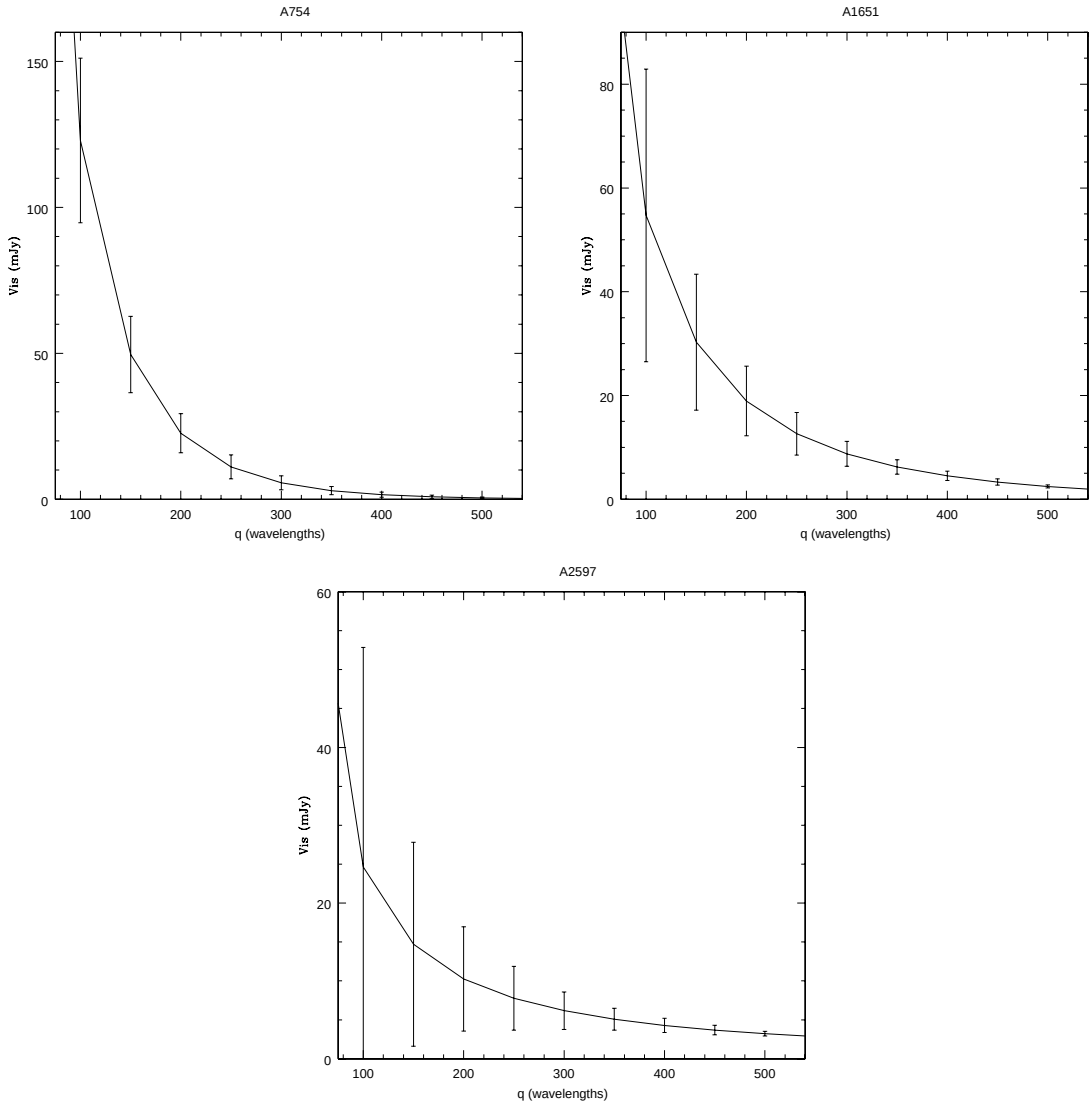

Figure 5.3 As in Figure 5.2, for A754, A1651, and A2597

5.2 Eigenmode Weighting

When fitting for h, we would like to use a weighting scheme which maximally downweights the CMB anisotropies while retaining as much information about the SZE signal as is possible. Naively, it seems that the way to do this would be to weight the data by the expected CMB variance at each baseline. However, the CMB is highly correlated, making it inappropriate as weights in the modelfitting. Instead, one must rotate the data matrix into a basis where the correlations have been removed. This method which we describe here, is related to signal-to-noise eigenmode studies used in CMB power spectrum analyses[2].

First, we make a comparison to the basic case of determining σ, the rms of one-dimensional Gaussian noise with zero mean using a maximum likelihood estimator. The probability of obtaining the data set for a given σ is

$$P(\sigma) \propto \prod_{i=1}^{N} \frac{e^{-v_i^2/(2\sigma^2)}}{\sigma}, \tag{5.1}$$

where v_i represents each data point, and N is the total number of data points. In order to determine the σ which best describes the data set, we would maximize this probability P with respect to σ, and of course we would find that the maximum likelihood σ is simply the standard deviation in the data.

Similarly, we assume the CMB fluctuations are Gaussian noise with zero mean. The strength of the CMB fluctuations is a function of angular scale as described by the power spectrum, so data points corresponding to differing angular scales are assigned their own σ_i's. If the CMB were not correlated on different data points, we could write the product in Equation 5.1 as

$$P = \frac{e^{-\boldsymbol{V}^T \boldsymbol{D}^{-1} \boldsymbol{V}/2}}{\sqrt{\det \boldsymbol{D}}}, \tag{5.2}$$

where $\boldsymbol{V}$ is the vector containing the individual visibility data points v_i, $\boldsymbol{D}$ is the diagonal matrix containing the corresponding σ_i^2's, and $\det \boldsymbol{D}$ is its determinant. In a real observation, thermal noise (which we assume to be independent on different baselines) would be added to the σ_i^2's. The σ_i^2's

[2]This is also known as a Karhunen-Loeve transform (White et al., 1999).

then represent the noise due to CMB+thermal effects that corrupt each data point.

Now, we consider that the CMB signals on differing baselines of an interferometer are correlated since baselines of similar length see almost the same fluctuations. In place of $\boldsymbol{D}$, we define a covariance matrix $\boldsymbol{C}$, which describes the correlation between different baseline pairs, and whose elements are

$$C_{ij} = \langle v_i v_j \rangle, \tag{5.3}$$

where v_i is the observed visibility for one baseline pair, and v_j is the visibility from another baseline pair. Thus, the diagonal elements of $\boldsymbol{C}$ are identical to those of the matrix $\boldsymbol{D}$ above. In the case of $\boldsymbol{C}$ we also add thermal noise along the diagonal. The covariance matrix contains much more information than the simple diagonal matrix; however, it is not immediately obvious how to extract this new information, as there is no longer a single quantity like the σ_i's with which we can weight the data points in the SZE fitting. We must transform the data to a basis where there is an equivalent to the σ_i's.

Each interferometer data point has both a real and an imaginary component, so in practice we must define separate covariance matrices for each. The CMB covariance matrix for the real component is always real and symmetric, and the covariance matrix for the imaginary component is always complex and hermitian. In either of these two cases, the covariance matrix can always be decomposed into an system of orthogonal eigenvectors,

$$\boldsymbol{C} = \boldsymbol{A}\boldsymbol{\Lambda}\boldsymbol{A}^{-1}, \tag{5.4}$$

where $\boldsymbol{A}$ is the matrix containing the eigenvectors along its columns, and $\boldsymbol{\Lambda}$ is the diagonal matrix containing the square of the eigenvalues, λ_i. Because we know the eigenvectors are orthogonal, $\boldsymbol{A}^{-1} = \boldsymbol{A}^T$, and we can easily write

$$\boldsymbol{C}^{-1} = \boldsymbol{A}\Lambda^{-1}\boldsymbol{A}^T. \tag{5.5}$$

Table 5.2 Comparison of predicted errors in $h^{-1/2}$ for no weighting and eigenmode weighting

Cluster	β-FWHM	$\sigma_{\rm nowt}$	$\sigma_{\rm eigwt}$
A85	8.80	0.373	0.292
A399	12.54	0.423	0.379
A401	8.58	0.272	0.210
A478	3.77	0.251	0.183
A754	16.96	0.291	0.264
A1651	6.68	0.437	0.324
A2597	1.92	0.902	0.589
CMB error in $h^{-1/2}$for sample		0.178	0.130
H_0 for sample with uncertainty due to CMB		67^{+25}_{-16}	67^{+17}_{-12}

Substituting Equation 5.5 into Equation 5.2 in place of $\boldsymbol{D}^{-1}$ yields in the exponent

$$\boldsymbol{V}^T\boldsymbol{C}^{-1}\boldsymbol{V} = \boldsymbol{V}^T\boldsymbol{A}\Lambda^{-1}\boldsymbol{A}^T\boldsymbol{V}. \tag{5.6}$$

Hence the eigenvalue decomposition essentially tells us how to get to a new basis $\boldsymbol{Y}$, where $\boldsymbol{Y} = \boldsymbol{A}^T\boldsymbol{V}$, in which the CMB covariance matrix has been diagonalized. The weights for different data points are now independent, and they are given by the eigenvalues, λ_i, which describe the "variance" corresponding to each data point in the new basis. We transform both the data and the model to this new basis and weight the data points by the independent λ_i's, utilizing all of the information contained in the covariance matrix. We call this the "eigenmode" weighting method.

5.3 Application to Simulated CBI Observations

To test our method, we return to Monte Carlo simulations list those described in Chapter 4. We compare the results of the eigenmode weighting scheme to the case where no weighting is used (i.e., the weights in the best-fits to determine h are simply thermal noise, as done in Chapter 4). We simulate the clusters as isothermal β-models, and we add randomized CMB sky images and observational noise. For the eigenmode weighting, we calculate the CMB covariance matrix as described in Equation 5.3, add observational thermal noise along the diagonal, and calculate the eigenvalues and eigenvector matrices. We use the eigenvector matrix to transform both the data and

model to a basis where the CMB modes are independent for each data point, and the eigenvalues are the weights in the best-fit to determine h from the visibility data. We perform 10^3 iterations with different realizations of the CMB, and this gives a distribution of resulting values of $h^{-1/2}$. The 1-σ errors from the eigenmode weighting method are listed in Table 5.2 and are compared with the results of simulations with weighting only by thermal noise. Figures 5.4 and 5.5 show the simulated distributions of derived central SZE decrements using both weighting methods (nowt, just thermal noise vs. eigwt) for 7 clusters, A85, A399, A401, A478, A754, A1651, and A2597. In all the models we input a value of $h = 0.7$, so $h^{-1/2}$= 1.195, although we have not corrected for the model bias described in Section 4.4.2, so small deviations are expected. The means in the sample distributions all agree well with the predicted model values, and the standard deviation represents our 1-σ error in the determination of the central decrement ($\propto h^{-1/2}$).

As expected, the eigenmode weighting significantly reduces the uncertainty in h contributed by the CMB. For the sample of 7 clusters studied here, the uncertainty in $h^{-1/2}$decreases by $\sim 30\%$. Also listed in Table 5.2 are the characteristic angular sizes of each of the clusters. We take these to be the FWHM of the β-model. Figure 5.6 shows the ratio of $\sigma_{\rm eigwt}/\sigma_{\rm nowt}$, a measure of the improvement obtained from the eigenmode weighting, plotted against the cluster angular size. The most compact clusters see the largest improvement from the eigenmode weighting. This is as expected because the eigenmode weighting places greater emphasis on the visibilities with smaller CMB signals; those are the long baselines, and for extended clusters, the SZE visibility profile falls off much more rapidly for extended clusters such as A754 and A399, as seen in Figures 5.2 and 5.2. If there is no detectable cluster signal on the baselines with the least CMB, the eigenmode weighting yields little improvement over weighting by only thermal noise.

5.4 Application to Real Data

Application of the eigenmode weighting scheme to the actual CBI data is still a work in progress. A potential complication is that the models used in simulations are idealizations of an actual cluster. The analysis assumes that we can model the shape of the cluster well, and that there is no clumpiness

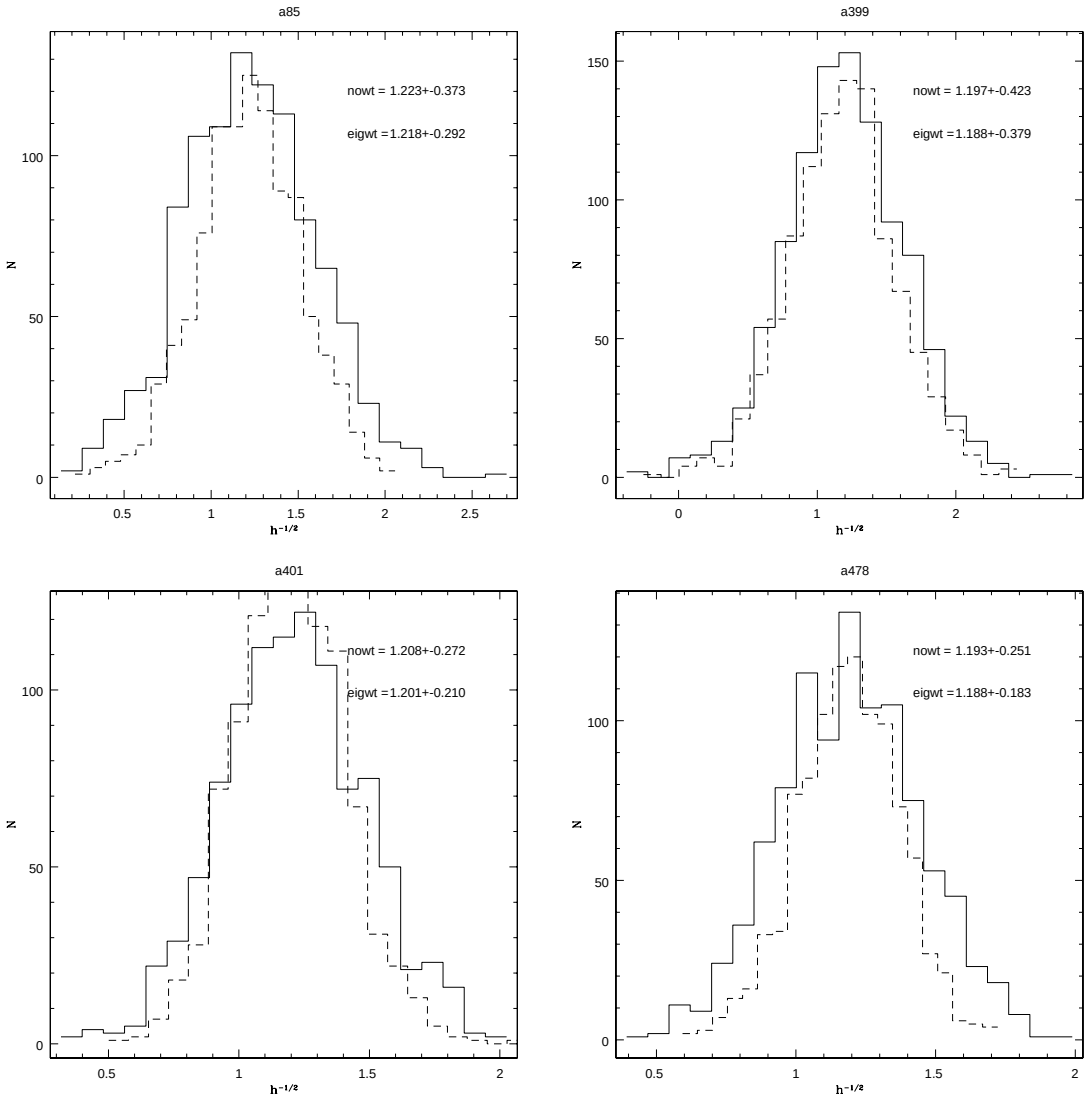

Figure 5.4 Histograms of the best fit $h^{-1/2}$ found for A85, A399, A401, and A478 after 1000 trials with different random CMB "skies" added to the cluster signal. The solid line represents the distribution for fitting done with no weighting; the dashed line is for our eigenmode weighting scheme. Simulations use input $h = 0.7$, so expected $h^{-1/2}$=1.195, although we have not corrected for the model bias described in Section 4.4.2, so small deviations are expected.

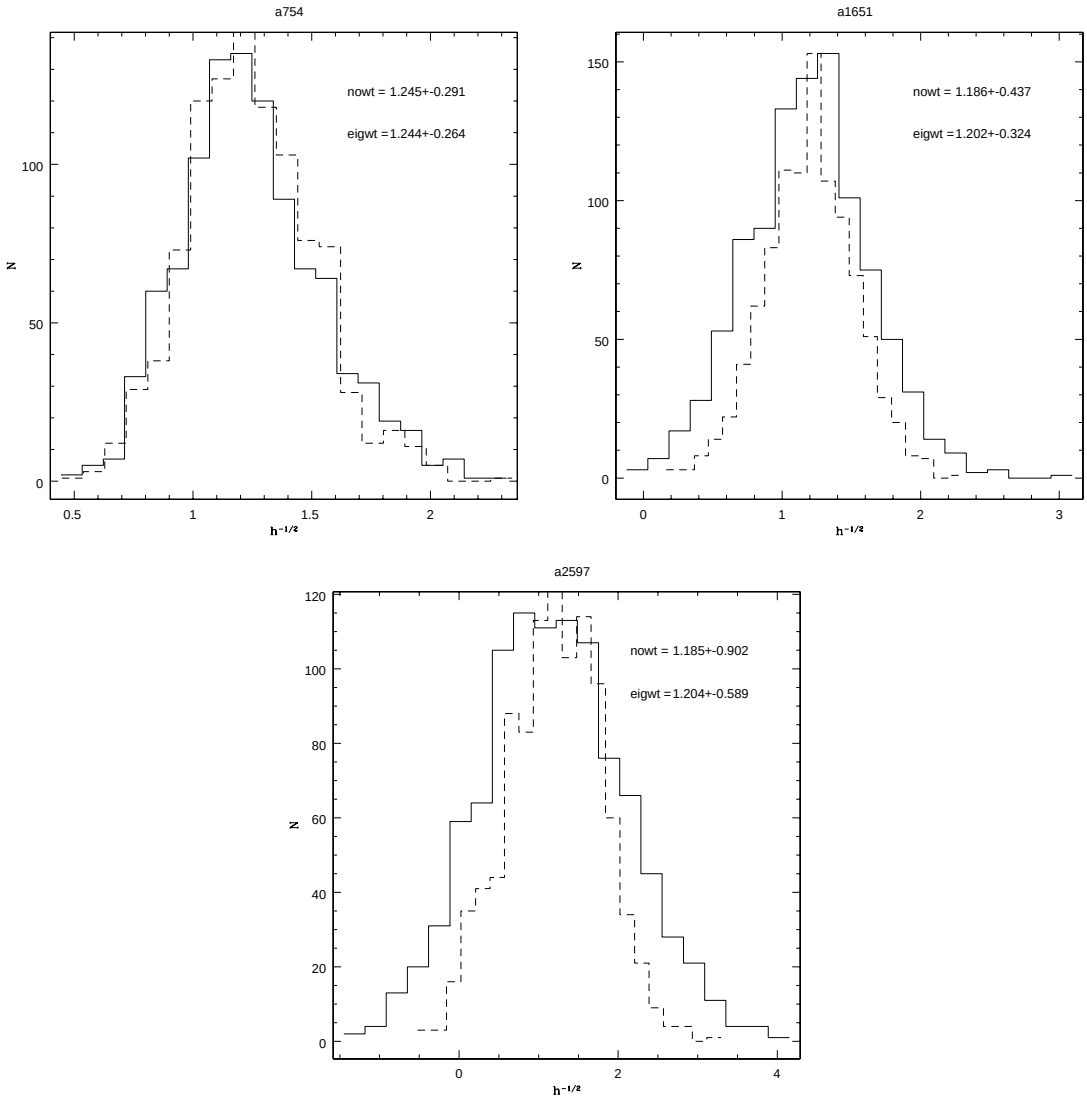

Figure 5.5 As in Figure 5.4, for A754, A1651, and A2597

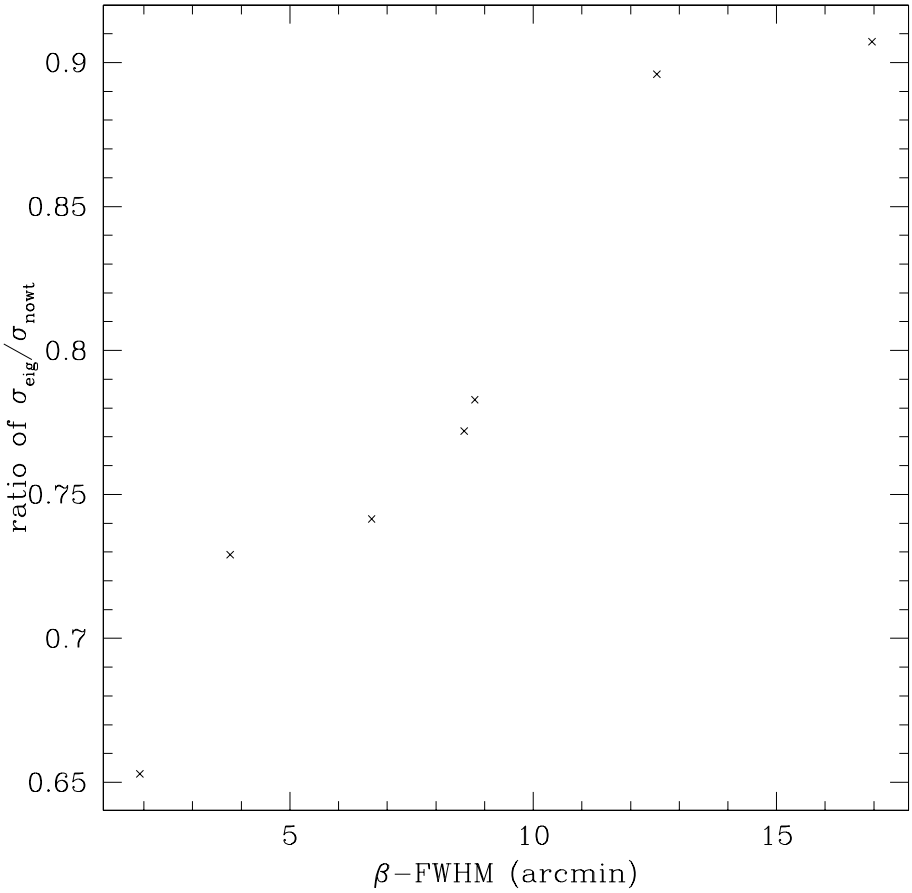

Figure 5.6 Ratio of $\sigma_{\rm eigwt}/\sigma_{\rm nowt}$ vs. FWHM of cluster β-model. The improvement gained from the eigenmode weighting method is a function of the cluster angular size, with smaller clusters benefiting most.

or small-scale structure. Eigenmode weighting would be particularly susceptible to effects of these possible small-scale fluctuations because the long baseline modes are given more weight; since the cluster signal is smaller on those modes, small deviations from the model would matter more. We have not yet included a way to model potential density fluctuations in order to determine their effect.

Real data also have foreground point sources, which we have not yet discussed in the eigenmode analysis method. The most straightforward way to deal with the point sources is to "project" them out, as done in many CMB experiments (e.g., Halverson et al., 2002; Mason et al., 2003). Basically, one calculates the point source covariance matrix based on the positions of known sources and assigns a large weighting factor to the point source covariance matrix, which is then added to the CMB and noise matrices. When this matrix is diagonalized, the eigenvalues provide weights for the correct combination of eigenmodes which essentially blank out the data at the position of the point source.

In summary, the total correlation matrix can be written as

$$\boldsymbol{C}^{\rm tot} = \boldsymbol{C}^{\rm Noise} + \boldsymbol{C}^{\rm CMB} + a_{\rm ptso}\boldsymbol{C}^{\rm ptso}. \tag{5.7}$$

The thermal noise is represented by $\boldsymbol{C}^{\rm Noise}$, usually taken to be a diagonal matrix since the noise should be independent on different baselines. The CMB is given by $\boldsymbol{C}^{\rm CMB}$, and the point source covariance matrix is $\boldsymbol{C}^{\rm ptso}$. The weighting factor used to project out the point sources is a. The actual value used does not matter very much as long as it is much larger than the other weighting factors. Typically, $a \sim 10^5$. This is a cleaner way of handling point source contamination than simultaneous fitting of the fluxes with the SZE data. However, we will still have to use independent measurements of the central point source fluxes. Central point sources overlap spatially with the cluster signal, and if those modes are removed from the data, much of the cluster would be "blanked" with the point sources.

Further tests need to be performed before the eigenmode weighting can be applied to actual CBI data, but we emphasize that this is a potentially powerful method for decreasing the level of contamination from the CMB in the SZE H_0 analysis. In the future (if, for example, the CBI were

to be outfitted with 90 GHz receivers), new observations at higher frequencies could increase further the leverage gained using this method. ACBAR (Runyan et al., 2002), a telescope at the South Pole, has similar angular resolution to the CBI, but it operates at much higher frequencies (150 GHz, 220 GHz, 274 GHz, and 345 GHz). Since the SZE null is at $\sim$218 GHz, the 220 GHz channel could be used to map CMB fluctuations and subtract them from the SZE data. Depending on how accurately this could be done, such observations could greatly minimize uncertainty due to the CMB. MITO (De Petris et al., 2002) has similar specifications and can target northern clusters.

Chapter 6

Conclusions

In this thesis, we have considered the advantages of using nearby clusters to measure H_0. We have defined a complete, orientation unbiased sample to minimize systematic error from cluster asphericity. Of the 15 clusters in the CBI primary sample, we have complete point source and X-ray data available for seven clusters: A85, A399, A401, A478, A754, A1651, and A2597. From the CBI SZE observations of those seven clusters, we have obtained a measurement of $H_0 = 67^{+30}_{-18\,(\mathrm{ran})}{}^{+15}_{-6\ (\mathrm{sys})}$ km s^{-1} Mpc^{-1} for an unweighted sample average and $H_0 = 75^{+23}_{-16\,(\mathrm{ran})}{}^{+16}_{-7\ (\mathrm{sys})}$ km s^{-1} Mpc^{-1} from a weighted average. We have quantified many sources of error, the largest being contamination due to CMB primary anisotropies. Observations of eight more clusters have been taken, and their analysis will be published in future papers. In addition to the four clusters which we have studied in common, Mason et al. (2001) also determined H_0 from three additional clusters, Coma, A2142, and A2256, which fall under our sample selection criteria but are too far north to be observed with the CBI. If we include those three clusters in our sample average, we obtain a result of $H_0 = 68^{+21}_{-14}$ km s^{-1} Mpc^{-1} for an unweighted average, and $H_0 = 74^{+16}_{-12}$ km s^{-1} Mpc^{-1} for a weighted average. We have not attempted to combine systematic uncertainties for the two different methods. The value of H_0 we obtain from the low redshift clusters is entirely consistent with the value obtained by the *Hubble Space Telescope* Key project of $H_0 = 72 \pm 8$ km s^{-1} Mpc^{-1} (Freedman et al., 2001). Our result is also consistent with that obtained from the SZE at higher redshift by Reese et al. (2002) of $H_0 = 60^{+4}_{-4\,(\mathrm{ran})}{}^{+13}_{-18\,(\mathrm{sys})}$ km s^{-1} Mpc^{-1}, although our sample value is somewhat higher.

With the low redshift clusters, we have also had to contend with larger uncertainties due to

CMB than occur in studies of higher redshift clusters. To minimize this source of error, we have developed an eigenmode weighting method which downweights the modes which have the largest CMB contamination. When this method is used, the uncertainty in $h^{-1/2}$ for the sample is reduced by about 30%, with improvement in individual clusters ranging from ∼10%–35%, depending on the angular size of the cluster. Including the remaining clusters from the sample in this analysis should yield a final sample uncertainty in H_0 of about 15%.

In future work, we will also attempt to address the errors due to incorrect modelling of the cluster gas distribution. *XMM-Newton* and *Chandra* will provide definitive measurements of temperature profiles for the clusters in our sample, and hydrodynamical simulations will allow us to quantify errors from clumpy, aspherical gas distributions. By making these improvements to our results, H_0 measurements from the SZE will provide a powerful check on other methods, such as the cosmic distance ladder of the HST H_0 Key Project.

Appendix A

SZBETA

Since no software existed to analyze the SZE data, it became my task to write such a beast. Armed with a book called Practical C Programming (Oualline, 1997) and the indispensible tutelage of Martin Shepherd, I put together a program called SZBETA, which I have used in all the SZE related work in this thesis. Unfortunately, the code is not very well documented, as it was never intended for use by anyone other than myself. I attempt to remedy this in this Appendix, and explain the main functions and uses of the program. A lot of the code is hardwired specifically for the CBI specifications (10 channels, the primary beam, etc)[1], but these things are not difficult to change.

SZBETA was written using the DIFMAP (Shepherd, 1997) interface, so many very useful features were Martin's creations, like the scripting, and the ability to directly call up PGPLOT functions to plot data. I wrote SZBETA to perform a few major tasks:

1. Plot image and visibility profiles of β-models with varying parameters

2. Simulate CBI observations of the SZE in clusters to compare with observations, and to study different sources of noise through Monte-Carlo simulations

3. Read in actual CBI data, fit SZE profiles to the data to determine H_0.

The program has expanded to about 22,000 lines of code, independent of the DIFMAP interface. Some bits for dealing with covariance matrices were contributed by Jonathan Sievers.

[1] Yes, I wish now I had listened to Martin when he warned me that this was not a good idea.

A.1 Summary of (currently useful) Commands

Several SZBETA commands are now outdated or have been superseded by better renamed versions. Here I list only the functions that are still useful as of this writing.

- **readclust:** reads in cluster β-model parameters from an input file, which should include in columns the cluster name, z, T_e in keV, θ_0 in arcmin, β, n_{e0} in $h^{1/2}\mathrm{cm}^{-3}$, a normalization factor $K/10^{-2}$ from XSPEC as described in Section 4.1, a flag to tell SZBETA whether the central component of the cluster was included (1) in the X-ray analysis or excluded (0) because of a cooling flow, and the frequency of the observation.

- **dt0:** for a given set of cluster parameters, calculates the central SZE decrement in mJy/arcmin^2 and the equivalent temperature in μK and Compton y-parameter. Can include relativistic corrections or kinematic SZE due to peculiar velocity.

- **improf:** plots an SZE image profile for a set of cluster parameters

- **visprof:** plots an SZE visibility profile

- **szim2d:** plots a 2-D map of a simulated cluster image

- **uvplt:** reads in a set of CBI antenna positions, and plots the UV coverage. Can optionally rotate deck by n_dk positions with a step size of rot_size.

- **szvis2d:** shows a 2-D plot of the simulated CBI visibilities

- **dirtyim:** for a given set of (u, v) positions, produces a simulated dirty CBI cluster image.

- **sim2dallchan:** this function has too many parameters; it grew a little too out of hand as I kept adding to it. For a set of (u, v) positions, frequency and integration time, this function creates a fake 2-D data set for a given randomizing seed. Can do all channels and write an output UV fits file. Option to add intrinsic anisotropy array read in by **rdcmb**.

- **chclpar:** function to temporarily change the β-model parameters, for example, when testing ensembles of density model parameters.

- **rdcmb:** reads in a CMB FITS image output by CBISKY to add to simulated clusters
- **gencovar:** creates a covariance matrix for an input CMB spectrum (CMBFAST format).
- **fitdi0:** single parameter fit for the amplitude of a β-model to the visibility data (simulated or real) to determine $h^{-1/2}$.
- **cmpbl:** reduces data size by averaging together points with redundant (u, v) positions.
- **rdcovar:** reads in a covariance matrix created by **gencovar**
- **rdfits:** reads in visibility data from a UV fits file; can be real or simulated.
- **genvis:** fast routine to create a cluster visibility data matrix for input cluster parameters, h, and frequency. Can include relativistic corrections or kinematic SZE due to peculiar velocity.
- **visflux:** reports flux in mJy for a cluster on specified baselines
- **freevis:** frees up memory used by genvis
- **beta_fwhm:** calculate FWHM for a given β-model:
- **setgrid:** need to specify grid size (npixels $\times$ pixel size in arcmin) before calling any function that performs an FFT. npixels must be a power of 2 - SZBETA does not check for this, so get it right.
- **cut_uv:** function to cut out baselines within specified uv range
- **calc_beta_dep:** function to calculate value of

$$\frac{\Gamma(1.5\beta - 0.5)}{\Gamma(1.5\beta)}, \tag{A.1}$$

  which is dependence on β of constant in central decrement
- **ptsrc_uvpl:** function to plot up what a point source looks like in UV space given flux in mJy, x,y coords in arcmin. Effect is basically sinusoidal wave with amplitude = flux of source,

and uv direction is perpendicular to direction in xy space. period is inversely proportional to distance away from pointing center.

- **visprof_avg:** radially averages SZE or CMB visibilities and writes out values to log file as function of radius
- **visprof_ptso:** radially averages contribution from point sources and writes output to file as function of radius
- **radcmp:** radially compresses data read in by **rdfits** (or compressed already via **cmpbl**)
- **set_chanmap:** set channel mapping for compression. default is to convert (1,2,3,4,5,6,7,8,9,10) to (1,1,2,2,3,3,4,4,5,5), averaging adjacent channels.
- **fitptso:** Does the same as **fitdi0**, but allows user to input positions of point sources whose fluxes should be fitted with the cluster. Uses a Levenberg-Marquardt algorithm (Press et al., 1996).
- **calc_da:** calculates angular diameter distance for various cosmologies
- **sim2dtmplt:** does the same as **sim2dallchan**, but instead of using a model (u, v) position set, reads in an actual CBI image, strips the observed data and replaces it with simulated visibility data which has been corrupted with the observed noise.
- **addptso:** adds point sources to bldat array, the main array which stores the visibility data.
- **fluxspix:** calculates expected flux given input frequency (default 1.4 GHz) flux and spectral index
- **newvisprof:** newer version of **visprof** which calculates visibility profile via fft. includes hybrid isothermal/adiabatic models.
- **calc_gamma:** Calculates the gamma function given input value
- **calc_r200:** Calculates r_200 given input values of T_e in keV and z as in Evrard et al. (1996)

- **calc_tproj:** Calculates the observed projected temperature at a given theta for a hybrid profile using

$$T_{\rm proj} = \frac{\int_0^\infty T(r) n^2(r)\, dl}{\int_0^\infty n^2(r)\, dl} \tag{A.2}$$

- **calc_new_t_0:** Accounts for fact that if a cluster has a hybrid temperature profile, its central temperature will be higher than that of an isothermal cluster with the same observed temperature. Calculates the emission weighted temperature out to a specified θ (should match ASCA observations or whatever) for a hybrid profile. annular emission measure Once emission weighted temperature is calculated, scales this to observed temperature and assigns real T_0 to new_t_0.

- **spix_distr:** takes an input file, with fluxes at nu_in GHz (default 1.4 GHz), and for each one, pulls a random spectral from the PMN-OVRO distribution derived in Mason et al. (2003) and calculates flux at specified frequency for that α, writes out new point source file with randomized fluxes at new frequency, default nu_cent=31 GHz.

- **cooray_spix_distr:** same as in **spix_distr**, but uses spectral index distribution of Cooray et al. (1998)

- **get_seed:** gets starting seed for functions that require random number generators.

- **calc_pb:** calculates the CBI primary beam attenuation for a given frequency and position

- **choose_pt:** reads in input point source file, selects out sources that after pb attenuation and random noise are added, would be detectable over a certain noise threshold for the CBI, writes out the file.

- **anti_choose_pt:** writes out file of sources that would NOT be detected by **choose_pt**

- **pt_noise:** simulates effect of subtracting out sources using 40-m observations. ignores listed flux in point source file, but adds random gaussian noise according to rms specified to **pt_noise** and writes out new file.

- **calc_new_ne0:** for files of xray parameters, calculates new ne0's for each beta and theta in file, assuming new $K/10^{-2}$ calculated in xspec and input into sample_final.dat file using new Te and z info.

- **modelrat:** routine to calculate density model bias factor

- **chisq_prob:** routine to calculate probability of exceeding a value of chisq by chance for a given number of degrees of freedom.

- **fitptso2clust:** like **fitptso** but written specifically for the case of A399/A401 and includes the effects of both clusters

Bibliography

Abell, G. O. 1958, ApJS, 3, 211

Abell, G. O., Corwin, H. G., & Olowin, R. P. 1989, ApJS, 70, 1

Arnaud, K. A. 1996, in ASP Conf. Ser. 101: Astronomical Data Analysis Software and Systems V, 17–+

Arnaud, M., Aghanim, N., Gastaud, R., Neumann, D. M., Lumb, D., Briel, U., Altieri, B., Ghizzardi, S., Mittaz, J., Sasseen, T. P., & Vestrand, W. T. 2001a, A&A, 365, L67

Arnaud, M., Neumann, D. M., Aghanim, N., Gastaud, R., Majerowicz, S., & Hughes, J. P. 2001b, A&A, 365, L80

Böhringer, H., Schuecker, P., Guzzo, L., Collins, C. A., Voges, W., Schindler, S., Neumann, D. M., Cruddace, R. G., De Grandi, S., Chincarini, G., Edge, A. C., MacGillivray, H. T., & Shaver, P. 2001, A&A, 369, 826

Böhringer, H., Voges, W., Huchra, J. P., McLean, B., Giacconi, R., Rosati, P., Burg, R., Mader, J., Schuecker, P., Simiç, D., Komossa, S., Reiprich, T. H., Retzlaff, J., & Trümper, J. 2000, ApJS, 129, 435

Baars, J. W. M., Genzel, R., Pauliny-Toth, I. I. K., & Witzel, A. 1977, A&A, 61, 99

Bacchi, M., Feretti, L., Giovannini, G., & Govoni, F. 2003, astro-ph/0301206

Bagchi, J., Pislar, V., & Lima Neto, G. B. 1998, MNRAS, 296, L23+

Birkinshaw, M. 1999, Phys. Rep., 310, 97

Birkinshaw, M., Gull, S. F., & Hardebeck, H. 1984, Nature, 309, 34

Boehringer, H. et al. 2003, A&A, in preparation

Carter, D. & Metcalfe, N. 1980, MNRAS, 191, 325

Cavaliere, A. & Fusco-Femiano, R. 1978, A&A, 70, 677

Challinor, A. & Lasenby, A. 1998, ApJ, 499, 1

Colafrancesco, S., Marchegiani, P., & Palladino, E. 2003, A&A, 397, 27

Colberg, J. M., White, S. D. M., MacFarland, T. J., Jenkins, A., Pearce, F. R., Frenk, C. S., Thomas, P. A., & Couchman, H. M. P. 2000, MNRAS, 313, 229

Condon, J. J., Cotton, W. D., Greisen, E. W., Yin, Q. F., Perley, R. A., Taylor, G. B., & Broderick, J. J. 1998, AJ, 115, 1693

Cooray, A. R. 2000, MNRAS, 313, 783

Cooray, A. R., Grego, L., Holzapfel, W. L., Joy, M., & Carlstrom, J. E. 1998, AJ, 115, 1388

De Grandi, S. & Molendi, S. 2002, ApJ, 567, 163

De Petris, M., D'Alba, L., Lamagna, L., Melchiorri, F., Orlando, A., Palladino, E., Rephaeli, Y., Colafrancesco, S., Kreysa, E., & Signore, M. 2002, ApJ, 574, L119

Doré, O., Bouchet, F. R., Mellier, Y., & Teyssier, R. 2001, A&A, 375, 14

Ebeling, H., Edge, A. C., Bohringer, H., Allen, S. W., Crawford, C. S., Fabian, A. C., Voges, W., & Huchra, J. P. 1998, MNRAS, 301, 881

Ebeling, H., Voges, W., Bohringer, H., Edge, A. C., Huchra, J. P., & Briel, U. G. 1996, MNRAS, 281, 799

Edge, A. C., Stewart, G. C., Fabian, A. C., & Arnaud, K. A. 1990, MNRAS, 245, 559

Evrard, A. E., Metzler, C. A., & Navarro, J. F. 1996, ApJ, 469, 494

Fabian, A. C., Peres, C. B., & White, D. A. 1997, MNRAS, 285, L35

Fixsen, D. J. & Mather, J. C. 2002, ApJ, 581, 817

Freedman, W. L., Madore, B. F., Gibson, B. K., Ferrarese, L., Kelson, D. D., Sakai, S., Mould, J. R., Kennicutt, R. C., Ford, H. C., Graham, J. A., Huchra, J. P., Hughes, S. M. G., Illingworth, G. D., Macri, L. M., & Stetson, P. B. 2001, ApJ, 553, 47

Fujita, Y., Koyama, K., Tsuru, T., & Matsumoto, H. 1996, PASJ, 48, 191

Giovanelli, R., Haynes, M. P., Salzer, J. J., Wegner, G., da Costa, L. N., & Freudling, W. 1998, AJ, 116, 2632

Gonzalez, A. H., Zabludoff, A. I., Zaritsky, D., & Dalcanton, J. J. 2000, ApJ, 536, 561

Grainge, K., Jones, M. E., Pooley, G., Saunders, R., Edge, A., Grainger, W. F., & Kneissl, R. 2002, MNRAS, 333, 318

Grego, L., Carlstrom, J. E., Reese, E. D., Holder, G. P., Holzapfel, W. L., Joy, M. K., Mohr, J. J., & Patel, S. 2001, ApJ, 552, 2

Gursky, H., Solinger, A., Kellogg, E. M., Murray, S., Tananbaum, H., Giacconi, R., & Cavaliere, A. 1972, ApJ, 173, L99+

Halverson, N. W., Leitch, E. M., Pryke, C., Kovac, J., Carlstrom, J. E., Holzapfel, W. L., Dragovan, M., Cartwright, J. K., Mason, B. S., Padin, S., Pearson, T. J., Readhead, A. C. S., & Shepherd, M. C. 2002, ApJ, 568, 38

Henriksen, M. J. & Markevitch, M. L. 1996, ApJ, 466, L79+

Henry, J. P. & Briel, U. G. 1995, ApJ, 443, L9

Herbig, T., Lawrence, C. R., Readhead, A. C. S., & Gulkis, S. 1995, ApJ, 449, L5+

Holzapfel, W. L., Arnaud, M., Ade, P. A. R., Church, S. E., Fischer, M. L., Mauskopf, P. D., Rephaeli, Y., Wilbanks, T. M., & Lange, A. E. 1997, ApJ, 480, 449

Hughes, J. P., Yamashita, K., Okumura, Y., Tsunemi, H., & Matsuoka, M. 1988, ApJ, 327, 615

Itoh, N., Kohyama, Y., & Nozawa, S. 1998, ApJ, 502, 7

Kassim, N. E., Clarke, T. E., Enßlin, T. A., Cohen, A. S., & Neumann, D. M. 2001, ApJ, 559, 785

Kauffmann, G., Colberg, J. M., Diaferio, A., & White, S. D. M. 1999, MNRAS, 303, 188

Kempner, J. C., Sarazin, C. L., & Ricker, P. M. 2002, ApJ, 579, 236

Leitch, E. M. 1998, PhD thesis, California Institute of Technology

Lima Neto, G. B., Pislar, V., & Bagchi, J. 2001, A&A, 368, 440

MacGillivray, H. T. & Stobie, R. S. 1984, Vistas in Astronomy, 27, 433

Markevitch, M., Forman, W. R., Sarazin, C. L., & Vikhlinin, A. 1998, ApJ, 503, 77

Mason, B. S., Leitch, E. M., Myers, S. T., Cartwright, J. K., & Readhead, A. C. S. 1999, AJ, 118, 2908

Mason, B. S. & Myers, S. T. 2000, ApJ, 540, 614

Mason, B. S., Myers, S. T., & Readhead, A. C. S. 2001, ApJ, 555, L11

Mason, B. S., Pearson, T. J., Readhead, A. C. S., Shepherd, M. C., Sievers, J., Udomprasert, P. S., Cartwright, J. K., Farmer, A. J., Padin, S., Myers, S. T., Bond, J. R., Contaldi, C. R., Pen, U., Prunet, S., Pogosyan, D., Carlstrom, J. E., Kovac, J., Leitch, E. M., Pryke, C., Halverson, N. W., Holzapfel, W. L., Altamirano, P., Bronfman, L., Casassus, S., May, J., & Joy, M. 2003, ApJ, 591, 540

McMillan, S. L. W., Kowalski, M. P., & Ulmer, M. P. 1989, ApJS, 70, 723

Mohr, J. J., Evrard, A. E., Fabricant, D. G., & Geller, M. J. 1995, ApJ, 447, 8

Myers, S. T., Baker, J. E., Readhead, A. C. S., Leitch, E. M., & Herbig, T. 1997, ApJ, 485, 1

Navarro, J. F., Frenk, C. S., & White, S. D. M. 1995, MNRAS, 275, 720

Oualline, S. 1997, Practical C Programming (O'Reilly & Associates)

Padin, S., Cartwright, J. K., Mason, B. S., Pearson, T. J., Readhead, A. C. S., Shepherd, M. C., Sievers, J., Udomprasert, P. S., Holzapfel, W. L., Myers, S. T., Carlstrom, J. E., Leitch, E. M., Joy, M., Bronfman, L., & May, J. 2001, ApJ, 549, L1

Padin, S., Shepherd, M. C., Cartwright, J. K., Keeney, R. G., Mason, B. S., Pearson, T. J., Readhead, A. C. S., Schaal, W. A., Sievers, J., Udomprasert, P. S., Yamasaki, J. K., Holzapfel, W. L., Carlstrom, J. E., Joy, M., Myers, S. T., & Otarola, A. 2002, PASP, 114, 83

Pariiskii, Y. N. 1972, AZh, 49, 1322

Pearson, T. J., Mason, B. S., Readhead, A. C. S., Shepherd, M. C., Sievers, J. L., Udomprasert, P. S., Cartwright, J. K., Farmer, A. J., Padin, S., Myers, S. T., Bond, J. R., Contaldi, C. R., Pen, U.-L., Prunet, S., Pogosyan, D., Carlstrom, J. E., Kovac, J., Leitch, E. M., Pryke, C., Halverson, N. W., Holzapfel, W. L., Altamirano, P., Bronfman, L., Casassus, S., May, J., & Joy, M. 2003, ApJ, 591, 556

Perley, R. A. & Taylor, G. B. 2003, the VLA Calibrator Manual

Press, W. H., Teukolsky, S. A., Vetterling, W. T., & Flannery, B. P. 1996, Numerical Recipes: The Art of Scientific Computing (Cambridge University Press)

Prestwich, A. H., Guimond, S. J., Luginbuhl, C. B., & Joy, M. 1995, ApJ, 438, L71

Raymond, J. C. & Smith, B. W. 1977, ApJS, 35, 419

Reese, E. D., Carlstrom, J. E., Joy, M., Mohr, J. J., Grego, L., & Holzapfel, W. L. 2002, ApJ, 581, 53

Rephaeli, Y. 1995, ApJ, 445, 33

Runyan, M. C., Bhatia, R. S., Lange, A. E., Daub, M. D., Holzapfel, W. L., Kuo, C. L., Leuker, M., Newcomb, M., Woolsey, D., Goldstein, J., Leong, J., Ruhl, J., Torbet, E., Cantalupo, C.,

Gomez, P., Peterson, J. B., Romer, A. K., Ade, P. A. R., Haynes, C. V., Tucker, C., Bock, J. J., & Sethuraman, S. 2002, American Astronomical Society Meeting, 201, 0

Sarazin, C. L. & McNamara, B. R. 1997, ApJ, 480, 203

Sazonov, S. Y. & Sunyaev, R. A. 1998, ApJ, 508, 1

Shepherd, M. C. 1997, in ASP Conf. Ser. 125: Astronomical Data Analysis Software and Systems VI, 77–+

Shimon, M. & Rephaeli, Y. 2002, ApJ, 575, 12

Sievers, J. L., Bond, J. R., Cartwright, J. K., Contaldi, C. R., Mason, B. S., Myers, S. T., Padin, S., Pearson, T. J., Pen, U.-L., Pogosyan, D., Prunet, S., Readhead, A. C. S., Shepherd, M. C., Udomprasert, P. S., Bronfman, L., Holzapfel, W. L., & May, J. 2003, ApJ, 591, 599

Slingo, A. 1974, MNRAS, 168, 307

Struble, M. F. & Rood, H. J. 1999, ApJS, 125, 35

Sunyaev, R. A. & Zel'dovich, Y. B. 1970, Comments on Astrophysics, 2, 66

—. 1972, Comments on Astrophysics and Space Physics, 4, 173

Taylor, A. C., Grainge, K., Jones, M. E., Pooley, G. G., Saunders, R. D. E., & Waldram, E. M. 2001, MNRAS, 327, L1

Thompson, A. R., Moran, J. M., & Swenson, G. W. 1998, Interferometry and Synthesis in Radio Astronomy (Krieger Publishing Company)

Tsuboi, M., Miyazaki, A., Kasuga, T., Matsuo, H., & Kuno, N. 1998, PASJ, 50, 169

White, D. A. 2000, MNRAS, 312, 663

White, D. A., Fabian, A. C., Allen, S. W., Edge, A. C., Crawford, C. S., Johnstone, R. M., Stewart, G. C., & Voges, W. 1994, MNRAS, 269, 589

White, M., Carlstrom, J. E., Dragovan, M., & Holzapfel, W. L. 1999, ApJ, 514, 12

Zaroubi, S., Squires, G., Hoffman, Y., & Silk, J. 1998, ApJ, 500, L87+

Zel'dovich, Y. B. & Sunyaev, R. A. 1969, Ap&SS, 4, 301